論文 / 著書情報
Article / Book Information

題目(和文)	
Title(English)	Study of diamond heteroepitaxy on Si substrates for power and sensor devices
著者(和文)	矢板潤也
Author(English)	Junya Yaita
出典(和文)	学位:博士(工学), 学位授与機関:東京工業大学, 報告番号:甲第10801号, 授与年月日:2018年3月26日, 学位の種別:課程博士, 審査員:波多野 睦子,宮本 恭幸,河野 行雄,小寺 哲夫,鈴木 左文,小泉 聡
Citation(English)	Degree:Doctor (Engineering), Conferring organization: Tokyo Institute of Technology, Report number:甲第10801号, Conferred date:2018/3/26, Degree Type:Course doctor, Examiner:,,,,,
学位種別(和文)	博士論文
Type(English)	Doctoral Thesis

Study of diamond heteroepitaxy on Si substrates for power and sensor devices

Junya Yaita
Department of Physical Electronics
Tokyo Institute of Technology

March, 2018

Abstract

Heteroepitaxial growth of diamond on a Si substrate is an important technology for synthesizing large-area and low-cost diamond films for both next-generation power devices and high-sensitivity sensor devices. However, Si substrates show a large lattice mismatch and surface energy difference from those of diamond films. Therefore, it is difficult to induce direct epitaxial nucleation of diamond on Si. Cubic silicon carbide (3C-SiC) is a candidate material to form an intermediate layer between Si and diamond for diamond heteroepitaxy, because the 3C-SiC film can be grown on the Si substrate and the lattice constant and surface energy of SiC are close to those of diamond. This study describes the heteroepitaxial growth of diamond on both Si (001) and (111) substrates via a 3C-SiC intermediate layer. The performance of the heteroepitaxially grown diamond film and the applicability of this process to both power and sensor devices are investigated. Epitaxial diamond nucleation was conducted on 3C-SiC (001)/Si (001) substrates using the original antenna-edge type microwave-plasma chemical vapor deposition (CVD) technique. It was observed that in situ bias current monitoring during diamond nucleation of bias-enhanced nucleation (BEN) is effective in controlling epitaxial nucleation. Using this technique, a tilt spread of 0.52° with a perfectly coalesced diamond (001) film could be obtained. To the best of our knowledge, this is the highest value for a diamond (001) film grown on a 3C-SiC substrate. Moreover, epitaxial diamond (111) grains were developed on the 3C-SiC/Si (111) substrate by utilizing the same nucleation technique. The synthesis of (111) highly oriented diamond thin films was confirmed for the first time. It was observed that this nucleation technology can become a popular method to produce epitaxial diamond nuclei, irrespective of the crystal face and the underlying material. The power and sensor devices were demonstrated by using heteroepitaxial diamond (001) and (111) films, respectively. Schottky barrier diodes (SBDs) were fabricated on heteroepitaxial diamond (001) films. The specific on-resistance of 0.2 Ωcm^2 and a high rectification of 10^8 (±5 V)

were obtained, which are comparable to those of the SBDs on homoepitaxial diamond films. It is necessary to further improve the heteroepitaxial growth and device technology in order to suppress the leakage current. Sensor devices using nitrogen-vacancy (NV) centers in diamond were formed in the heteroepitaxial diamond (111) films. The NV centers in heteroepitaxial diamond can be preferentially aligned to one atomic direction and an improvement in sensitivity was confirmed. This development of the heteroepitaxial diamond films is expected to be useful for fabricating large-area and low-cost power and sensor device platforms.

Contents

Abstract ii
Contents iii
Previously published papers v
Acknowledgments vi

1 Introduction **1**
1.1 Research background 1
1.1.1 Diamond power devices 1
1.1.2 NV center in diamond for sensor devices 2
1.1.3 Issues in practical use of diamond devices 3
1.2 Single-crystal diamond substrates and homoepitaxial growth of diamond . 6
1.2.1 High-pressure high-temperature method 6
1.2.2 Chemical vapor deposition 6
1.3 Diamond heteroepitaxy on close lattice constant materials 9
1.3.1 Diamond on c-BN 9
1.3.2 Diamond on Ni 9
1.4 Si substrates based diamond heteroepitaxy 11
1.4.1 Bias enhanced nucleation 13
1.4.2 Heteroepitaxial diamond film on Si substrates 13
1.4.3 Heteroepitaxial diamond film on Pt intermediate layer 15
1.4.4 Heteroepitaxial diamond film on Ir intermediate layer 15
1.4.5 Heteroepitaxial diamond film on 3C-SiC intermediate layer 16
1.5 Objective of this research and structure of the study 17

2 EPITAXIAL NUCLEATION **19**
2.1 Background of epitaxial nucleation of diamond on 3C-SiC 19
2.2 Influence of high microwave plasma density 22
2.2.1 Antenna-edge type microwave plasma CVD 22
2.2.2 Characterization of the plasma conditions 24
2.2.3 Effect of high plasma condition 27
2.3 In-situ monitoring of the epitaxial nucleation by the bias current 31
2.3.1 The bias current duration during BEN 31

2.3.2 Nucleation process analysis by Avrami exponent 35
2.4 Large-area nucleation 39
2.5 Conclusion 40

3 HETEROEPITAXIAL GROWTH 41
3.1 Heteroepitaxial growth of diamond(001) 41
3.1.1 Two-step growth process 42
3.1.2 Residual stress and dislocations in diamond film 44
3.2 Heteroepitaxial growth of diamond(111) 49
3.2.1 Effect of oxygen gas addition for growth of diamond(111) 51
3.2.2 Highly-oriented diamond(111) film on 3C-SiC(111)/Si(111) . . . 51
3.3 Conclusion 54

4 POWER AND SENSOR DEVICES 55
4.1 SBDs on heteroepitaxial diamond(001) 55
4.1.1 Fabrication process of SBDs 55
4.1.2 Electrical characteristics of SBDs on heteroepitaxial diamond on 3C-SiC 56
4.2 NV centers in heteroepitaxial diamond(111) 63
4.2.1 Fabrication process of NV centers in heteroepitaxial diamond . . 63
4.2.2 NV centers in diamond particles 64
4.2.3 NV centers in heteroepitaxial diamond films 67
4.2.4 Magnetic sensitivity of NV center in heteroepitaxial diamond film 71
4.3 Conclusion 76

5 SUMMARY 77
5.1 Thesis summary 77

A APPENDIX 79
A.1 Growth of single crystal 3C-SiC on Si 79
A.2 Diamond nucleation and growth conditions 81
Bibliography 84

Citations of previously paper

1. J. Yaita, T. Iwasaki, M. Natal, S. E. Saddow, and M. Hatano, Heteroepitaxial growth of diamond on 3C-SiC/Si substrates with utilization of antenna-edge microwave plasma CVD, Jpn. J. Appl. Phys., **54**, 04DH13 (2015).

2. J. Yaita, M. Natal, S. E. Saddow, M. Hatano, and T. Iwasaki, Influence of high-power density plasma on heteroepitaxial diamond nucleation on 3C-SiC surface, Appl. Phys. Express, **10**, 045502 (2017).

3. T. Suto, J. Yaita, T. Iwasaki, and M. Hatano, Highly oriented diamond (111) films synthesized by pulse bias-enhanced nucleation and epitaxial grain selection on a 3C-SiC/Si (111) substrate, Appl. Phys. Lett., **110**, 062102 (2017).

4. J. Yaita, T. Tsuji, M. Hatano, and T. Iwasaki, Preferentially aligned nitrogen-vacancy centers in heteroepitaxial (111) diamonds on Si substrates via 3C-SiC intermediate layers, Appl. Phys. Express, (in press).

Acknowledgements

I would like to thank my supervisors Prof. Hatano and Prof. Kodera for their considerable support in my PhD research work. My thesis committee, comprising Prof. Miyamoto, Prof. Suzuki, Prof. Kawano, and Dr. Koizumi (National Institute for Materials Science), helped me with constant feedback and encouragement. I would also like to thank Dr. Iwasaki for encouraging my research, developing my career, and providing me with immense knowledge. Dr. Ishiwata and Dr. Masuyama also helped me in my research work. The 3C-SiC intermediate layers on Si substrates for the diamond heteroepitaxy process were provided by Prof. Stephen and Dr. Natal (University of South Florida). They also provided me with some sound advice about my published papers. The diamond-doped layers and devices were fabricated by Dr. Yamasaki, Dr. Makino, Dr. Ogura, and Dr. Kato (Advanced Industrial Science and Technology). Ms. Kobayashi and Ms. Saito, who are secretaries in Hatano-Kodera Laboratory, Tokyo Institute of Technology, helped me deal with paperwork. I am also grateful to the members of Hatano-Kodera Laboratory, especially Takeru Suto, Takuya Murooka, and Takeyuki Tsuji. The heteroepitaxial growth of diamond (111) was performed by Takeru Suto, the electric characteristics of the diamond film were measured by Takuya Murooka, and Takeyuki Tsuji helped me with NV center measurements.

Chapter 1

Introduction

1.1 Research background

1.1.1 Diamond power devices

To realize sustainable development, power devices with low loss and high breakdown voltage are required. Si devices have already reached their theoretical limit; thus, it is necessary to replace them with new materials to dramatically improve the device characteristics. Wide-band-gap semiconductors, such as silicon carbide (SiC), gallium nitride (GaN), and diamond, have a higher breakdown electric field than that of Si; thus, it is possible to improve the electric characteristics of power devices using such semiconductors. Table 1.1 shows the electric properties of diamond and other power-device materials. Compared with other semiconductor materials, diamond has superior electric characteristics, such as high carrier mobility and high breakdown electric field (10 MV/cm). The Baliga's figure of merit (BFOM) of diamond that indicates the resistive loss of power devices is much higher than that of Si, SiC, and GaN, which proves that the diamond is useful for low-loss power devices. The diamond power devices have been demonstrated as Schottky barrier diodes (SBDs) [1, 2], junction field-effect transistors (FETs) [3], and metal-oxide-semiconductor FETs (MOSFETs) [4] so far.
In this study, the SBD is described. A high current density of order $\mathrm{kA/mm^2}$ [5] and a high breakdown electric field at 7.7 MV/cm [6] have been reported. In addition to low-loss devices, the cooling systems can be simplified or eliminated because of the high thermal conductivity of diamond of 20 $\mathrm{W/cm \cdot K}$, resulting in the downsizing of the system.

Table 1.1: Properties of semiconductor materials

Material		Si	4H-SiC	GaN	Diamond
Bandgap [eV]		1.1	3.26	3.39	5.47
Mobility [cm^2/Vs]	Electron	1400	1000	900	2200
	Hall	600	115	150	1600
Breakdown electric field [MV/cm]		0.3	2.5	3.3	10
Thermal conductivity [W/cmK]		1.5	4.9	2.0	20
Relative permittivity		11.9	9.7	9.0	5.5
BFOM		1	700	1000	22000

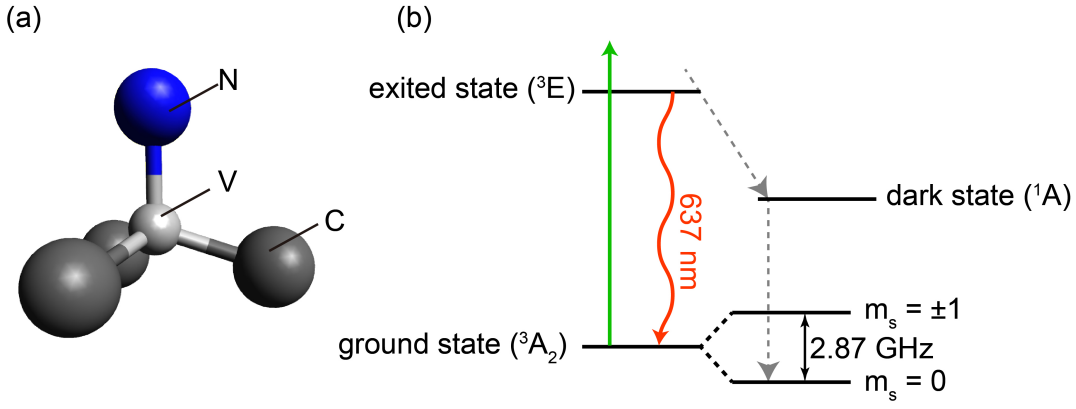

Figure 1.1: (a) Structure of NV center in diamond and (b) energy levels of NV center.

1.1.2 NV center in diamond for sensor devices

Diamond has many point-defect color centers, such as germanium-vacancy [7], tin-vacancy [8], silicon-vacancy (SiV) [9, 10], and nitrogen-vacancy (NV) [11, 12] centers. These color centers are expected to be useful for biology, quantum information processing, electric [13, 14], thermometry [15–17], and as magnetic sensors [12, 18] because they have high photo-stability and optical intensity. In particular, the negatively charged NV centers are extremely useful in the nuclear magnetic resonance [19], magnetic field, and electric field [13] measurements because the NV center has a spin-triplet state, which can be controlled at room temperature, as shown in Fig. 1.1. The spin states of the NV center can be read out by optically detected magnetic resonance (ODMR) because the ground state is controlled by microwave and $m_s = \pm 1$ are the dark states. The ground-state

Hamiltonian equation is described by

$$\mathcal{H} = \frac{1}{\hbar^2}\left\{(D_{gs} + \varepsilon_z)S_z^2 - \varepsilon_x(S_x^2 - S_y^2) + \varepsilon_y(S_xS_y + S_yS_x)\right\} + \frac{g\mu_b}{\hbar}S \cdot B \tag{1.1}$$

where D_{gs} (2.87 GHz) is the zero-field splitting parameter, ε is the energy of interaction between external electric field (E) and strain (σ), B is the magnetic field, d_{gs} is the NV electric dipole moment, $g(2.00)$ is the electron g-factor, and b is the Bohr magneton. Thus, the ODMR spectrum reflects the electric field, strain, and magnetic field of the region around NV centers. For these reasons, the NV centers in diamond are a promising prospect for highly sensitive thermometry, electrometry, and magnetometry. Nano-scale diamond particles are expected for thermometry in living cells, because they have a high sensitivity of 3.5 mK [20] with a very small crystalline size, and diamond consists of only carbon atoms, which indicates the non-toxic material. In addition to magnetometry, it is also expected for electrometry to measure the electric field in diamond and other semiconductor materials. The magnetometry using NV centers in diamond are demonstrated as NMR and MRI. Its sensitivity (η) is scaled with

$$\eta \propto \frac{1}{C\sqrt{NT_2}} \tag{1.2}$$

where C is the contrast of ODMR, N is the density of the NV centers, and T_2 is the coherence time of the electron spin. To obtain a high contrast of ODMR C to improve the sensitivity, NV centers in diamond should be aligned toward one direction. For the formation of aligned NV centers, single-crystal diamond (111) substrates are desirable, instead of diamond (001) substrates because single-crystal diamond (111) substrates enable us to form perfectly aligned NV centers [21, 22].

1.1.3 Issues in practical use of diamond devices

Conventional diamond devices are formed on single-crystal diamond substrates. However, the size of diamond substrates is limited to several mm^2 area due to the synthesizing process of diamond. The current in diamond power devices is limited to less than several A [23] because of the small substrates. Moreover, it is necessary to reduce the fabrication cost for practical application of diamond devices. The heteroepitaxial growth of diamond on Si substrates is a promising approach to fabricate large-area and low-cost single-crystal diamond films. Figure 1.2 shows the various industries expected to have diamond device

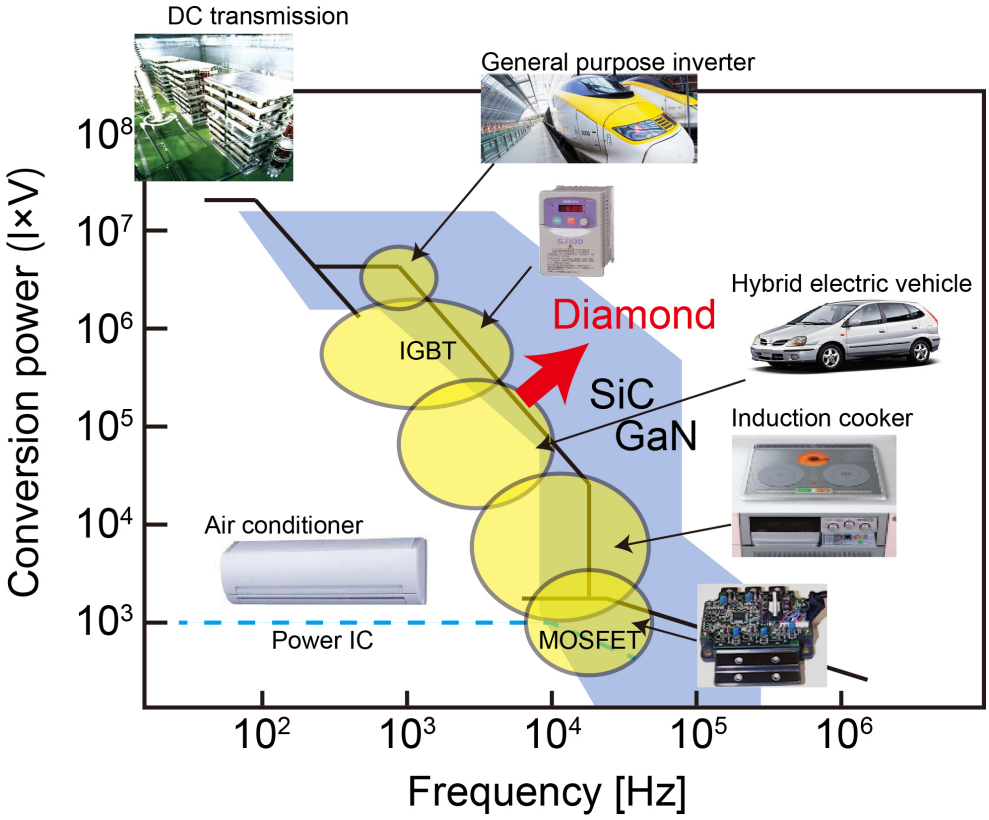

Figure 1.2: Expected field of application of diamond power devices

applications. A large-area heteroepitaxial diamond is a promising approach for increasing the current.

From the view point of sensor devices, the heteroepitaxial growth of diamond films on Si substrates is an alternative approach for fabricating a large-area quantum sensing platform [11]. It can sense the wide fields, such as those in magnetocardiography and magnetoencephalography. Figure 1.3 shows the expected field of application of heteroepitaxial diamond films as sensor devices. Heteroepitaxial diamond films can be expected for macro-scale sensing with size as small as few centimeters. In addition to size and cost, heteroepitaxial diamond films on Si substrates is expected to enable on-chip integration with well-established Si COMS technologies. Another advantage of heteroepitaxial thin films is the fabrication of photonic structures, as demonstrated for NV [24] and SiV [25] centers.

In this study, we focus on the heteroepitaxial growth of diamond on Si substrates for power and sensor devices. The heteroepitaxial growth of diamond has been demonstrated by

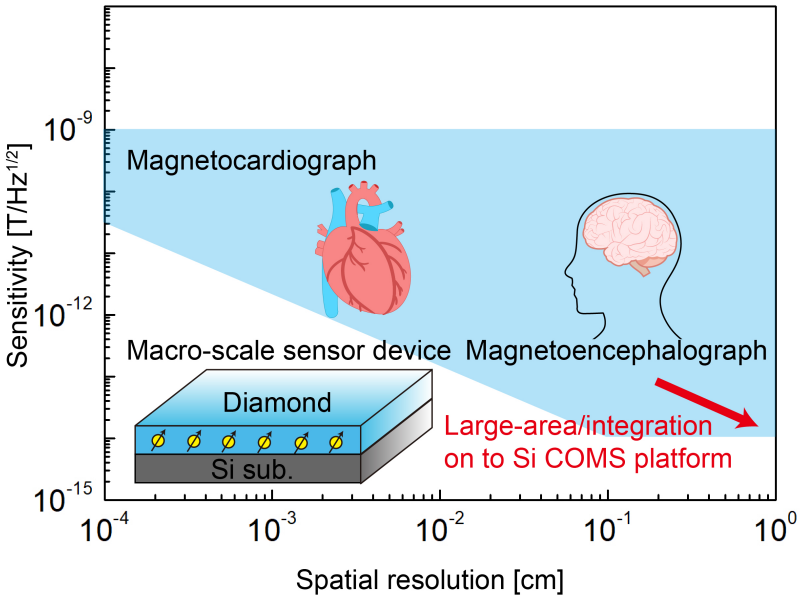

Figure 1.3: Expected field of application of sensor devices with heteroepitaxial diamond on Si substrates.

various substrates and/or buffer layers so far. We consider that the heteroepitaxial growth on 3C-SiC/Si substrates is candidate material for diamond heteroepitaxy from view point of its cost and scalability.

1.2 Single-crystal diamond substrates and homoepitaxial growth of diamond

1.2.1 High-pressure high-temperature method

A conventional method of synthesizing single-crystal diamond substrates is the use high-pressure high-temperature (HPHT) method. A phase diagram of carbon is shown in Fig. 1.4. In this figure, carbon atoms are directly transformed into diamond under a high-pressure and high-temperature environment. The formation energy of graphite is 2.9 kJ/mol, which is smaller than that of diamond. However, a large energy barrier exists between diamond and graphite. Therefore, diamond does not transform into graphite at room temperature. Although at high temperatures, above around 1000 °C, diamond transforms into graphite.

1.2.2 Chemical vapor deposition

Homoepitaxial growth of diamond is achieved by chemical vapor deposition (CVD). Typically, hydrogen and hydrocarbons (e.g., CH_4) are used for growth gases. Hydrocarbon gas is used for providing carbon, which is the precursor of diamond growth, and hydrogen is used as a carrier gas. Diamond growth by CVD is performed with a low methane concentration of 0.025 % [27, 28], because the decomposed hydrogen plays an important role in diamond growth by CVD. For diamond growth, the CVD condition is typically performed at a high pressure of several dozen [kPa], low methane concentration of approximately 10 % in hydrogen gas, and a high temperature of approximately 1200 °C. The introduction of hydrogen into growth gas is important for diamond growth because not only diamond but also graphite is synthesized without hydrogen CVD. The decomposed hydrogen (i.e., atomic hydrogen) selectively etch the graphite during CVD growth [29]. Thus, it is possible to synthesize only diamond.

There are three major growth modes in crystal growth, and methane concentration,

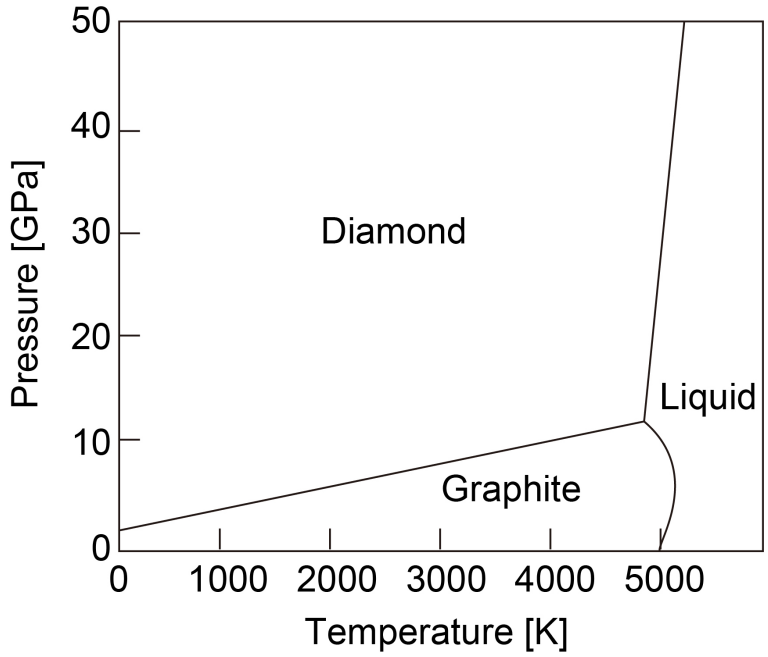

Figure 1.4: Phase and transition diagram of carbon [26].

growth temperature, and off angle determine these growth modes and growth rate. To obtain a high-quality diamond film, it is desirable to grow the Frank van der Merve (FM) mode. The combination of very low methane concentration (0.05 %) and substrate with misorientation-angle enhance the FM growth mode [27], which is called the step-flow growth. This is because the atoms are introduced at step-edges formed by the misorientation angle. For diamond (001) and (111) substrates, the misorientation angle towards the <110> and $[\overline{1}\overline{1}2]$ direction is useful for the step-flow growth, respectively. This is because the dangling bonds of these directions face the growth direction. Using these techniques, high-quality diamond films can grow on HPHT single-crystal diamond substrates. However, the size of diamond films are limited by the HPHT substrates size of several mm^2. To solve this problem, two methods have been reported. First, several clone films, grown on the same HPHT substrate by CVD, are merged with each other by the CVD growth [30] (Fig. 1.5(a)). Thus, the surface of the clones is coalesced and this technique is called "Mozaic wafer". This technique produces a wafer of size $20 \times 40\ mm^2$ as compared to the typical HPHT substrate size of several mm^2. However, the merged interface of "Mozaic wafer" is defective and consists of screw dislocations and stacking faults. The other method is called the three-dimensional enlarging process of crystal size [31]. In

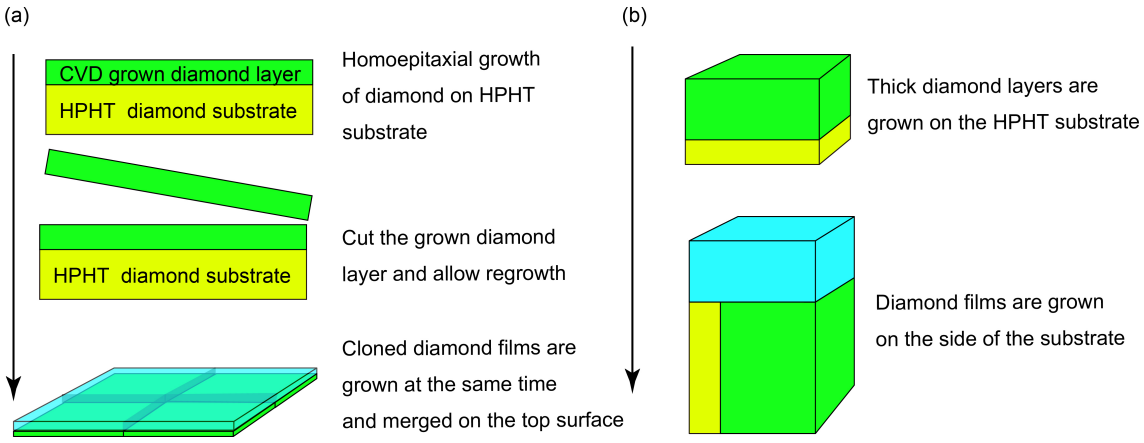

Figure 1.5: Schematic illustration of the procedure of large-area substrates synthesis from HPHT substrates by (a) clones and (b) three-dimensional enlarging process.

this method, the area of the diamond is increased by epitaxially growing the diamond substrate side after growing a thick diamond (Fig. 1.5(b)s). This method takes a long time to complete because of the very slow growth rate of diamond (150 μm/h).

1.3 Diamond heteroepitaxy on close lattice constant materials

The ideal substrates for heteroepitaxy are small lattice mismatch and close surface energy with diamond. For this reason, diamond heteroepitaxy has been performed on cubic boron nitride (c-BN), Ni (Fig. 1.6), and *etc*. In this section, we describe their characteristics.

1.3.1 Diamond on c-BN

A c-BN is an ideal substrate for diamond heteroepitaxy because it has the same crystal structure, very close lattice constant of 3.6 Å with diamond (the difference is only 1.3 %), and close surface free energy with diamond. It is the only substrate that can grow heteroepitaxial diamond films without any pre-treatment (i.e., the synthesis process for heteroepitaxial diamond films on c-BN substrates is almost the same as that used for growing single crystal diamond by CVD). To obtain thin heteroepitaxial diamond films, the nucleation density of at least 10^8 cm^{-2} is required. For diamond heteroepitaxy on c-BN substrates, the nucleation density of diamond reaches 10^{10} cm^{-2} using a boron-terminated surface. Thus, continuous diamond films can be obtained after several minutes of growth. Another advantage of diamond heteroepitaxy on c-BN is that it is easy to fabricate the pn-structure because the n-type c-BN is obtained by Si impurities and the p-type diamond is obtained by boron impurities. This is expected for pn-junction devices, such as light-emitting diodes. However, the size of c-BN is limited, as in the case of diamond.

1.3.2 Diamond on Ni

Heteroepitaxial growth of diamond on metal substrates or intermediate layers are demonstrated by using Ni, Pt, and *etc*. Ni also has a small lattice mismatch of 1.2 % with diamond. Hence, the Ni substrate can be used as a substrate material for diamond heteroepitaxy. The heteroepitaxial growth of diamond on Ni substrates has been demonstrated by MPCVD. Although the epitaxial diamond nanoparticles appeared after CVD process, the sp^2 component such as graphite is also synthesized on Ni substrates because of the catalytic effect of Ni, which has a high carbon solubility. To inhibit the sp^2 component on the Ni substrates, the three-step growth process has been performed as follows [34].

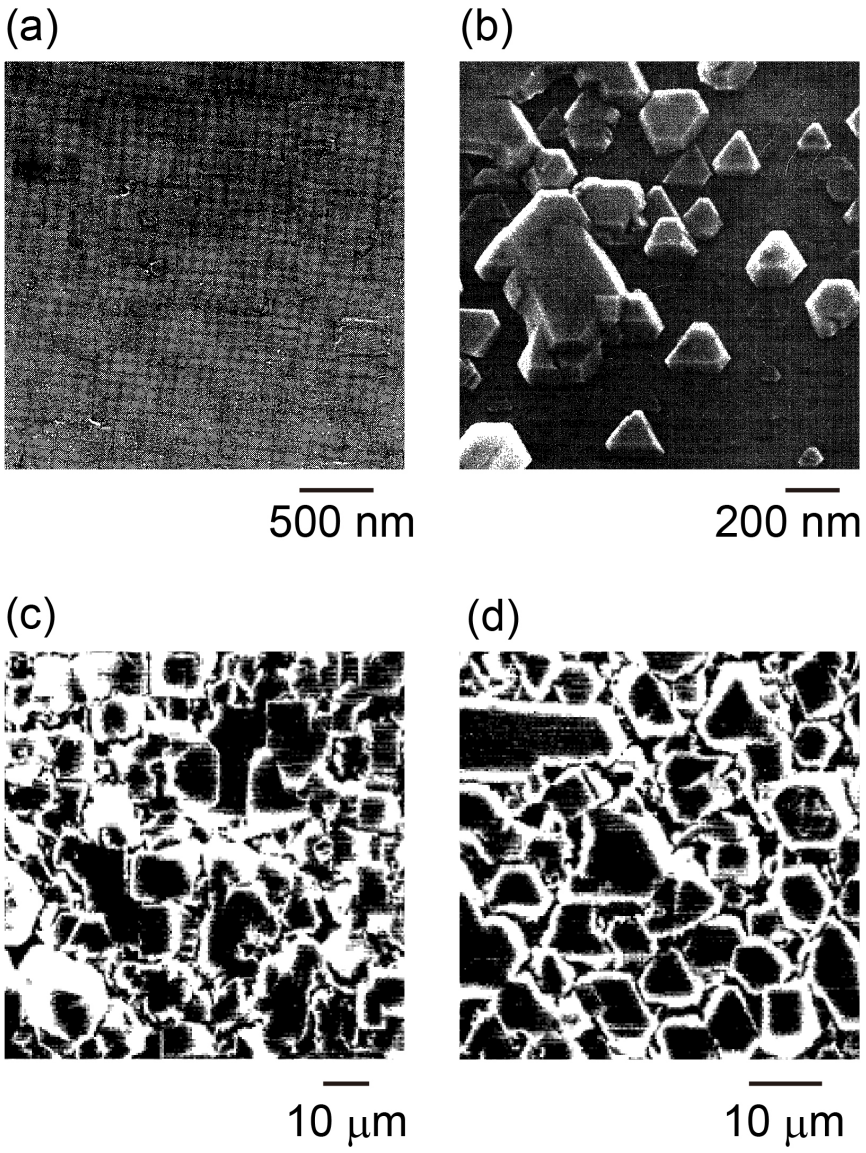

Figure 1.6: SEM images of heteroepitaxial diamond on (a, b) c-BN [32] and (c, d) Ni [33]. (a,c) and (b, d) are the (001) and (111) substrates, respectively.

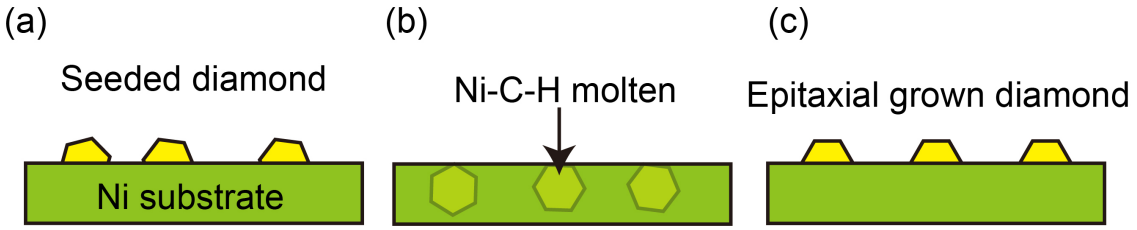

Figure 1.7: Schematic illustrations of (a) seeding, (b) annealing, and (c) growth process of diamond on Ni substrates.

(i) Diamond nanoparticles were scratched on Ni substrates (Fig. 1.7(a)); (ii) the scratched diamond nanoparticles on Ni substrates are annealed at a high temperature of above 1000 °C without methane gas. In this process, the seeded diamond nanoparticles dissolve into the Ni surface, and form the Ni-C-H molten states (Fig. 1.7(b)); and (iii) the CVD condition is set to diamond growth (i.e., introduce the methane and lower temperature of around 900 °C). After this step, the carbon atoms in the Ni-C-H molten forms the epitaxial diamond nuclei and it grows, resulting in the synthesis of epitaxial diamond films (Fig. 1.7(c)). Using this technique, the heteroepitaxial diamond with both (001) and (111) on Ni substrates has been reported.

1.4 Si substrates based diamond heteroepitaxy

Si substrates are promising materials for the heteroepitaxial growth of diamond owing to their scalability, low coefficient of thermal expansion (CTE), and low cost. However, the diamond nanoparticles on Si substrates are not epitaxially nucleated because of the large lattice mismatch of 32 % and large surface energy differences (1.51 and 5.60 J/m^2 for Si and diamond [35], respectively). Therefore, synthesized diamond on Si has large angular spread films. To improve the quality of heteroepitaxial diamond films, the heteroepitaxial growth of diamond on Si substrates is often used as the intermediate layer. Figure 1.8 shows the scanning electron microscopy (SEM) images of heteroepitaxial diamond films on Si substrates and different intermediate layers. In this section, we describe heteroepitaxy on Si substrates for high-quality diamond films.

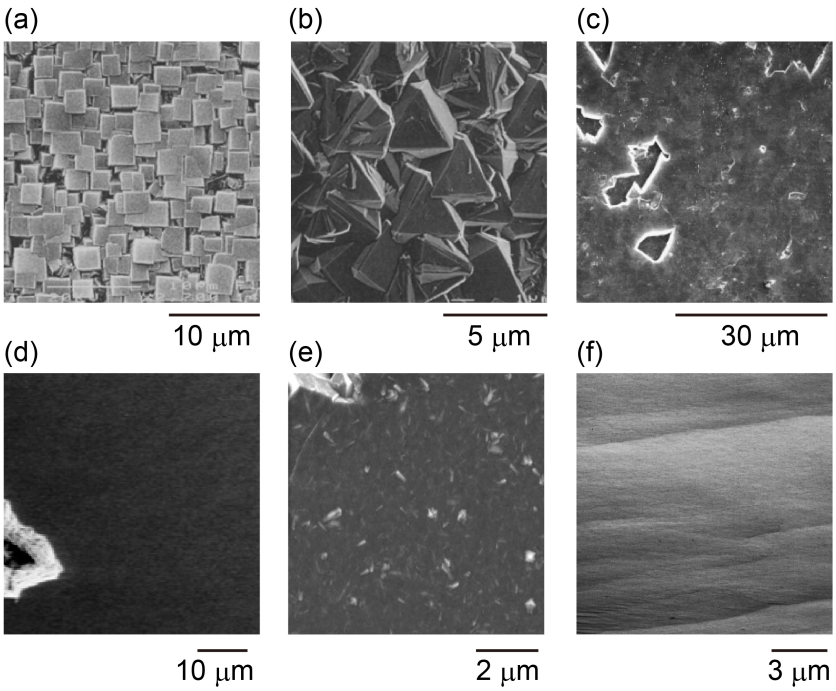

Figure 1.8: SEM images of heteroepitaxial diamond on (a, b) Si [36], (c) Pt [37], (d, e) Ir [38, 39], and (f) 3C-SiC [40]. (a, b) and (d, e) are (001) and (111) substrates, respectively.

1.4.1 Bias enhanced nucleation

As mentioned above, epitaxial diamond nuclei are rarely synthesized on non-diamond substrates except for c-BN and high carbon solubility metals with a small lattice mismatch with diamond. To synthesize a continuous diamond film on other substrates with short time (several hours), epitaxial diamond particles with nucleation density of above 10^8 cm^{-2} is required. To obtain high nucleation density diamond on non-diamond substrates, two methods are used. First, the diamond nanoparticles are put on the substrates by polishing the substrates or sonication in alcohol containing diamond nanoparticles. This method helps increase the nucleation density to above 10^8 cm^{-2}. However, the scratched diamond nanoparticles are randomly oriented, leading to polycrystalline diamond films after the growth process. The other method is called bias enhanced nucleation (BEN), reported by Yugo et al. [41]. The schematic illustration of the BEN procedure is shown in Fig. 1.9a. The negative bias voltage is applied to substrates during the diamond growth condition required for the CVD procedure. After this process, diamond nanoparticles are epitaxially nucleated on non-diamond substrates with a high density of 10^{10} to 10^{12} cm^{-2}. Lifshitz et al. suggested the mechanisms of the BEN process as follows [42, 43]: (i) The accelerated ion species (typically several hundred eV) in a plasma sheath is implanted on the substrate surface (1-2 nm), through a process called sub-implantation (Fig. 1.9b); (ii) the energetic species in the sub-surface are stopped by atomic displacement, phonon excitations, and electron excitations (i.e., thermal spikes); (iii) high-density amorphous hydrogenated carbon (a-C:H) is generated at the surface (Fig. 1.9c). The Si shallow surface is formed at the carbon-saturated layer and hydrogen atoms etch the graphitic species present on the Si surface; (iv) thermal spikes toward a-C:H leads to the formation of pure sp^3 clusters in the a-C:H phase (Fig. 1.9d). The formation probability depends on favorable boundary conditions. Amorphous carbon (a-C) transforms to diamond by preferential displacement mechanisms. Thus, diamond nanoparticles are epitaxially nucleated on non-diamond substrates. After developing this technique, the heteroepitaxial growth of diamond on the Si substrates rapidly advances.

1.4.2 Heteroepitaxial diamond film on Si substrates

Direct heteroepitaxial growth of diamond on Si substrates has been reported by some researchers. Jiang et al. synthesized a heteroepitaxial diamond film on Si substrates using

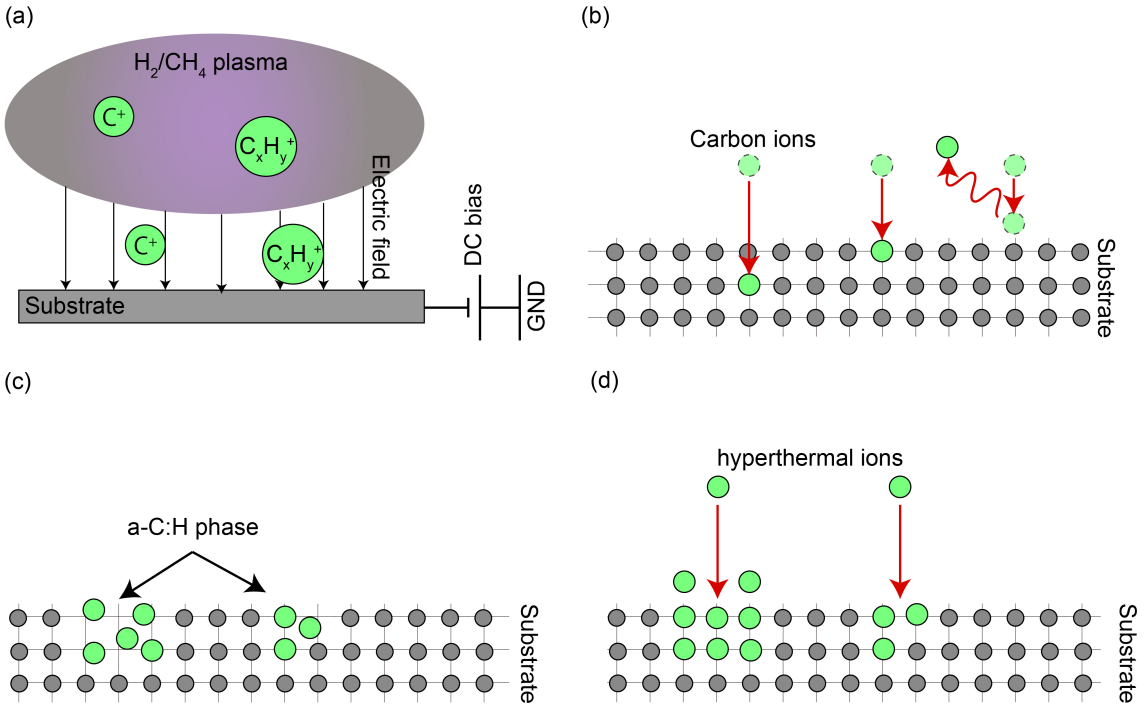

Figure 1.9: Schematic illustrates of (a) BEN method, (b)sub-implantation, (c)formation of *a*-C:H phase, and (d)formation of sp^3 cluster by hyperthermal ion.

the BEN method [44]. The use of the BEN procedure led to the synthesis of diamond nanoparticles on Si substrates with a nucleation density of an order of 10^{10} cm^{-2}, and 50 % of diamond nanoparticles are epitaxially nucleated on Si substrates. Although the Si substrates are covered with (001) diamond facets, a large tilt spread of approximately 2° is observed, instead of 7 arcseconds for single crystal diamond substrates [45]. The tilt spread of diamond films grown directly on Si substrates does not decrease on increasing the film thickness. The crystalline orientation usually improved with increasing thickness, according to van der drift's theory [46]. However, the clear grain boundaries that occur at the film surface inhibit the diamond grains from merging into each other (Fig. 1.8a, b); thus, the tilt spread of diamond films grown directly on Si substrates remains limited at around 2°.

1.4.3 Heteroepitaxial diamond film on Pt intermediate layer

Heteroepitaxial diamond films on the Si substrate has a large tilt spread because of the large lattice mismatch with diamond. Therefore, heteroepitaxial growth of diamond on Si substrates is often used for obtaining intermediate layers. Pt (111) intermediate layer is an attractive material for diamond heteropitaxy. The heteroepitaxial diamond on Pt (111) has been reported by using Si (001) and sapphire (0001) substrates. The tilt spread of 1.1° of heteroepitaxial diamond (111) on Pt/sapphire (0001) substrates [47] (Fig. 1.8c) is much smaller than that of diamond on Si (111) substrates (7°). The heteroepitaxial growth of diamond on Si (001) can be used to obtain a multi-layer of Pt(111)/SiO_x. The grown diamond films on Pt(111)/SiO_x/Si(001) [48] have a tilt spread of 3-5°, which is smaller than that diamond films grown directly on Si(111). However, the diamond films on Pt show stacking faults.

1.4.4 Heteroepitaxial diamond film on Ir intermediate layer

Heteroepitaxial growth of diamond films on Ir has been reported by Sawabe et al. [49]. Single-crystal Ir is deposited on magnesium oxide substrates; grain boundaries were not observed in the SEM image of heteroepitaxial diamond films with a thickness of around 2 μm. In the case of Ir, the diamond particles after the BEN procedure are almost perfectly epitaxially nucleated on the Ir surface (i.e., the epitaxial relationship between diamond and Ir reach to 100 %). However, Ir is not deposited directly on Si

substrates. More recently, Schreck et al. demonstrated heteroepitaxial diamond films on Ir grown on Si substrates via yttria-stabilized zirconia (YSZ) intermediate layers (Fig. 1.8d, e)[38]. The YSZ films were deposited by pulsed laser deposition on Si substrates and then Ir buffer layers were grown by e-beam evaporation with a tilt spread of 0.2°. A tilt spread of 0.02° has been reported in diamond (001) films on Ir intermediate layers. This value is much smaller than that of diamond films grown directly on Si substrates. Moreover, the diamond (111) heteroepitaxial films has also been accomplished using Ir (111) intermediate layers on YSZ/Si (111) substrates. Although the tilt spread of 0.3° is larger than that of heteroepitaxial diamond (001) films on Ir [50], the diamond surface is perfectly coalesced without twins.

1.4.5 Heteroepitaxial diamond film on 3C-SiC intermediate layer

Lee et al. has revealed that diamond can be nucleated on Si substrates through an epitaxial process via a 3C-SiC intermediate layer [51], synthesized during the BEN process, and compared with Si, 3C-SiC is more difficult to etch by ion bombardment during the BEN procedure. Therefore, the BEN procedure on Si substrates is firstly synthesized with a 3C-SiC intermediate layer before diamond nucleation. However, the CVD condition is not sufficient to grow single-crystal 3C-SiC layers; thus, the 3C-SiC layer is grown with not only a single crystal but also a polycrystalline and/or amorphous structure. This suggests that the heteroepitaxial diamond films improve if we use single-crystal 3C-SiC layers.
Therefore, 3C-SiC intermediate layers on Si substrates are also powerful intermediate layers for diamond heteroepitaxy because 3C-SiC is directly grown on Si substrates, and lattice mismatch with diamond is smaller (18 %) than that of Si (32 %). In fact, the epitaxial nucleation of diamond on 3C-SiC has been reported in some literature [52–54]. Kawarada et al. has reported perfectly coalesced, smooth, and continuous diamond films [40, 55] with a tilt spread of 0.62° on Si substrates via 3C-SiC (001) buffer layers (Fig. 1.8f), which is much smaller than that of diamond films grown directly on Si substrates. Moreover, the diamond films on 3C-SiC can also be used as metal semiconductor FET using a hydrogen-terminated diamond surface showing p-type conductivity [56, 57]. However, it has been two decades since the epitaxial nucleation of diamond on 3C-SiC was first reported, and still, that result has not yet been exceeded.

1.5 Objective of this research and structure of the study

For practical applications of diamond power and sensor devices, high-quality, high-productivity, and large-sized single-crystal diamond films are required. It is difficult to increase (more than 1 ″ in diameter) the size of homoepitaxially grown substrates. Heteroepitaxial growth of diamond is a promising technology to realize high productivity and large-sized diamond films. A 3C-SiC/Si system is a popular material for diamond heteroepitaxy because 3C-SiC can grow on Si and has a close lattice constant than that of Si. Moreover, the 3C-SiC intermediate layer has various advantages, listed as follows:

1. It is an abundant resource because 3C-SiC comprises only Si and carbon atoms.
2. It can be used with the existing semiconductor process because both Si and SiC are semiconductors.
3. Integrated devices with Si and/or SiC can be prepared.
4. Thermal stress caused by the difference in CTE between diamond and Si can be reduced by using the 3C-SiC nanocomposite interlayer.

The quality of heteroepitaxial diamond films grown on 3C-SiC/Si substrates has been improved using various methods such as by increasing the nucleation density and by biaxial stress relaxation using a nanocomposite interlayer. However, the process of heteroepitaxial growth of diamond films on 3C-SiC/Si has not yet been clarified. It is also difficult to obtain epitaxial nanocrystals in a reproducible manner. Moreover, the heteroepitaxial diamond (111) on 3C-SiC/Si substrates has not yet been reported.

In this study, we aimed to develop a nucleation technology to fabricate epitaxial diamond films on both 3C-SiC/Si (001) and (111) substrates and to evaluate their potential as power and sensor devices.

This study has been structured as follows:

In Chapter 1, the background and objectives of this study are described.

In Chapter 2, we describe the improvement and optimization of diamond nucleation on Si substrates via both 3C-SiC (001) and (111) intermediate layers using high-plasma density and by in situ monitoring the bias current. We report that the plasma density during the BEN process improve the epitaxial nucleation of diamond on 3C-SiC. We also clarify that the bias current during the BEN process well reflects the diamond nucleation process.

Thus, the optimum condition for diamond nucleation can be determined from the bias current.

In Chapter 3, we discuss the heteroepitaxial growth of diamond. The diamond (001) is nucleated on 3C-SiC by using a combination of high-plasma density and in situ monitoring of the bias current, and the best quality films were obtained. In addition, we propose the epitaxial growth method of diamond (111) on 3C-SiC by using oxygen as a growth gas. Using this technique, we obtained highly oriented diamond (111) films on 3C-SiC for the first time.

In Chapter 4, we evaluate their potential as power and sensor devices. The heteroepitaxial diamond (001) films were demonstrated as SBDs. The high rectification of 10^8 ($\pm$5 V) and specific on-resistance of 0.2 Ωcm^2, which are comparable to those of the homoepitaxial film, were obtained. The heteroepitaxial diamond (111) films were demonstrated as sensor devices using the NV centers. The NV centers in heteroepitaxial diamond films were preferentially aligned toward one atomic direction, indicating that the heteroepitaxial diamond films are promising for sensor-device platforms.

Chapter 5 summarizes this study.

Chapter 2

EPITAXIAL NUCLEATION

2.1 Background of epitaxial nucleation of diamond on 3C-SiC

Heteroepitaxial nucleation of diamond on 3C-SiC has been reported by Stoner et al. for the first time. They revealed that diamond could be nucleated on Si substrates using a 3C-SiC intermediate layer, which was synthesized during the diamond nucleation process in a mixture of hydrogen and methane gases. However, diamond was also nucleated on the Si surface directly along with an amorphous silicon carbide layer, leading to a large angular spread of > 2° for diamond on Si substrates. Heteroepitaxial 3C-SiC buffer layers on Si substrates were useful for diamond heteroepitaxy because the lattice mismatch with diamond is smaller than with that of Si, and it can be grown on Si directly. In 1995, a continuous diamond film, which was perfectly coalesced without any observable grain boundary, was reported by Kawarada et al. on 3C-SiC(001)/Si. A mosaic spread of 0.62° with a diamond film thickness of 300 μm was recorded by the X-ray diffraction (XRD) measurement, which is much smaller than that of the diamond film grown directly on Si. However, single crystal diamond synthesized under high pressure and high temperature possesses an angular spread of 7 arcseconds, corresponding to 0.002°. Thus, improving the crystal quality of the heteroepitaxial diamond on 3C-SiC is essential.

The difference in the mosaic spread of the diamond grown directly on Si substrate and the SiC buffer layer is due to the difference in the crystal orientation of the diamond nanoparticles obtained by the BEN process. To improve the quality of heteroepitaxial

diamond film grown on 3C-SiC, increase in the epitaxial diamond nucleation density and decrease in the mosaic spread of the diamond nuclei after the BEN process must be achieved. Arnault et al. reported the dependence of the surface state on diamond nucleation on both carbon-rich and Si-rich surfaces. The C 1s core X-ray photoelectron spectroscopy (XPS) intensity from the diamond grown on a C-terminated 3C-SiC surface was much higher than that from diamond grown on the Si-terminated surface. This implies that the carbon surface was beneficial for diamond nucleation. This is a possible method for increasing the diamond nucleation density to improve the quality of heteroepitaxial diamond film. The bias voltage during the BEN process is an important parameter for the heteroepitaxial nucleation on 3C-SiC. For example, on Ir buffer layers, a high bias voltage leads to the formation of laterally extending single crystal diamonds. However, for 3C-SiC, a high voltage led to the nucleation of non-epitaxial diamonds. Thus, optimizing the BEN condition is required.

Although the continuous diamond film have been reported on 3C-SiC/Si(001) substrates, it is required to improve the film quality for realizing diamond devices. Moreover, improving the heteroepitaxial diamond(001) enable to synthesizing heteroepitaxial diamond(111). Generally, heteroepitaxial growth of diamond(111) is more difficult than that of (001) because the (001) crystal face is more stable and defects are easy to form on the (111) face due to the dislocation propagation of the <111> direction and 110 slip plane system. In fact, the tilt spread of heteroepitaxial diamond(111) on Si and Ir were wider than that of (001). The diamond nucleation process determines the diamond film quality as the tilt and azimuthal spreads of diamond film strongly depend on those of nucleated diamond particles. The epitaxial nucleation of diamond nanoparticles on 3C-SiC (and also Si) by the BEN method is difficult due to the following reasons:

1. The BEN process enables to synthesize diamond nanoparticles on non-diamond substrates. However, *a*-C layers also form during this process. If the non-crystalline layers are synthesized on single-crystal substrates, the diamond nanoparticles are nucleated though the non-crystalline region, resulting in the formation of non-epitaxial diamond.

2. The diamond nucleation is performed by hyperthermal ion species which are promoted by the bias voltage as mentioned in chapter 1. However, the bias voltage has a negative effect for diamond growth. Supply of excess carbon and hyperthermal ion collide formed diamond. As a result, too long BEN process leads to the formation

of twins and nucleation of non-epitaxial diamond as well as the formation of *a*-C on nucleated diamond nanoparticles.

To solve the first problem, diamond nucleation was performed by using high-density plasma. As mentioned in chapter 1, the atomic-hydrogen has an effect to selectively etch the non-diamond species. In the CVD process, a high microwave power density promotes decomposition of molculer hydrogen rather than methane. To further improve the epitaxial nucleation on 3C-SiC at the initial step of the BEN process by suppressing formation of non-crystalline carbon, we performed the BEN process with high-density plasma which is obtained by the antenna-edge type microwave plasma (AE-MP)CVD reactor. To solve the second problem, in-situ monitoring of the diamond nucleation was performed by measuring the bias current during the BEN process. The bias current is easy to be measured and it well reflects the diamond nucleation process. So far, an optimal process window of the diamond nucleation directly on Si substrates has been reported. They determined the optimal window based on the azimuthal orientation of grown diamond films. However, the quality of the diamond nanoparticles themselves has not been correlated with the bias current. In this study, the relationship between the density and tilt spread of diamond nanoparticles and the bias current was investigated, and also the optimal process window of the diamond nucleation process was determined by in-situ monitoring the bias current.

2.2 Influence of high microwave plasma density

2.2.1 Antenna-edge type microwave plasma CVD

In this thesis, the diamond nucleation and growth are performed by MPCVD. A typical MPCVD system is shown in Fig. 2.1a, which is called ASTEX type reactor. The microwave is guided into the CVD reactor by an antenna located outside of the CVD reactor. Thus, the plasma is formed on the substrate holder at the bottom of the chamber. In this research, we used a unique CVD system so-called the AE-MPCVD (Fig. 2.1b) for the diamond nucleation process. The AE-MPCVD has advantages for the diamond nucleation as follows:

1. The electric field of the microwave is concentrated at the tip of the antenna, resulting in dramatic increase in the plasma density compared with the typical microwave plasma CVD system.

2. The antenna also works as an electrode for the BEN process. Thus, the ionic species, which are important for the BEN process, are effectively accelerated toward substrates.

The first one is important for both diamond nucleation and growth because the high plasma density makes it possible to effectively decompose the CVD gas and thus to increase diamond nucleation precursors. Additionally, the high plasma density leads to improve diamond crystal quality and growth rate. The electric fields calculated by finite element method (FEM) around substrates of both the typical CVD and AE-MPCVD are shown in Fig. 2.1b,d. The electric field of AE-MPCVD is an order of magnitude higher than that of the typical CVD system. The second one facilitates the diamond nucleation on non-diamond substrates. Diamond nuclei are synthesized by the accelerated ions by DC bias. The antenna electrode in the AE-MPCVD system effectively accelerates ionic species toward the substrate. Therefore, the diamond nucleation can be performed for a very short duration owing to the high ion flux. This is important to avoid the undesirable long-time collision of the thermal ion flux which causes damages and misorientation of the diamond nuclei.

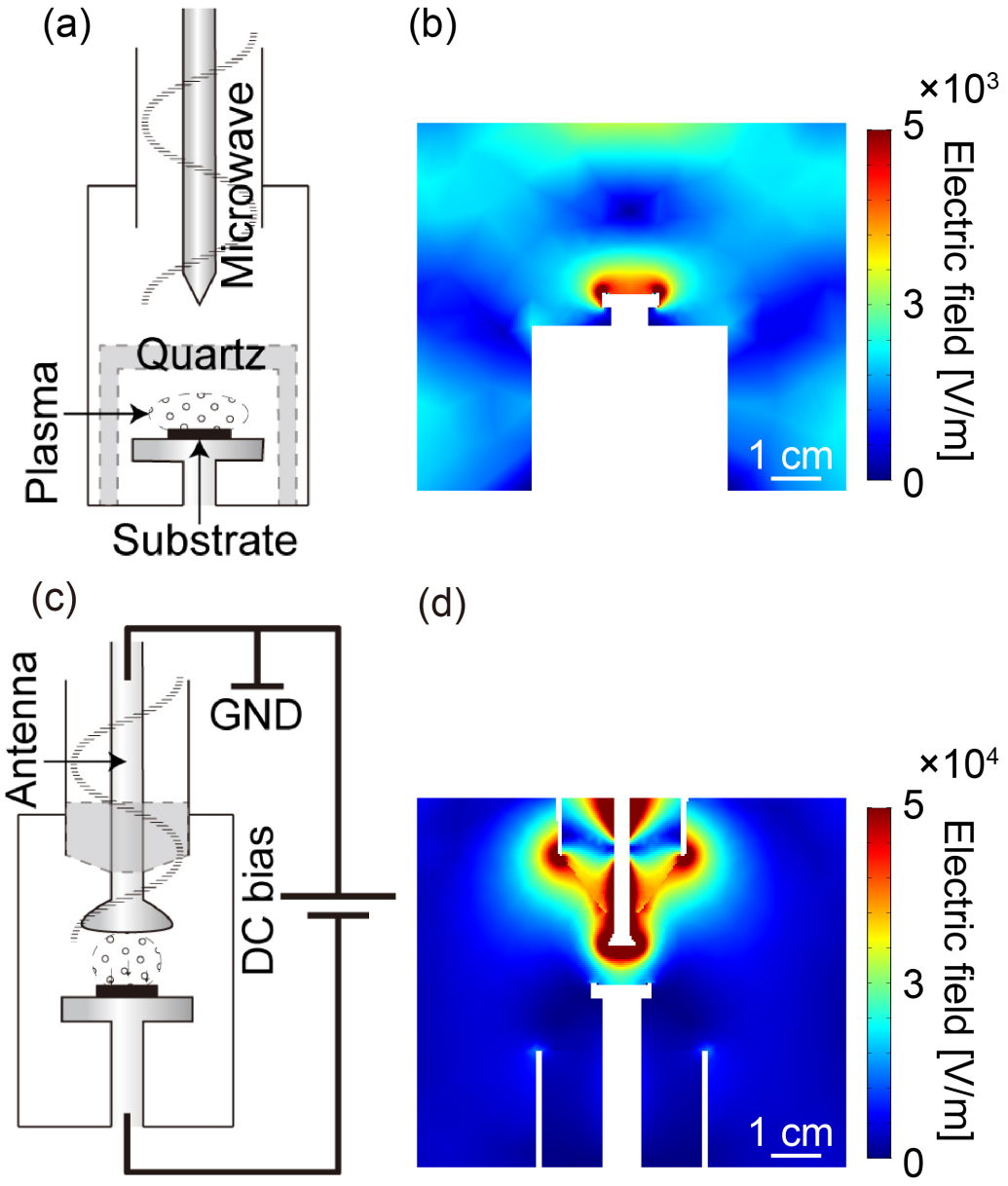

Figure 2.1: (a,b)Schematic illustrates and (c,d)electric field calculation by FEM of (a,c)ASTEX type reactor and (b,d) AE-MPCVD.

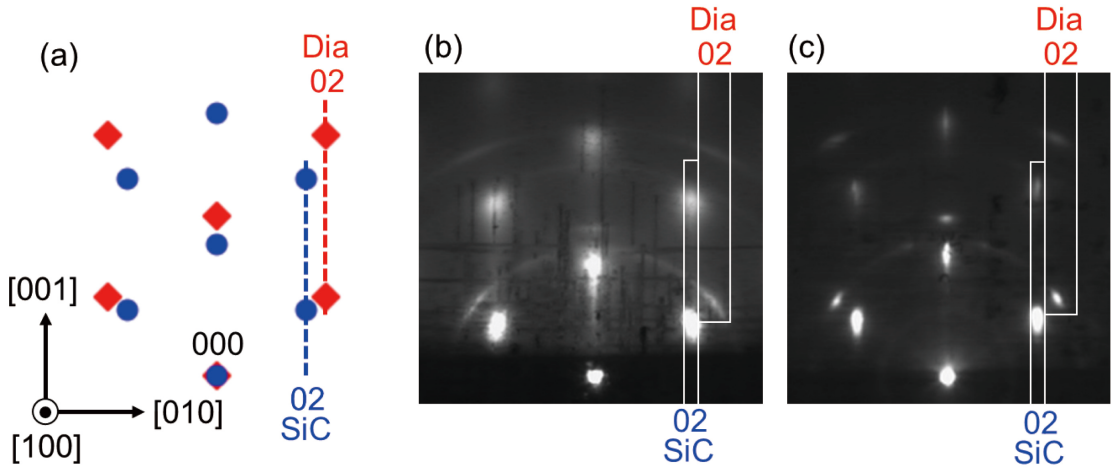

Figure 2.2: (a) Theoretical RHEED pattern with an incident beam along the [100] direction. Rhombuses and circles denote diamond and SiC, respectively. RHEED patters after nucleation under (b) low and (c) high microwave power densities. SiC and diamond [02] diffractions are indicated by the dotted lines in (a) and white squares in (b) and (c).

2.2.2 Characterization of the plasma conditions

Since AE-MPCVD can concentrate the electric field of the microwave at the tip of the antenna, the plasma density can be dramatically increased. To observe the effect of plasma power density on the diamond nucleation, the BEN procedure was performed under microwave power densities of 250 W/cm^3 at 200 W and 1100 W/cm^3 at 600 W .The power densities were estimated from the plasma volume and input microwave power. The 3C-SiC on Si(001) on-axis was used as substrates. A bias voltage of -100 V was applied during the BEN procedure. The other BEN conditions are detailed in Table A.1. Figure 2.2 shows the reflection high energy electron diffraction (RHEED) pattern after the BEN process at each microwave power. An arc-like diamond diffraction pattern was observed for a low microwave power density of 250 W/cm^3, indicating the presence of polycrystalline diamond. On the other hand, for the high-density microwave power of 1100 W/cm^3, the diffraction pattern becomes spotted, indicating that a larger amount of diamond nuclei are aligned toward the [001] direction. This dramatic change in the epitaxial relationship was caused by changing the plasma density.

We performed OES measurements to characterize plasma conditions. This method provides information on the plasma by observing the emission intensity. Figure 2.3 shows

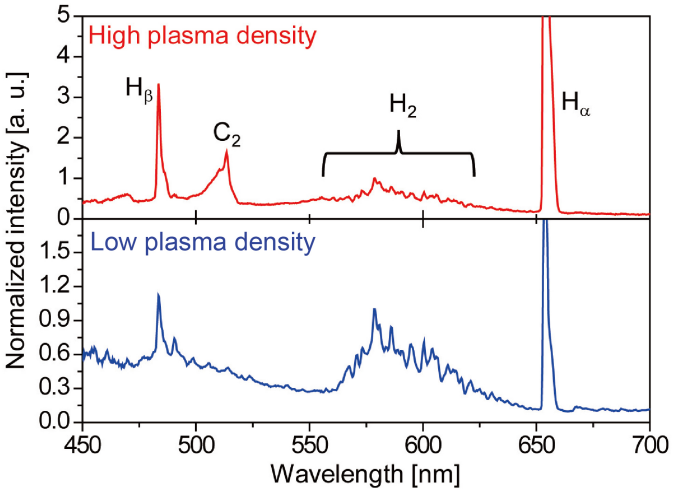

Figure 2.3: OES spectra of films grown with high (upper) and low (bottom) plasma density.

the emission spectra recorded for each microwave power density. The typical atomic hydrogen peaks of 656 nm (Balmer α : H_α) and 486 nm (Balmer β : H_β)[58] were observed. Also, the molecular hydrogen Fulcher α band[59] between 590–640 nm was observed. The intensity of the OES spectrum is described as

$$I = nAh\nu \tag{2.1}$$

The H_β/H_2 ratio reflects the population ratio in the plasma since the intensity of the OES is proportional to the population of its species. Comparing the population ratios obtained at high (1100 W/cm^3) and low microwave power (W/cm^3), the ratio of high microwave power was much higher than that of low microwave power. Silva et al. also showed that the characteristic hydrogen decomposition from molecular hydrogen was increased with increasing the process pressure, corresponding to the microwave power density. Moreover, the intensities from carbon species (CH_x and C2), which are considered as precursors of the diamond nucleation, also increased with increasing the microwave power density. Thus, the improvement of the crystal spread of diamond and nucleation density was likely to be caused by the efficient decomposition of hydrogen and the increased concentration

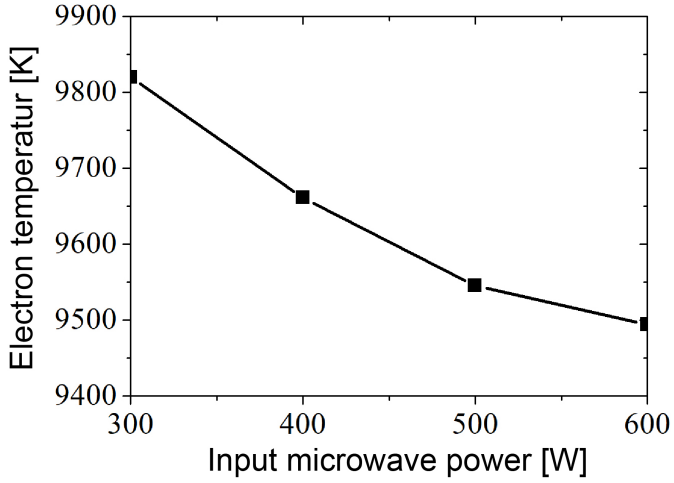

Figure 2.4: Electron temperature dependence with respect to the input microwave power.

of the methane precursor.

In order to investigate the reason for the improvement of the decomposition of hydrogen, we investigated the plasma condition in more detail. In our CVD condition, the plasma is in local thermal equilibrium. Therefore, the number ratio between the exited state and ground state is described by

$$\frac{n_i}{n_0} = \frac{g_i}{g_0} \exp\left(-\frac{E_i}{kT_e}\right) \tag{2.2}$$

where E_i is energy of exited state, k is Boltzmann constant, T_e is electron temperature, g_i and g_0 are number of degenerate of exited and ground states, respectively. Considering equation 2.1 and 2.2, the electron temperature can be calculated by using two emission intensity. If we use the intensity of H_α and H_β, the electron temperature is described as

$$T_e = \frac{E_\alpha - E_\beta}{kln\left(\frac{I_\alpha A_\alpha g_\alpha \nu_\alpha}{I_\beta A_\beta g_\beta \nu_\beta}\right)} \tag{2.3}$$

Figure 2.4 shows the electron temperature with respect to the input microwave power. The electron temperature decrease with increasing the input microwave power. This indicates the collision frequency of plasma increases with increasing the input microwave power. Therefore, the decrease of electron temperature leads to decomposed molecular hydrogen species, and it can improve epitaxial diamond nucleation on 3C-SiC surface.

2.2.3 Effect of high plasma condition

For diamond on Si substrates, the deposition of an amorphous layer was observed between the Si and diamond nuclei[60]. Cross-sectional transmission electron microscope (TEM) was performed to observe the interface between diamond and SiC, with the incident beam along the <110> direction. Although two misfit dislocations in the diamond were observed at the interface for every nine 3C-SiC lattice planes, the epitaxial diamond nuclei have clear continuous interfaces with 3C-SiC (Fig. 2.5a). Although misfit dislocations were generated, supercell matching between the nine 3C-SiC lattices (=9×4.36=39.24 Å) and eleven diamond lattices (=11×3.56=39.16 Å) (Fig. 2.5c). The supercell structure relaxes the interface stress [61] and enables the epitaxial nucleation of diamond on 3C-SiC [62]. On the other hand, non-epitaxial diamond nuclei were also observed, which nucleated on the single crystal 3C-SiC in a non-crystalline region with a tilt spread of 19° (Fig. 2.5b). In electron energy loss spectroscopy (EELS) measurements, a strong π^* peak arising from sp^2 bonded carbon atoms such as *a*-C and/or diamond like carbon [63] was observed in the non-crystalline region (Fig. 2.5d). Typical Raman spectra of the diamond grains grown for 1 hour are shown in Fig. 2.6a. Both spectra show peaks from transverse optical phonons for 3C-SiC at 794 cm^{-1} [64], diamond at 1332 cm^{-1}, and a broad band between 1400 to 1700 cm^{-1}. The broad band is thought to be sp^2 carbon impurities such as *a*-C and graphite [65]. There are two differences between the low- and high-plasma density samples. First, the high-density sample possesses a sharp diamond line at 1332 cm^{-1}, having a FWHM of approximately 10 cm^{-1} (red line of Fig. 2.6a), while it becomes wider (20 cm^{-1}) for the low-density sample. Second, the Raman band from the sp^2 carbon impurities is also smaller for the high-density sample. Figs. 2.6(b, c) show mappings of the carbon impurity band (1400 to 1700 cm^{-1}) normalized with the 3C-SiC peak (794 cm^{-1}) for the low- and high-plasma density samples. Apparently, the low-density sample includes a higher amount of impurities within the nucleation layer. Considering the OES, cross-sectional TEM, EELS, and Raman measurements, the non-crystalline carbon impurity between the diamond and 3C-SiC layers leads to nonepitaxial diamond nucleation as same as diamond nucleation on Si substrates directly, resulting in the deterioration of the subsequently grown diamond films. Atomic hydrogen is known to etch *a*-C more strongly than diamond [66]. The high-density plasma generates numerous atomic hydrogen species and inhibits the formation of *a*-C impurities. Consequently, improved epitaxial nucleation was obtained with the high-density plasma process. Thus,

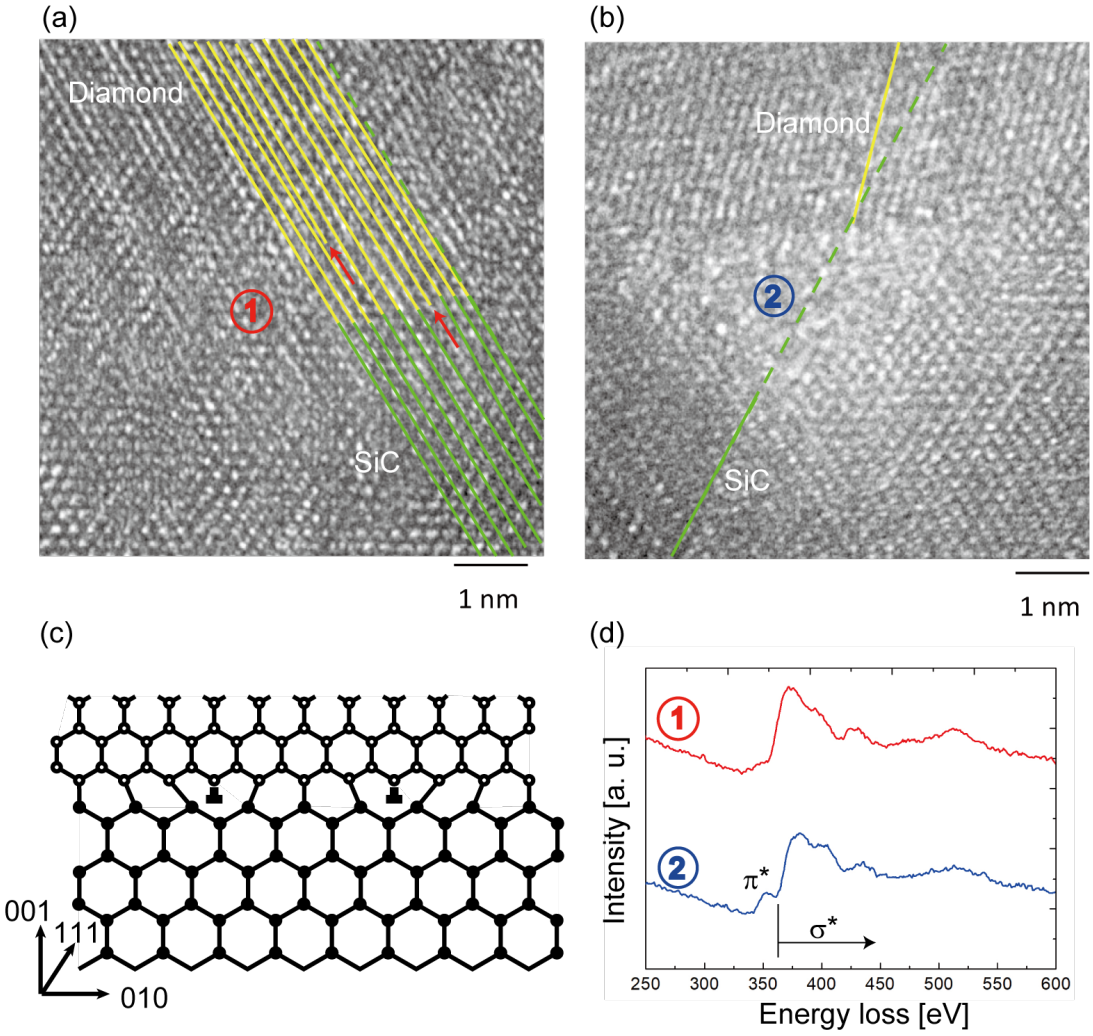

Figure 2.5: Cross-sectional TEM images of (a) epitaxial and (b) non-epitaxial interface. (c) A schematic illustrate of epitaxial diamond on 3C-SiC with misfit dislocations. (d) EELS spectrum of diamond interface. measured area marked in (a) and (b).

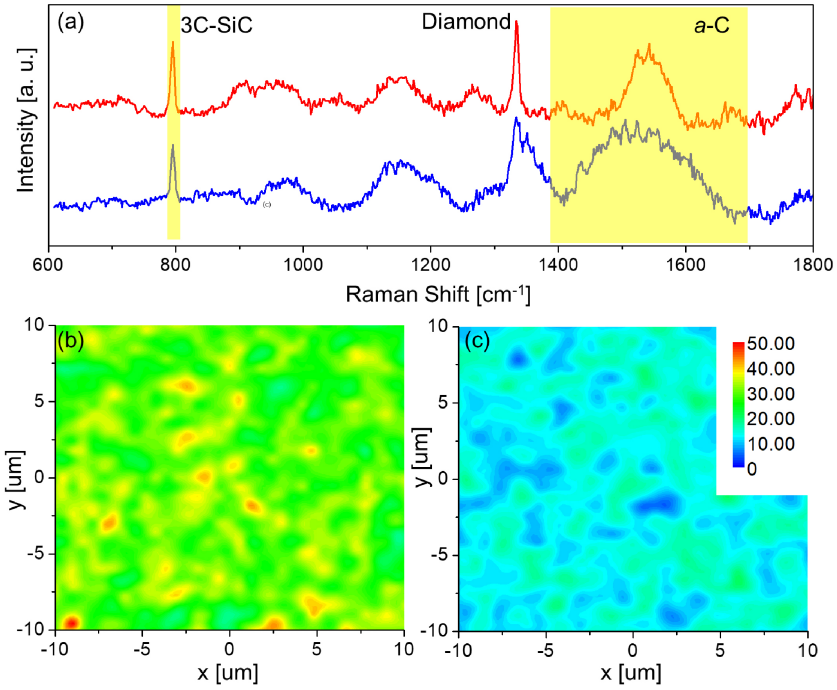

Figure 2.6: (a) Typical Raman spectra of diamond grains. Red and blue lines indicate the diamond grains nucleated by high and low microwave power density, respectively. Raman mapping of the integrated value of *a*-C component of (b) low and (c) high microwave power density normalized 3C-SiC peak. Integrated regions are shown in (a) as yellow square.

high microwave plasma density was determined to be a key condition for the formation of epitaxial diamond on the 3C-SiC substrate.

2.3 In-situ monitoring of the epitaxial nucleation by the bias current

In the previous section, the epitaxial diamond nanoparticles were formed using the high microwave power density which leads to the prevention of the formation of a-C layers at the interface between 3C-SiC and synthesized diamond. However, in the BEN process the optimal time for diamond nucleation strongly depends on the CVD system and crystal orientation, thus making it difficult to obtain epitaxial nanoparticles in a reproducible way. Therefore, in-situ monitoring of the diamond nucleation processes is necessary for achieving the reliable epitaxial nucleation.

So far, in-situ monitoring methods for the diamond nucleation have been reported. As ne method, laser reflection interferometry has been proposed for optimizing and detecting the diamond nucleation process. This method is able to measure the diamond film thickness and surface roughness [67, 68]. Another method is to measure the evolution of the bias current during the BEN process. In fact, the time variation of the bias current has been experimentally observed in previous studies according to the difference between the secondary electron emission from the substrate and diamond nanoparticles [69, 70]. An optimal process window of the diamond nucleation on Si substrates has been reported, demonstrating that the azimuthal orientation of the diamond films was deteriorated after dramatic increase in the bias current [71]. However, the relationship between the bias current variation and the state of diamond nanocrystals (i.e., density and epitaxial nucleation) has not been reported. In this section, we will describe in-situ monitoring of the formation of diamond nanocrystals by measuring the bias current changes during the BEN process, and demonstrate the optimal diamond nucleation time for obtaining the epitaxial diamond nanoparticles.

2.3.1 The bias current duration during BEN

The bias current during the BEN process reflects the information on the nucleation because the bias current density in the plasma is described by[70]

$$J_{bias} = qnE(\mu_i + \mu_e) \tag{2.4}$$

where q is the elementary charge, n is the number of electron and ion per unit area, E is electric field at the plasma sheath, μ_i and μ_e are the mobilities of ions and electrons in

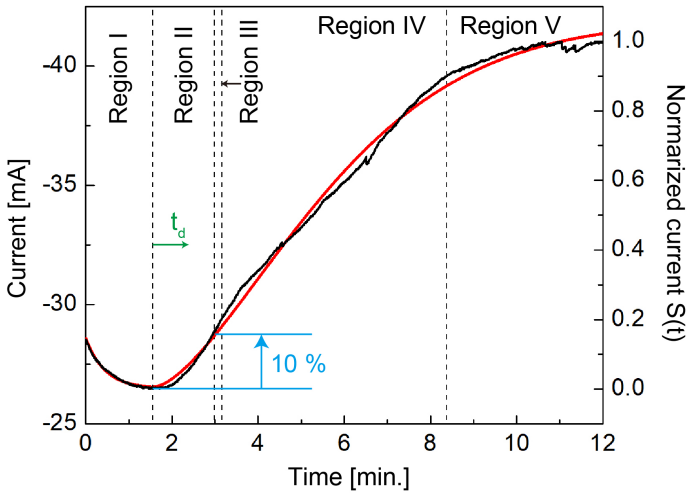

Figure 2.7: The bias current as a function of time for diamond growth on 3C-SiC/Si(001). The black line denotes the experimental results. The red line is the fitting curve using equation 2.8.

the plasma, respectively. When the diamond is nucleated on 3C-SiC surface, the electron density and electric field near the diamond become higher than those of 3C-SiC due to the high secondary electron emission coefficient of diamond. Therefore, the diamond nucleation causes change in E and n in equation 2.4. Figure 2.7 shows the bias current variations of the BEN process using the on-axis 3C-SiC/Si(001) substrates. The bias current is categorized into five regions, as mentioned in Fig. 2.7. Figure 2.8 shows the RHEED pattern, SEM, and atomic force microscope (AFM) images in each region.

Before the BEN process, the RHEED pattern of 3C-SiC shows the streak patterns, indicating very flat surface. At the Region I, the bias current decreased, and the RHEED pattern of 3C-SiC changed to spots, and no diamond diffraction was observed. The AFM image exhibited striped features along the <110> direction on the 3C-SiC surface, which may have been caused by ion bombardment during the nucleation process. The SiC surface was etched and damaged by C ions, resulting in a decrease in the bias current. This surface roughening is frequently observed at the initial step of diamond nucleation on various substrates [72].

The current reduction was gradually saturated and reached a minimum (Region II). Epitaxial diamond diffraction and particles aligned along the SiC striped structure were

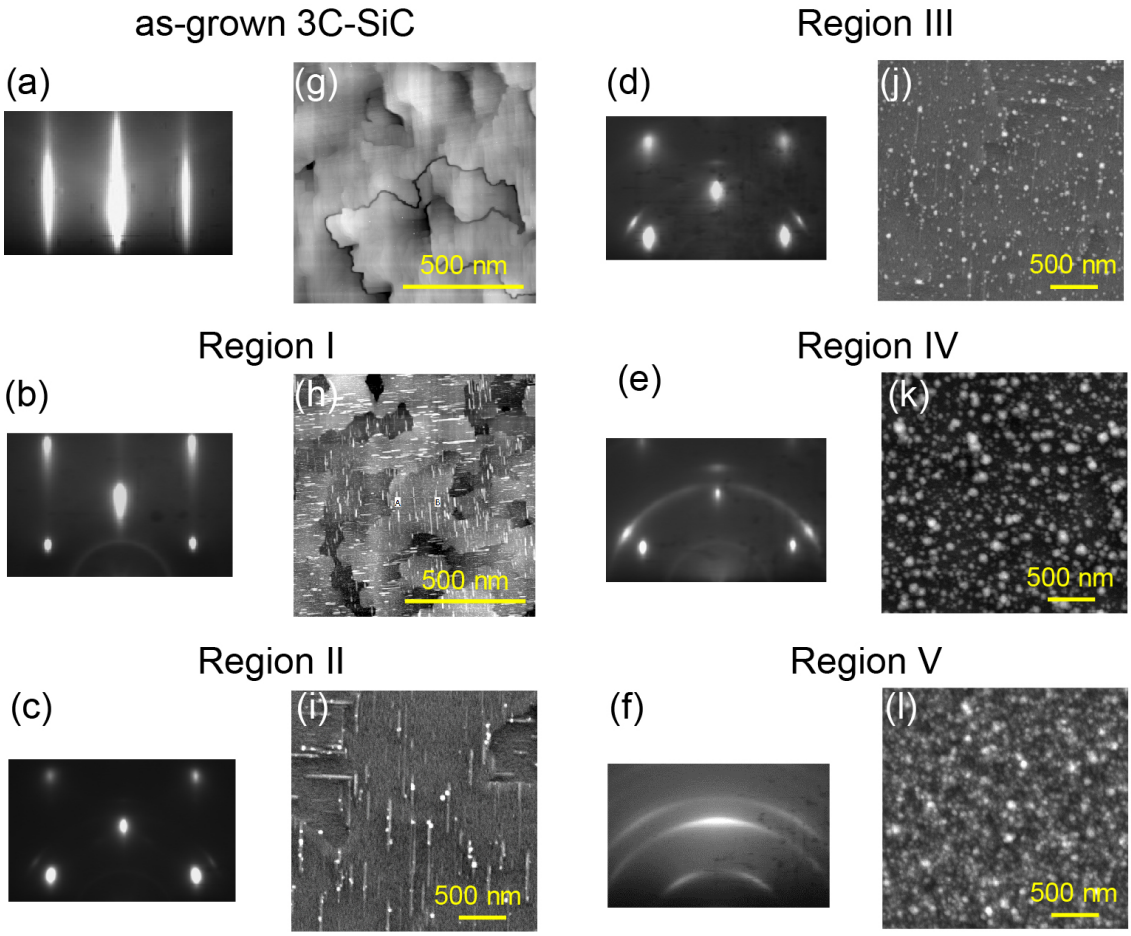

Figure 2.8: (a-f) RHEED patterns of the zero-order Laue zone with the electron beam incident along [110]. Green and red circles indicate [111] diffractions of SiC and diamond, respectively. (g-h) AFM and (i-l) SEM images of each region in Fig. 2.7. Bright particles in SEM images are the diamond nanoparticles.

observed in the RHEED pattern and SEM image. Thus, diamond nucleation was initiated in this region. Diamond possesses a high secondary electron emission coefficient, which compensates the decrease in the bias current due the roughening of the 3C-SiC, thus saturating the bias current. The diamond nucleation density (σ) was estimated to be approximately $10^9 \mathrm{cm}^{-2}$ with an average grain size (μ_g) of 25 nm. At the Region III, the bias current increased from by around 10 % (9 to 11 %) from the minimum. Strong epitaxial diamond spots were observed in the RHEED pattern (Fig. 2.8d). A high diamond nucleation density of $\sigma = 2.5 \times 10^{10}$ cm^{-2} was obtained with grain sizes of $\mu_g = 25$ nm in this region and the coverage of diamond on SiC reached approximately 16 %.

Further increasing the bias current negatively affected the diamond nucleation (Region IV). The RHEED pattern exhibited ring-like diffraction, indicating the deterioration of diamond tilt spread. Here, not only the density of diamond (3.9×10^{10} cm^{-2}) but also the diamond grain size increased ($\mu_g = 120$ nm): that is, carbon precursors were used for the growth of the diamond nanoparticles rather than the further nucleation of new diamonds. Thus, the BEN duration is too long in this region, leading to secondary nucleation[44], formation of twin structure, deterioration of epitaxial orientation due to bombardment with hyperthermal ions.

At Region V, the bias current was saturated at the maximum value. Only polycrystalline diamond rings were detected in RHEED. The whole 3C-SiC surface was covered by non-epitaxial diamond particles.

Here, we model the bias current variation based on the nucleation process. Note that we do not need to consider the current from the Mo substrate holder because the plasma in AE-MPCVD is concentrated only on the substrate. In our experiments, the diamond nucleation did not start immediately after the bias voltage applied, corresponding to region I in Fig. 2.7. Therefore, the bias current variation due to diamond need not to be considered in Region I. In this regime, the bias current decreases due to the conversion of the 3C-SiC surface structure and/or the formation of the damage to the SiC layer. The bias current variation is described as

$$I(t) = J_{SiC} exp(-t/C) S_0 \tag{2.5}$$

where J_{SiC} is the current density on the SiC surface during the BEN process, C is the time constant, S_0 is the whole substrate surface area. At $t > t_d$ which is defined as the minimum current value, the density of diamond particles continues to increase and, thus, the surface coverage exponentially increases with $1 - e^{-At^n}$ according to the Kolmogorov-

Johnson-Mehl-Avrami (KJMA) theory and reported experimental results[69, 73, 74]. Simultaneously, the coverage of 3C-SiC (bias current from diamond) decreases with $exp(-At^n)$. The bias current from diamond increases until the entire SiC surface is covered with diamond. Consequently, the bias current based on diamond is given as

$$I_{Dia}(t) = \begin{cases} 0 & (t < t_d) \\ J_{Dia}S_0(1 - e^{-A(t-t_d)^n}) & (t > t_d) \end{cases} \tag{2.6}$$

where J_{Dia} is the current density on the diamond surface, A is the constant value, n is the Avrami exponent. In contrast, the bias current based on 3C-SiC is given as

$$I_{SiC}(t) = \begin{cases} J_{SiC}S_0e^{-t/C} & (t < t_d) \\ J_{SiC}S_0e^{-A(t-t_d)^n} & (t \geqq t_d) \end{cases} \tag{2.7}$$

Thus, the change in the total bias current is described by

$$I(t) = \begin{cases} J_{SiC}S_0e^{-t/C} & (t < t_d) \\ (J_{SiC} - J_{Dia})S_0e^{-A(t-t_d)^n} + J_{Dia}S_0 & (t \geqq t_d) \end{cases} \tag{2.8}$$

The curve fit of this equation is in good agreement with the experimental bias current shown in Fig. 2.7. From the fitting, the surface coverage of diamond is estimated to be 17 % at the 10 % increase in the bias current. This value is almost same as that estimated from the SEM image in region III (Fig. 2.8j).

Here, we show that monitoring the bias current in-situ also works for the diamond nucleation on 3C-SiC/Si(111) substrates with an off-angle of 2.5° toward $[\overline{1}\overline{1}2]$ direction. We nucleated diamonds using a short-time nucleation process called pulsed BEN. The nucleation conditions are listed in Table A.2, and the evolution of the bias current during the nucleation is shown in Fig. 2.9, which is similar to that of the (001) substrate. The only difference was a constant value of A and incubation time t_d in equation 2.8, which depends on the CH_4 concentration and/or crystal orientation. Although the nucleation time on the (111) substrate was shorter than that of (001), we could obtain a high density of epitaxial diamond nanocrystals of 10^{10} cm^{-2} (Fig. 2.8) in the same manner, i.e., at the time when the bias current increased by 10 % from the minimum bias current.

2.3.2 Nucleation process analysis by Avrami exponent

The current density is changed due to the formation of the diamond particles because of changing the electric field and high electron emission efficiency of diamond. The time

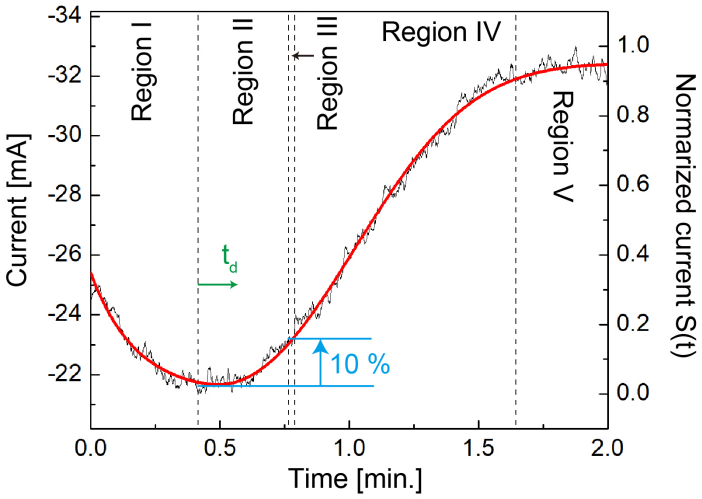

Figure 2.9: The bias current as a function of time for diamond growth on 3C-SiC/Si(111). The black line denotes the experimental results. The red line is the fitting curve using equation 2.8.

dependence of surface fraction of the diamond ($S(t)$), corresponding to the normalized bias current, (shown in Fig. 2.7 and 2.9) follows the KJMA equation as follows

$$S(t) = 1 - \exp(-At^n) \tag{2.9}$$

We fitted the bias current using this theory, and it is good agreement with experimental data. However, it is known that the Avrami exponent (n) frequently depends on the time due to the change of surface condition [75]. The nucleation and growth process can be estimate by the Avrami exponent. In order to obtain the time dependence of Avrami exponent, the KJMA equation is transformed into

$$\ln(-\ln(1 - S(t))) = n\ln(t) + \ln(A) \tag{2.10}$$

the Avrami exponent (n) can be estimated by the KJMA plot (i. e. $\ln(-\ln(1 - S(t)))$ vs $\ln(t)$). Figure 2.10 shows the KJMA plot in region II-IV. The slope of the curve corresponds to the Avrami exponent. We found that the slope in Region III has an Avrami exponent of 4. The further analysis can be performed by considering the Avrami exponent with the following relationship then the Avrami exponent is described by [76]

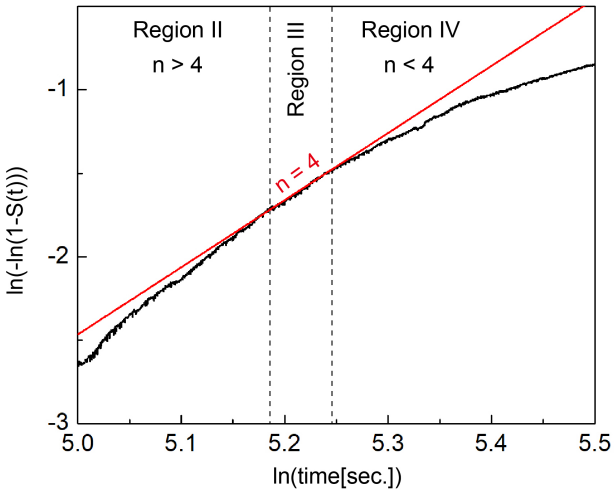

Figure 2.10: KJMA plot of the diamond (001) nucleation process. The black and red lines indicate the experimental data and line with n=4, respectively.

$$n = b + mp \tag{2.11}$$

where b indicates the nucleation rate, m and p indicate the growth mode. The nucleation rate is described as follows: (i) $b > 1$: increase in the nucleation rate with time; (ii) $b = 1$: the constant nucleation rate; (iii) $0 < b < 1$: decrease in the nucleation rate with time; (iv) $b = 0$: no nucleation. The three possible values for m are 1, 2, and 3 correspond to the growth mode of one-, two-, and three-dimensional growth mode, respectively. p can take 1 when the diamond growth is diffusion-controlled and p is 0.5 when the diamond growth is non-diffusion-controlled. In Region III, the Avrami exponent 4. In this region, the diamond particle size of 25 nm was observed in the experiment (Fig. 2.8j). Since it has been reported that the diamond nanoparticles grow with the non-diffusion-controlled growth when the size of the nanoparticles less than 60 nm, the value of p is 0.5. In fact, the size of the diamond nanoparticles hardly changes from Region II to Region III. Moreover, m = 3 is assumed because the diamond nanoparticles larger in the three-dimension. Therefore, the $b > 1$ was obtained from equation 2.11. This indicates that the diamond nucleation rate is not saturated yet. For the same reason, n > 4 in Region II means that the nucleation rate of the diamond particles increases with time. In fact, the diamond nucleation density was increased by a factor of 10 between Region II and III.

This result suggests that nucleation of diamond continued to occur from Region II to III. In contrast, n < 4 was obtained from the KJMA plot in Region IV. In the experimental data, the diamond particle size was up to 120 nm, indicating the $p = 1$ because the diamond grow with the diffusion-controlled growth in this region. Therefore, $b < 1$ is obtained in this region, indicating the decrease in the diamond nucleation rate and/or no diamond nucleation after this region. Comparing with the experimental results shown in Fig. 2.8, the nucleation density increased with only 2 times or less, whereas the size increased between Region III to Region IV. This suggests that the diamond was grown in Region IV rather than the nucleation. Therefore, the bias current increased by 10 % from the minimum is the limit of the generation of new diamond nanoparticles, and deterioration of the crystal orientation and secondary nucleation are occur in Region IV due to the collision of hyperthermal ions to the synthesized diamonds. Summarizing the diamond nucleation density and its crystalline size, the diamond nucleation density is dramatically increased after the incubation time (t_d). However, the newly synthesized nanoparticles are limited by current increases of 10 % from the minimum, corresponding to the Avrami exponent of 4. Therefore, the optimum condition for the diamond nucleation can be determined by the bias current change during the BEN process. The in-situ monitoring of the bias current was also performed on 3C-SiC(111)/Si(111) substrates. An Avrami exponent of 4 was obtained in Region III indicating that this monitoring method can be applied to any crystal orientation to optimize the epitaxial diamond nucleation.

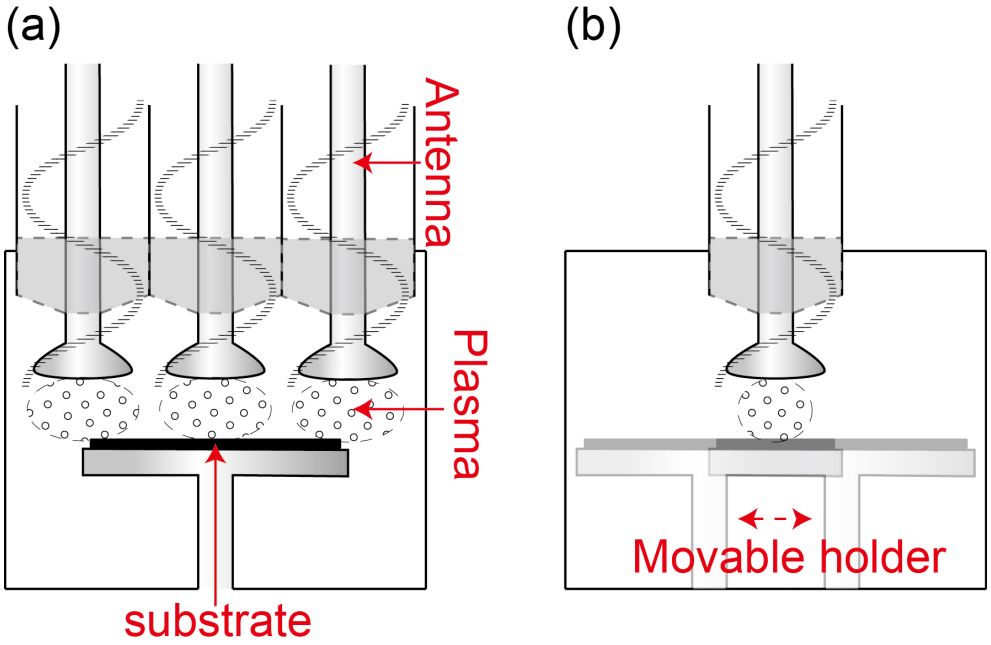

Figure 2.11: Schematic illustrates of (a)multi AE-MPCVD and (b) large-area nucleation by scanning whole substrate area.

2.4 Large-area nucleation

We have performed diamond nucleation on 3C-SiC by using AE-MPCVD to concentrate the electric field at the antenna edge. Although the electric field of an order of 10^4 V/m was calculated from FEM, the plasma generation area was limited to the antenna diameter of 1 cm. In order to increase the area of the diamond nucleation, it is necessary to perform the nucleation over the whole Si substrate. As the outlook of research, the following two methods are considered to obtain the large-area diamond nucleation. Importantly, there is a trade-off relationship between the microwave power density and uniformity [77].

1. Increase the plasma generation area by increasing the number of the antenna (Fig. 2.11a): In order to widen the plasma generation region with the same electric field, a large microwave power is necessary. A large-area growth of diamond film, however, the microwave power of an order of kilo watt is used. Since we use less than 1 kW in this thesis, we would achieve it by increasing input microwave power. Large-area nucleation would be accomplished using multi-antenna CVD and high input microwave power. It is a future work that concerns about nonuniformity at the

interface with adjacent plasma

2. Nucleation of diamond by moving the substrate or antenna: The plasma is fixed at the tip of the antenna in the AE-MPCVD system. However, if the antenna or substrate is scanned over the whole substrate area with the optimized BEN time at each position, uniform and large-area diamond nucleation is expected to be obtained. Our CVD configuration can move the antenna and/or substrate holder as shown in Fig. 2.11b. In the case of multi-antenna, heterogeneous of the microwave power density at the plasma interface considered to be a problem. The movable substrate holder can be useful for homogeneous nucleation of diamond with large-area.

2.5 Conclusion

We have performed epitaxial diamond nucleation on both 3C-SiC(001) and (111) intermediate layers on Si substrates. The diamond nucleation on 3C-SiC by the BEN method formed the non-crystalline layer at the interface between diamond and 3C-SiC as same as diamond nucleation on Si. In order to selectively inhibit the non-crystalline region, we have used the high microwave power density which can be obtain applying the AE-MPCVD. The AE-MPCVD can increase the decomposition of molecular hydrogen species due to high electric field. Thus, the non-crystalline region at the interface was inhibited by the well decomposed hydrogen species. In addition to inhibit the interface non-crystalline carbon species, we have also performed in-situ monitoring of diamond nucleation during the BEN process. The bias current variation during BEN process reflects the surface coverage of diamond and its nucleation and growth process can be estimated by the Avrami exponent. As a result, we have obtained the epitaxial diamond nanoparticles on both 3C-SiC(001) and (111) using combination of high plasma density nucleation and optimizing nucleation time by in-situ monitoring during the BEN process.

Chapter 3

HETEROEPITAXIAL GROWTH

3.1 Heteroepitaxial growth of diamond(001)

The diamond(001) is a basic substrate for diamond applications because of the high growth rate in the [001] direction, reaching 150 μm/h [78]. The diamond nuclei on Si(001) directly formed by BEN process are not perfectly oriented and have an angular spread. To remove misoriented diamond nuclei, a two-step growth method was performed based on evolutionary selection [79], which occurred due to the difference in the growth rates between <001> and <111>. During the first step, the diamond nuclei were preferentially grown in the <001> direction. In this process, the misoriented diamond particles were buried, forming a pyramidal structure governed by Wulff construction. Then, during the second step, preferential growth in the <111> direction was performed to merge and flatten the diamond surface. The difference in the growth rates between the <001> and <111> directions is defined as the α-parameter [79].

$$\alpha = \sqrt{3}\frac{V_{001}}{V_{111}} \tag{3.1}$$

where V_{001} and V_{111} are the growth rates in the <001> and <111> crystalline directions, respectively. Generally, α values range from 1 to 3 according to the law of Wulff construction. A high value of 3 (i.e. $V_{001} = \sqrt{3}V_{111}$) is obtained by the CVD growth under conditions of high methane concentration, low temperature, or nitrogen atmosphere. In order to more improve the tilt spread of diamond films on Si substrates directly, the two-step growth process has been applied. Wild et al. has reported the highly-oriented diamond(001) film on Si substrates even though the diamond particles on Si substrates

were nucleated by “ scratch ” method, by which the nuclei were not epitaxially formed on Si substrates [79]. The two-step growth process occurs as follows:

1. The nucleated diamond nanoparticles are preferentially grown to <001> directions. In this process. The diamond nanoparticles not facing the [001] direction are buried in the diamond facing the [001] direction based on van der drift's theory. According to Wulff's construction, the crystalline facets with the fastest growth rate disappears, and the other crystalline facets are appear. In this condition, the growth rate of the <001> directions are faster than that of the <111> directions. Thus, the diamond grains form pyramidal structures (Fig.3.1b).

2. After most of the diamond grains not facing the [001] direction are buried, they are preferentially grown to the <111> directions. In this process, the (001) facets appear instead of the (111) facets and they merge with neighboring diamond grains. Finally, the Si substrate is covered by the (001) diamond facets. (Fig. 3.1c)

Using this technique, the highly-oriented diamond (001) films has been formed in spite of diamond nanocrystal with several angular spreads on Si substrates. The heteroepitaxial diamond on Si substrates has been demonstrated using this technique. However, the diamond nanoparticles on Si substrates have several angular spreads of > 2° because of large lattice mismatch with diamond. As a result, the diamond grains are not perfectly coalesced and thus, the heteroepitaxial diamond film shows grain boundaries. In contrast, a continuous heteroepitaxial diamond films on 3C-SiC has been achieved by utilizing diamond nanoparticles with a smaller tilt spread after the BEN process [40]. In this research, the two-step growth method was applied to the diamond nuclei formed by AE-MPCVD to obtain continuous heteroepitaxial diamond(001) films. Dislocations in heteroepitaxial diamond films are also important for the design and function of diamond-based electronic devices. Generally, heteroepitaxial film have high-density dislocations caused by differences in the lattice constant between the substrate (or buffer layer) and diamond.

3.1.1 Two-step growth process

The diamond nanoparticles nucleated with the high and low microwave power densities were further processed using the two-step growth method to obtain diamond films. Figure

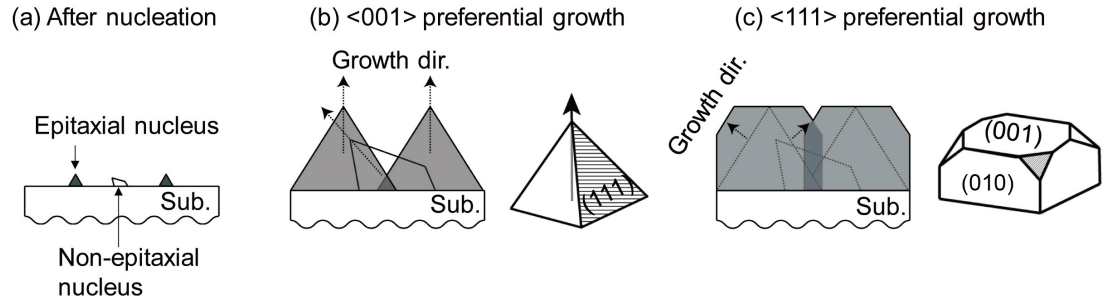

Figure 3.1: Schematic illustration of the two-step growth process.

3.2a,d show the SEM images of the diamond nanoparticles after the BEN procedure under low and high microwave power densities, respectively. In the first step, diamond nuclei were grown in a gas mixture of 4 % methane and 120 ppm nitrogen in hydrogen. Nitrogen was essential for the acceleration of the <001> direction growth. Pyramidal-shaped diamond grains were observed with the same azimuthal orientation (Fig. 3.2b,e). However, non-epitaxial diamond grains were also observed (Fig. 3.2b). In contrast, all diamond grains formed based on the nanoparticles by the high microwave power possess the pyramid-shaped structure, which indicates that the diamond grains have an epitaxial relationship with the 3C-SiC buffer layers. Next, the diamond grains were laterally grown to obtain a film by adjusting the α-parameter. In this process, diamond grains were grown in a gas mixture of the same methane concentration and 0.25 % oxygen in hydrogen. The nitrogen gas was not added to reduce the α-parameter. Oxygen was used to improve the crystallinity of the grown heteroepitaxial diamond film. Despite the utilization of the identical processes, grain boundaries were observed in the diamond films based on the nanoparticles formed with the low microwave power density (Fig. 3.2c), whereas diamond films originating from the nanoparticles formed with high density plasma showed a continuous film with no grain boundary (Fig. 3.2f). This confirms that the quality of the heteroepitaxial diamond film can be improved by using the high density plasma. XRD measurements were performed to measure the mosaic spread of the continuous diamond films. Figure 3.3a shows the FWHM of the (004) XRD ω-rocking curve as a function of film thickness. Thick diamond films were synthesized on the 3C-SiC/Si substrates with an off angle of 3° towards the [110] direction, promoting the frank van der merwe (FM) (i.e. the step-flow) growth mode. The thin diamond layer approximately 20 μm in thickness showed a large FWHM of approximately 1°. As the film thickness increases,

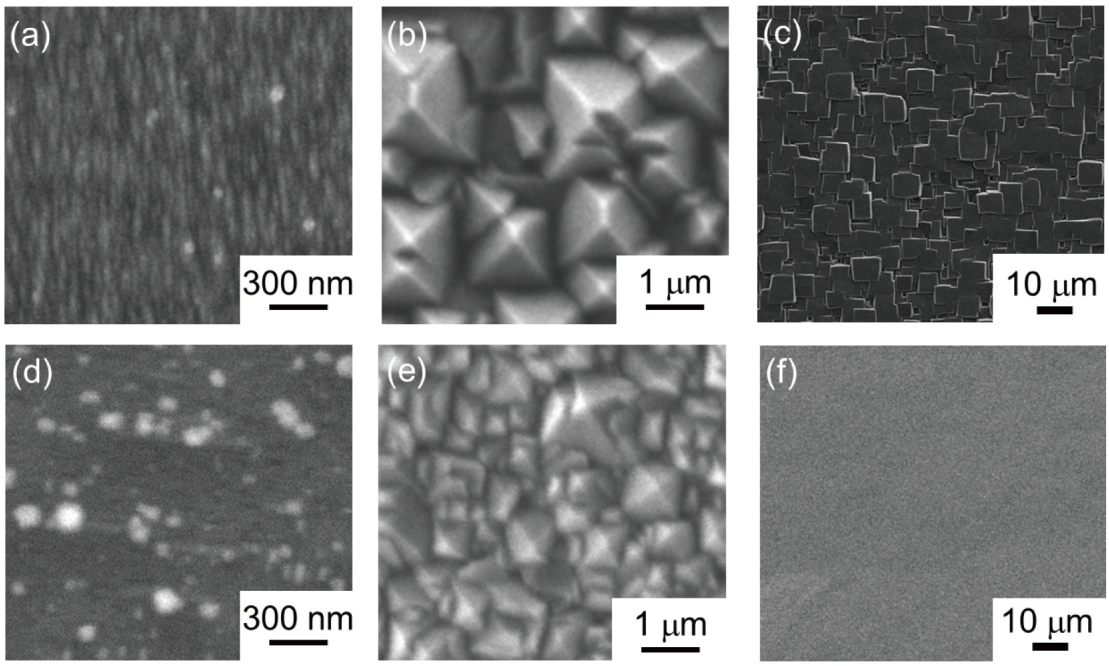

Figure 3.2: SEM images after (a, d) the BEN process, (b, e) <001> preferential growth, and (c, f) <111> preferential growth. (a-c) and (d-f) were for diamond nanoparticles formed under the low and high plasma density, respectively.

the FWHM dramatically decreases and reaches a value of 0.52° at a thickness of 75 μm. The optical microscope (OM) image of the 75 μm thick diamond film (Fig 3.3b) shows a step-terrace diamond structure covering the whole 3C-SiC surface. The FWHM of 0.52° obtained from the 75 μm thick film is smaller than that in a previous report (0.62 ° for a film thickness of 300 μm)[40] and, to the best of our knowledge, is the smallest value for reported diamond films grown on a 3C-SiC/Si(001) system to date.

3.1.2 Residual stress and dislocations in diamond film

The residual stress in the diamond films lead to the increase of curvature. Heteroepitaxial diamond films usually have high residual stress caused by misfit dislocations and difference of CTE. The stress in diamond films caused by the difference of CTE between diamond and Si is described by

$$\sigma_{thermal} = Y_{Diamond} \int_{T_0}^{T_{Gr}} (\alpha_{Diamond} - \alpha_{Si}) dT \tag{3.2}$$

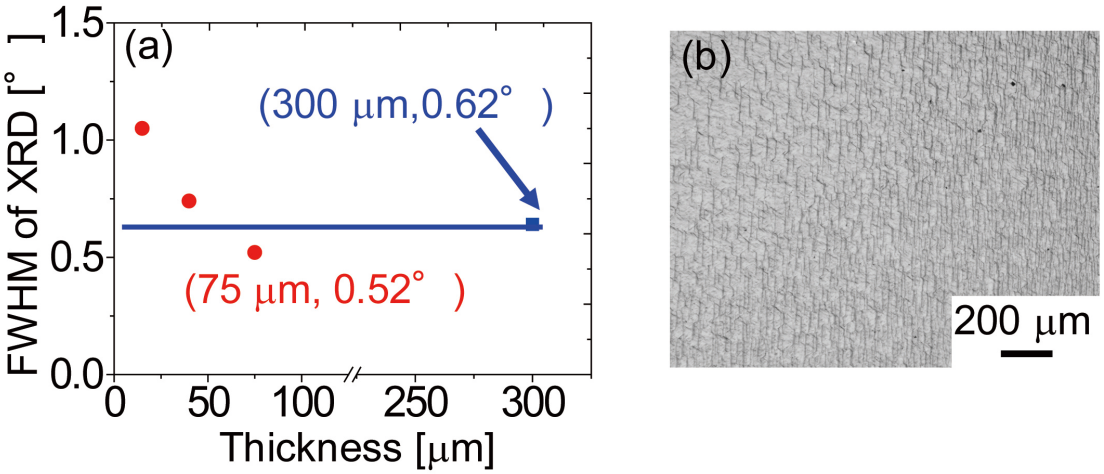

Figure 3.3: (a) FWHM of XRD (004) rocking curve of heteroepitaxial diamond as a function of the film thickness. 0.62° at a thickness of 300 μm is the smallest value previously reported in ref inset. (b) OM image of the diamond film with a FWHM of 0.52° at a thickness of 75 μm.

where $Y_{diamond}$ is conversion elastic constant of diamond, T_0 and T_{Gr} are temperature of after and during growth, respectively. The stress in the diamond films at the surface caused by difference of CTE is described as

$$\sigma_{surface} = \frac{A\sigma_{thermal}}{B} \tag{3.3}$$

where A and B is defined as

$$A = 1 + \frac{1}{h_{cov}Y_{cov}} - 3\left(1 + \frac{1}{Y_{cov}}\right) \tag{3.4}$$

$$B = \left(1 + \frac{1}{Y_{cov}}\right)^3 \times \left(\frac{1 + h_{cov}Y_{cov}^3\left(1 + \frac{1}{h_{cov}Y_{cov}}\right)}{1 + \frac{1}{Y_{cov}}^2}\right) \tag{3.5}$$

and

$$h_{cov} = \frac{h_{Si}}{h_{dia}} \tag{3.6}$$

$$Y_{cov} = \frac{E_{dia}(1 - u_{dia})}{E_{Si}(1 - u_{Si})} \tag{3.7}$$

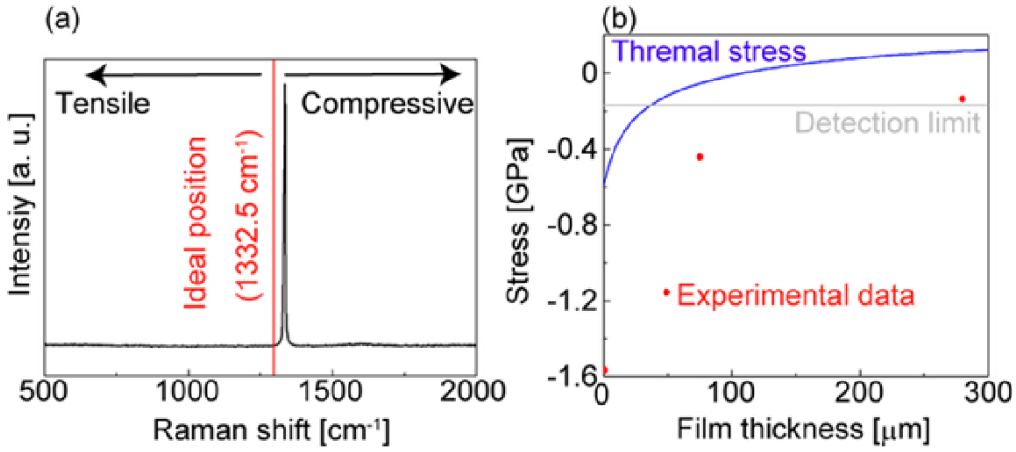

Figure 3.4: (a) Raman spectrum of a diamond films in thickness of 280 μm. (b) Average residual stress in the diamond films as a function of the film thickness. Red point and blue line donate the experimental results and theoretical stress caused by the difference of CTE between Si and diamond, respectively.

where E_{Si} = 130 MPa and E_{dia} = 1141 MPa are elastic constant, u_{Si} = 0.28 and u_{dia} = 0.07 are Poisson's ratio, h is film thickness. The biaxial stress in the diamond film can be estimated by Raman scattering spectroscopy with the following relation [80]

$$\sigma = 0.34 \times (\nu - \nu_0) \tag{3.8}$$

where ν and ν_0 are the measured Raman shift of diamond films and theoretical position of diamond Raman peak at 1332.5 cm^{-1}, respectively. Fig. 3.4 shows a Raman spectrum of the heteroepitaxial diamond(001) film and the estimated average residual stress. The diamond film shows a Raman shift of 0.84 cm^{-1}, higher than the ideal position. This means that the film possesses the compressive stress. The experimentally obtained stress in the diamond film is much higher than the theoretical stress calculated from the difference of CTE between the diamond and Si substrate. The extra stress in diamond film would be caused by low angle grain boundaries [81] and/or dislocations [82] in the film. Chemical etching, such as with oxygen plasma treatment, was used to estimate the dislocation densities in the diamond film [83]. Etch pits are formed at the dislocations by the oxygen plasma. Figure 3.5a shows an AFM image of an etched diamond surface. The process was performed in a gas mixture of 1 % oxygen in hydrogen for 5 minutes in the CVD chamber. Inverse pyramid pits were observed on the diamond surface, and the dislocation density

can be estimated by counting the number of the etch pits in a given area. It has been reported that the dislocation density of the heteroepitaxial film is reduced as increasing the film thickness for diamond on an Ir buffer layer [84] and for GaAs on Si substrates [85]. Figure 3.5b shows the dislocation density of the diamond film grown on the 3C-SiC buffer layer estimated from the etch pit density of the AFM images as a function of the film thickness. The dislocation density decreases as the film thickness (h) increases. At a film thickness of 280 μm, a dislocation density of 10^8 cm^{-2} was obtained, which is close to that of a heteroepitaxial diamond grown on Ir with the same diamond film thickness. The dependence of the dislocation density on the film thickness can be separated into two distinct regions. The dislocation density depends on 1/h in the region of the film thickness < 75 μm. On the other hand, when the film thickness is > 75 μm, a lower dislocation density is obtained and has an exponential relationship with the film thickness. The scaling laws of the dislocation density of the heteroepitaxial diamond film on 3C-SiC can be given by [85]

$$N(h) = \frac{1}{\left(\frac{1}{D_0} + \frac{b}{a}\right) e^{ah} - \frac{b}{a}} \tag{3.9}$$

where $D_0 = 2.4 \times 10^{12}$ cm^{-2} is the dislocation density at the diamond and 3C-SiC interface, estimated from the cross-sectional TEM image, and a and b are fitting parameters. Note that a and b were defined as

$$a = n\sigma \tag{3.10}$$

$$b = kl_0 \tag{3.11}$$

where n is the cross section of dislocation area, σ is concentration of the scattering matter, $k = 1$ is used for the diamond structure, in which the dislocations propagate to the <110> direction and (001) surface, and l_0 is the reaction distance between two neighboring dislocations. In the high dislocation density area, the distance between neighboring dislocations is within l_0; thus the dislocations merge with neighboring ones and their number is dramatically decreased [86]. In contrast, the dislocations do not merge with their neighbors in the low dislocation density area, and instead participate in cyclic reactions with themselves. Thus, the number of dislocations in the heteroepitaxial diamond were decreased with increasing film thickness.

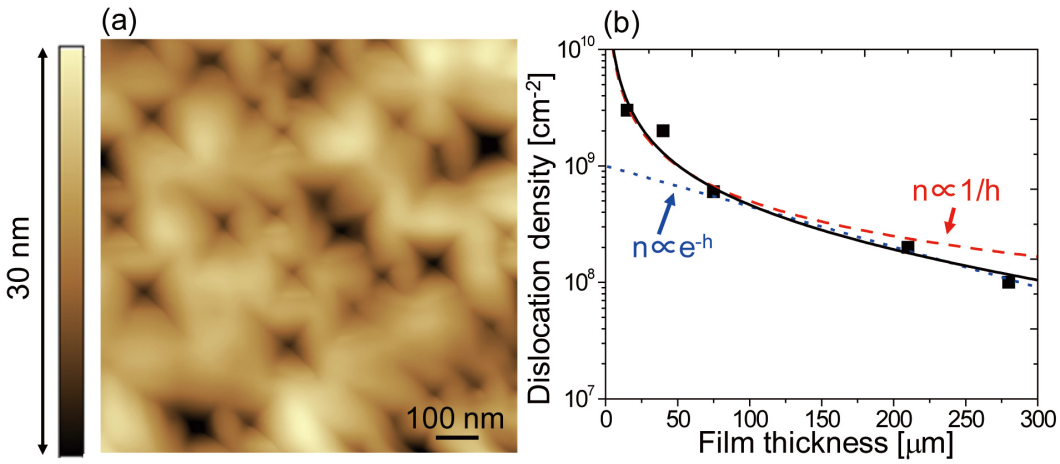

Figure 3.5: (a) AFM image of the diamond surface with a thickness of 15 μm after H_2/O_2 plasma treatment for 5 min. (b) Dislocation density as a function of diamond film thickness. Solid line denotes the fitting using equation 3.9, respectively.

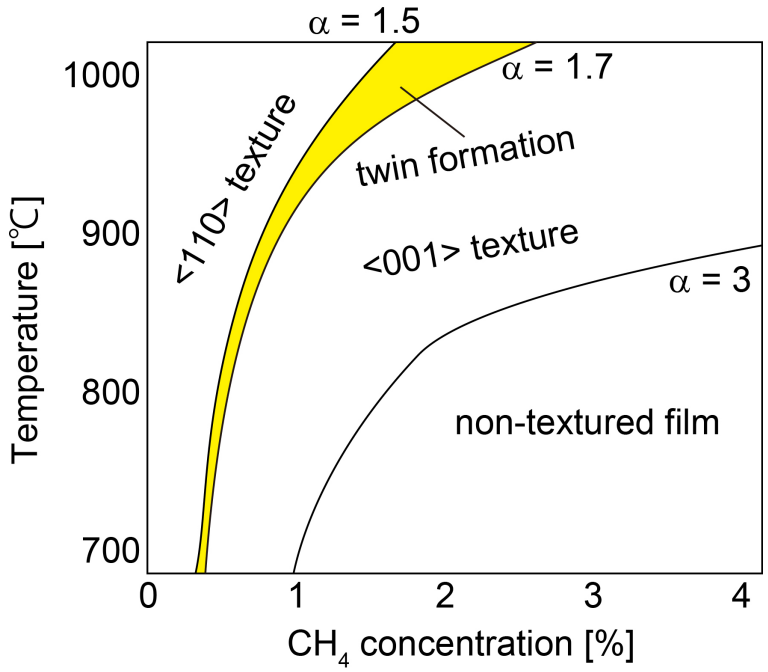

Figure 3.6: Dependence of the film texture on the different methane concentration and temperature [87].

3.2 Heteroepitaxial growth of diamond(111)

Heteroepitaxial growth of diamond(111) has been previously reported on Si(111) [36], Ir(111) [39], and Pt(111) [37]. The mosaic spreads of the heteroepitaxial (111) diamond films were larger than that of (001). This indicates that (111) diamond heteroepitaxy is more difficult compared to the growth of the (001) diamond. For the diamond(001), non-epitaxial diamond particles can be easily buried in the epitaxial grains using a high α-parameter. On the other hand, the growth rate of the (111) diamond is usually slower and the twin formation also occurs on the (111) diamond facets under α-parameter ranges from 1.5 to 1.7 [87]. Moreover, epitaxial diamond(111) particles are buried in <110> diamond particles under low α-parameter as shown in Fig. 3.6, making it hard to control its growth conditions compared with the diamond(001) growth. Thus, the two-step growth methods which was used for the diamond(001) heteroepitaxy cannot be applied to the heteroepitaxial growth of the diamond(111). For this reason, the heteroepitaxy on 3C-SiC(111) has not been so far demonstrated.

In this research, another method is proposed for obtaining the epitaxial diamond(111) films

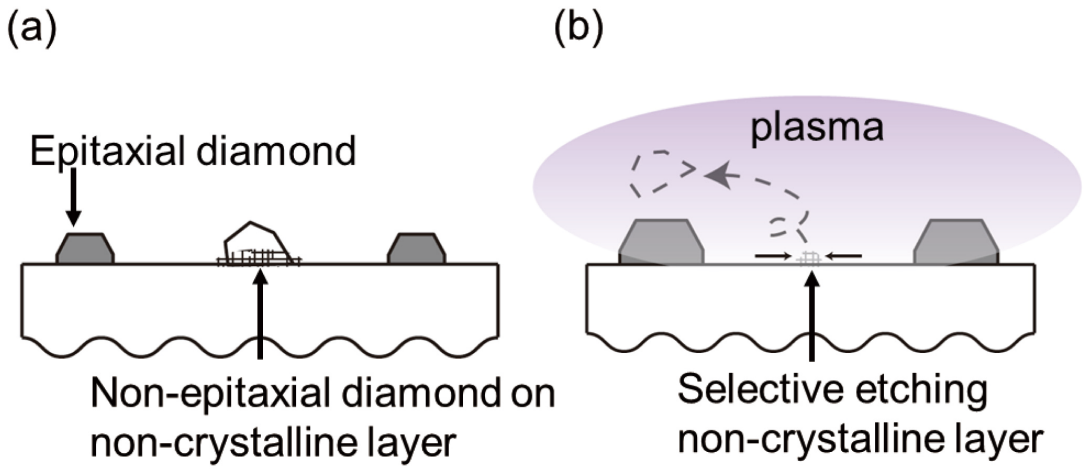

Figure 3.7: Schematic illustration of the proposed method for synthesizing a heteroepitaxial diamond(111) films on 3C-SiC(111). (a) Diamond on 3C-SiC after the BEN process. (b) Selective etching of the non-crystalline region and removal of non-epitaxial diamond.

on 3C-SiC(111)/Si(111) substrates. A key process in the proposed method is the selective oxidative etching of non-epitaxial diamond nuclei. In chapter 2, cross-sectional TEM observations of non-epitaxial diamond on the 3C-SiC(001) substrate revealed that a non-crystalline layer was formed at the interface between the non-aligned diamond and 3C-SiC. Diamond nuclei on Si substrates were similarly formed on *a*-C:H at the interface between diamond and Si during the BEN process. The presence of *a*-C interlayers, at the interface of the diamond nuclei and 3C-SiC, was also suggested from XPS studies. The addition of a small amount of oxygen gas preferentially etches away the non-crystalline layer (defective interface) [66], and the non-epitaxial nuclei are also spontaneously removed (Fig. 3.7). Consequently, epitaxial diamond grains become dominant on the 3C-SiC(111) surface. The initial diamond particle size is critical for this etching process; therefore, a rapid BEN technique called pulse-BEN was developed. In this section, the heteroepitaxial growth of diamond(111) on Si(111) substrates via 3C-SiC(111) will be described using the growth under oxygen enriched conditions.

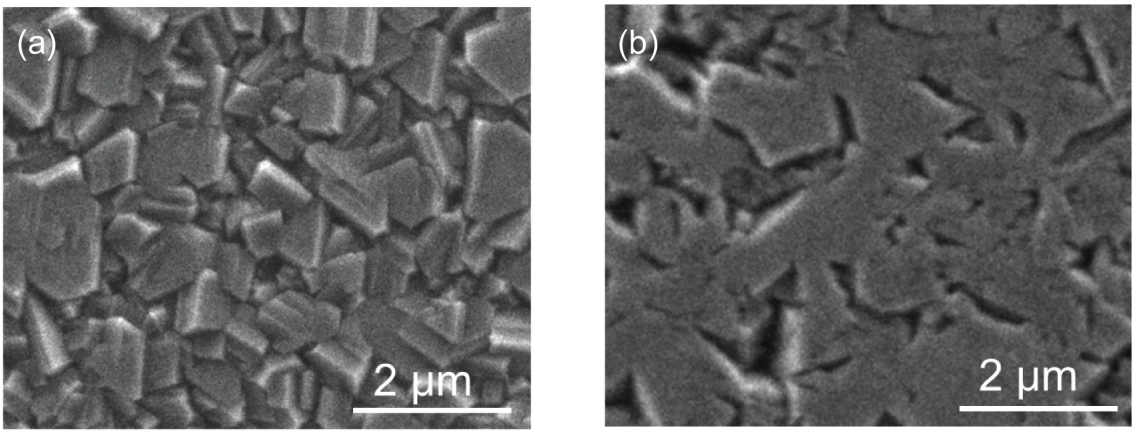

Figure 3.8: SEM images of diamond grains grown (a) without and (b) with oxygen.

3.2.1 Effect of oxygen gas addition for growth of diamond(111)

Figure 3.8a shows the diamond grains grown under conditions in a gaseous mixture of 2 % methane in hydrogen. The 3C-SiC(111) grown on Si(111) with an off angle of 2.5° toward $[\overline{1}\overline{1}2]$ was used as substrates. The diamond nucleation process was performed as mentioned in chapter 2. Although some of the diamond nuclei were epitaxially nucleated after the BEN procedure, the diamond became polycrystalline after the subsequent growth. It is because the non-epitaxial diamond grains on the non-crystalline regions exist on the 3C-SiC(111) surface. To remove the non-crystalline regions along with the non-epitaxial diamonds, 0.5 % oxygen was added to the gas mixture. The oxygen is known to be a highly effective etching gas for carbonaceous materials compared to hydrogen. Figure 3.8b shows the SEM image of diamond grains grown with the oxygen gas. The diamond grains showed triangular or hexagonal (111) facets. Thus, highly oriented (111) diamond was obtained by the oxygen addition to the growth environment.

3.2.2 Highly-oriented diamond(111) film on 3C-SiC(111)/Si(111)

Figure 3.9a shows an SEM image of a film formed in the presence of the oxygen gas for 3 hours, leading to a film thickness of 3 μm. The surface was perfectly covered by triangular (111) epitaxial grains and they merge with neighboring grains to form larger facets. The RHEED diffraction patterns (Fig. 3.9b, c) showed only diamond spots indicating that the 3C-SiC surface was perfectly covered by diamond. It was also found from the diffraction that the diamond grains were oriented in the (111) direction with the same azimuthal

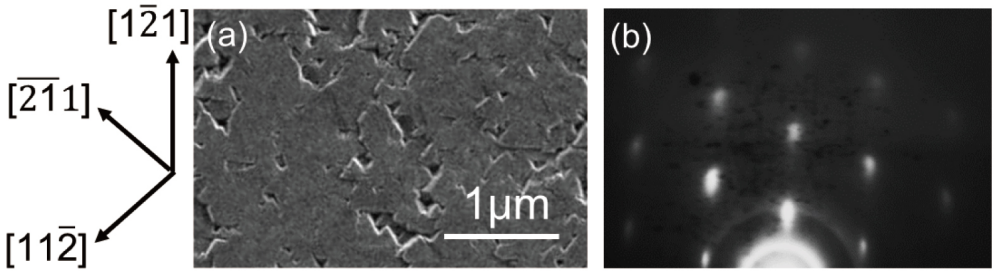

Figure 3.9: (a) SEM image and (b) RHEED pattern of the diamond(111) film grown with the oxygen gas for 3 h.

orientation. XRD measurements were performed to determine the crystal quality in more detail. A tilt spread of 2.4° was obtained from the FWHM of the (111) ω-rocking curve (Fig. 3.10a). The (11$\bar{1}$) ω-scan shows a FWHM of 4.0°, corresponding to an azimuthal angle spread (Fig. 3.10b). It is worth nothing that the intensities from twins are much smaller than those from the epitaxial grains in the 360° ϕ-scan (Fig. 3.10c). The twin formation is thought to be suppressed by the step-flow growth mode. Those values, i.e. the tilt spread of 2.4° and the intensity ratio of the epitaxial diamond and twins of 10, are much smaller than those of the diamond films grown directly on the Si substrates.

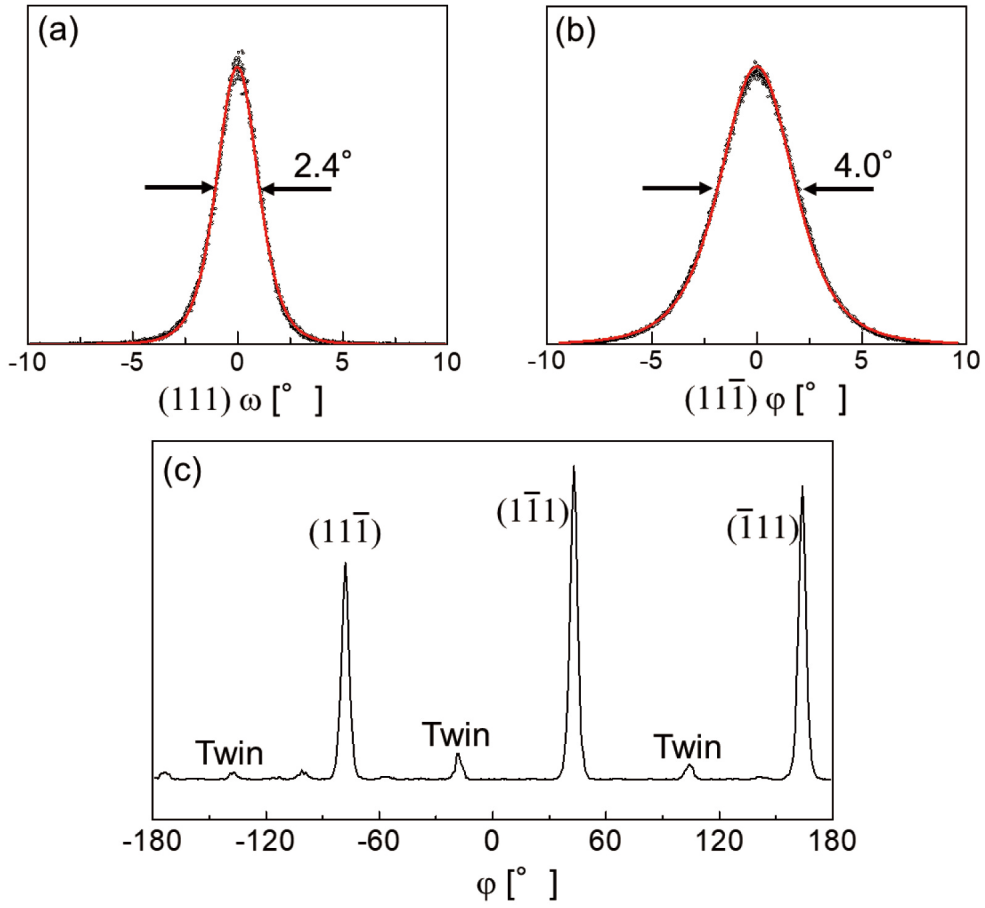

Figure 3.10: XRD measurements of the diamond(111) film. (a) Diamond (111) ω-rocking curve, (b) diamond (111) ϕ-rocking curve, and (c) diamond azimuthal scan (polar angle 54.7°).

3.3 Conclusion

We have performed the heteroepitaxial growth of diamond on 3C-SiC. The diamond(001) on 3C-SiC(001)/Si(001) was grown by two-step growth process. We have accomplished the tilt spread of 0.53° in diamond films thickness of 75 μm which is smaller than previously report. The residual stress and dislocation in heteroepitaxial diamond films decrease with increasing film thickness. The scaling laws of dislocation reduction obey the that of other semiconductor materials. Thus, the dislocation in the film reaches to 10^8 cm^{-2}. The highly-oriented diamond (111) films have been obtained using selectively oxygen etching growth. The oxygen in the growth gas can selectively etch the non-crystalline carbon at the interface. After growth for 3 hours, 3C-SiC(111) surface was perfectly covered with diamond(111) facets. The tilt spread of diamond (111) of 2.4° is much smaller than that of Si substrates directly and comparable for diamond(111) on Pt(111).

Chapter 4

POWER AND SENSOR DEVICES

4.1 SBDs on heteroepitaxial diamond(001)

The exceptional electric properties of diamond are promising material for next-generation power devices. Heteroepitaxial diamond film on 3C-SiC/Si substrate shown in Chapter 3 is promising materials for application of the diamond power devices. As for the first step, performance of the diamond power device is characterized by SBDs. In this section, we focus the boron-doped diamond films on 3C-SiC/Si(001) substrates.

4.1.1 Fabrication process of SBDs

Figure 4.1 shows the fabrication process of SBDs on heteroepitaxial diamond films. The on-axis 3C-SiC/Si(001) substrates were used as substrates. The nucleation process is same as mentioned in chapter 2. The thick intrinsic diamond layer of 100 μm was grown by using two-step process, including <001> preferential growth layer and <111> preferential growth layer. The nucleation and growth process are listed in Table A.5. The film thickness was estimated by growth rate of diamond. Boron-doped diamond film was synthesized by ASTEX type MPCVD with gas mixture of hydrogen, CH_4, oxygen, and $(CH_3)_3B$. In this process, oxygen gas was used for reducing incorporation of boron into diamond films. Ohmic contact electrodes of Ti/Pt/Au were formed on hydrogen terminated diamond surface. Schottky electrodes of Mo were formed on oxygen terminated diamond surface. In order to estimate the boron doping concentration and thickness of boron doped layers, the SIMS measurement was performed using single crystal diamond films grown

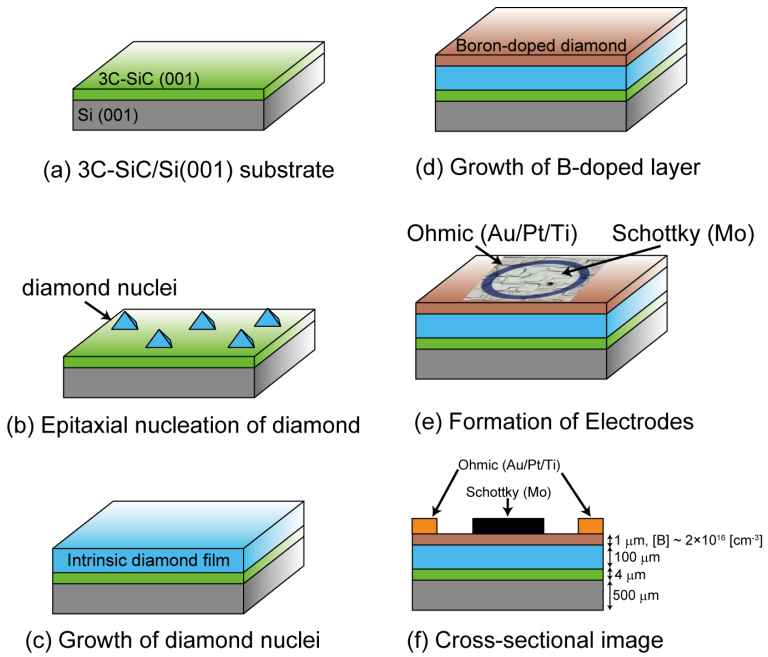

Figure 4.1: Schematic illustration of the fabrication process of SBDs on heteroepitaxial diamond(001) films.

on HPHT diamond (001) substrate (Fig. 4.2) under same growth condition. The boron concentration of diamond films were estimated 2×10^{16} cm^{-3} and thickness of 1 μm. Note that the high boron concentration on the order of 10^{18} cm^{-3} with thickness of 100 nm at interface, as shown in Fig. 4.2, was formed to prevent the spread of depletion layer to intrinsic diamond layer. Importantly, other impurities of hydrogen, oxygen, and Si reached to detection limits of SIMS.

4.1.2 Electrical characteristics of SBDs on heteroepitaxial diamond on 3C-SiC

Figure 4.3 shows the $C^2 - V$ characteristic at 100 kHz. Under this high frequency, most of the interface trapped charier cannot follow. Therefore, boron concentration of heteroepitaxial diamond films is obtained by

$$\frac{1}{C^2} = \frac{2(V_0 - V)}{q\epsilon_0\epsilon_r N_A S^2} \tag{4.1}$$

where S is surface area. Thus, we obtained the boron concentration of 9×10^{15} cm^{-3},

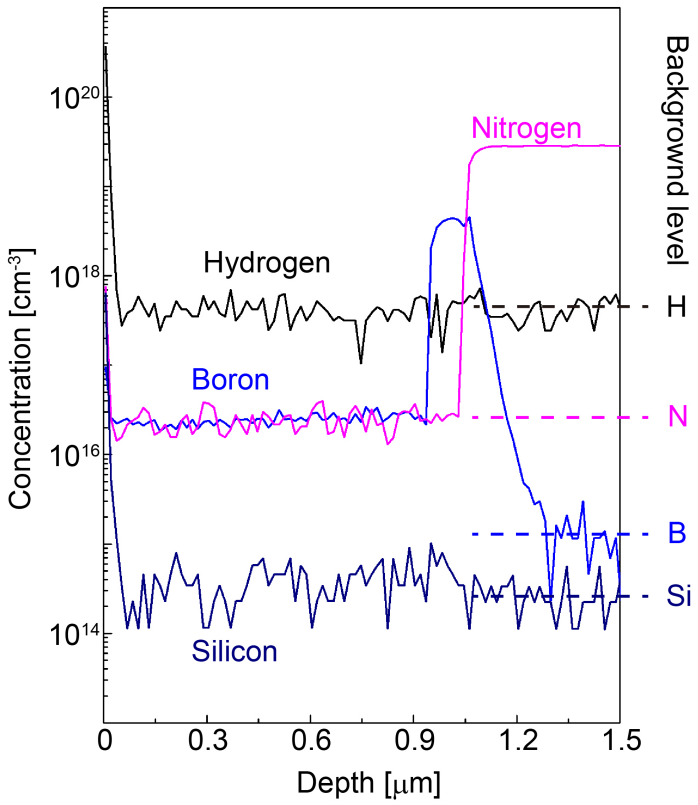

Figure 4.2: SIMS measurement of homoepitaxial diamond films.

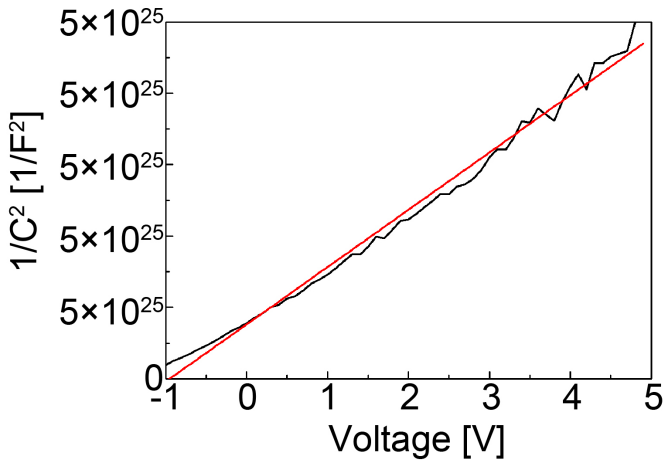

Figure 4.3: $C^2 - V$ characteristic of the heteroepitaxial diamond at 100 kHz.

which is almost same as doping concentration of single crystal diamond as shown in Fig. 4.2. Figure 4.4 shows the typical current density-voltage (j-V) characteristic of SBDs on heteroepitaxial diamond films measured at room temperature. The high rectification of 10^8 is observed at ±5 V. The specific on-resistance of 0.2 $\Omega - cm^2$ is obtained which is comparable for SBDs on homoepitaxial diamond film of 0.3 $\Omega - cm^2$[88]. The forward current density of SBDs is described by

$$j = j_s exp(\frac{qV}{nkT})(1 - exp(\frac{qV}{kT})) \tag{4.2}$$

Then, j_s is defined as

$$j_s = A^* T^2 exp(-\frac{q\phi_{bi}}{kT}) \tag{4.3}$$

where j_s, n, k, A^*, ϕ_{bi}, and T are the saturation current density, ideality factor, Boltzmann constant, Richardson constant, Shottky barrier height, and temperature, respectively. The best fit result using equation 4.2 and 4.3 is shown in Fig. 4.4 as red line. The ideality factor (n) of 1.8 and Shottky barrier height (ϕ_{bi}) of 1.1 eV were obtained. The high rectification of 10^7 is observed in the temperature range from RT to 500 K (Fig. 4.5a). Importantly, the ideality factor decreases with increasing the temperature (Fig. 4.5b). Conversely, the apparent barrier height tends to increase to 1.5 eV as the temperature rises. This behavior is considered as a transition of the interface current transport from thermionic field emission to thermionic emission. At the low temperature, the carrier tunneling probability through the Schottky barrier is higher than that at high temperature. Therefore, the ideality factor

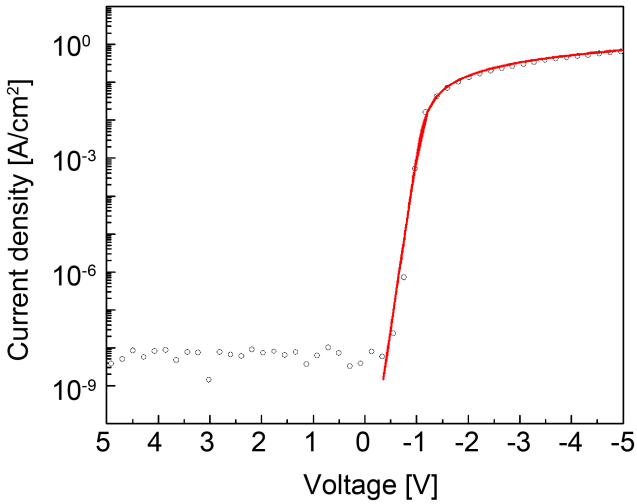

Figure 4.4: j-V characteristic of SBDs on heteroepitaxial diamond at room temperature. Circles and red line indicate the experimental result and best fit curve using equation 4.2 and 4.3, respectively.

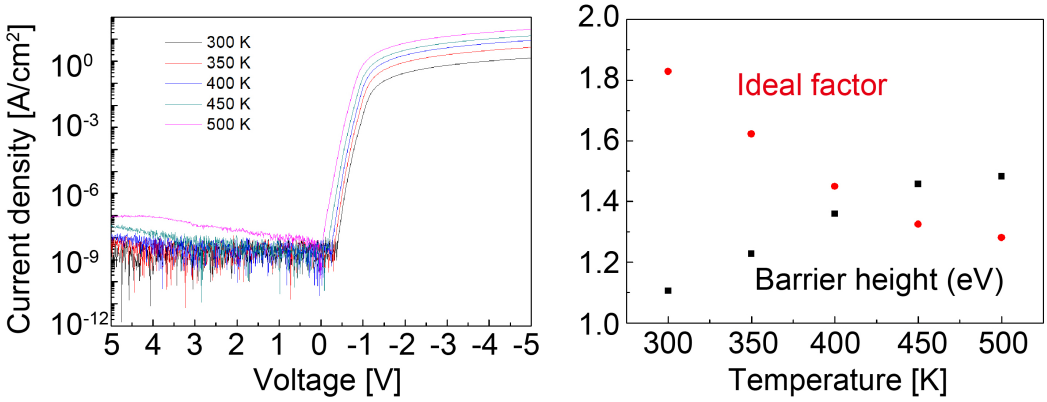

Figure 4.5: j-V characteristic of SBDs on heteroepitaxial diamond at high temperature.

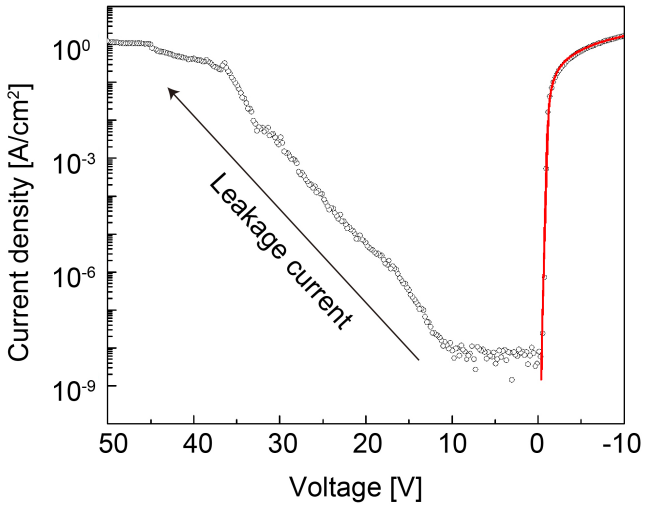

Figure 4.6: j-V characteristic of SBDs on heteroepitaxial diamond at RT with voltage ranges from 50 to -10 V.

is decrease to 1.2 at 500 K.

The SBDs on heteroepitaxial diamond films show the good electric characteristics under temperature range from 300 to 500 K and voltage range of ±5 V as shown in Fig. 4.5. The remaining issue of the SBDs of the heteroepitaxial diamond is the leakage current at the high reverse bias voltage. The leakage current is rapidly increased with increasing the reverse bias voltage, as shown in Fig. 4.6. One of possible cause is dislocation in the heteroepitaxial diamond films. In chapter 3, we have estimated the dislocation density by H_2/O_2 plasma treatment (Fig. 3.5), and the dislocation density decrease scaling laws of equation 3.9. Therefore, the leakage current should be decrease with increasing the thickness of heteroepitaxial diamond film. However, the dislocation reduction by increasing film thickness is required very long time. Further improvement of the heleroepotaxial growth and device technology are necessary to suppress the leakage current.

Therefore, the new technology for reduction of dislocation is required. Figure 4.7a shows the heteroepitaxial diamond films in thickness of 15 μm grown under same growth condition. We performed H_2/O_2 plasma treatment for formation of etch-pit at the surface, corresponding to dislocations at the diamond surface. Figure 4.7b,c show the SEM images after H_2/O_2 plasma treatment for 1 hour. The two (large- and small-) size etch-

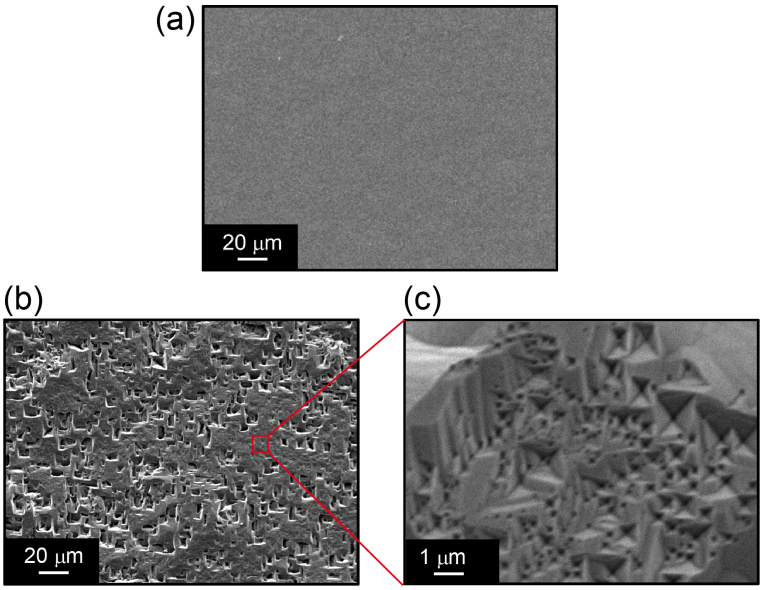

Figure 4.7: SEM images of (a) as-grown surface and (b) after H_2/O_2 plasma treatment of diamond films with thickness of 15 μm. (c) magnified SEM image of marked area of (b).

pits were observed after H_2/O_2 plasma treatment. It has been reported that the leakage current is proportional to the number of large etch-pits[88], and it is considered that the leakage current is increased by this large etch pit. It have been revealed that the dislocation in diamond can be decreased by hole. It was accomplished following ways[89]: (i) Formation of hole in the diamond substrates (Fig. 4.8a); (ii) Diamond substrates laterally grown by CVD (Fig. 4.8b); (iii) merge the lateral growth front (Fig. 4.8c). In the case of heteroepitaxial diamond films, the large etch pits are formed at the 45° mixed dislocation[83], which is considered that main component of increasing the leakage current. Therefore, after the formation of large etch pits by H_2/O_2 plasma treatment, the heteroepitaxial diamond films laterally grown by CVD. Using this process, the 45° mixed dislocation can be selectively reduced.

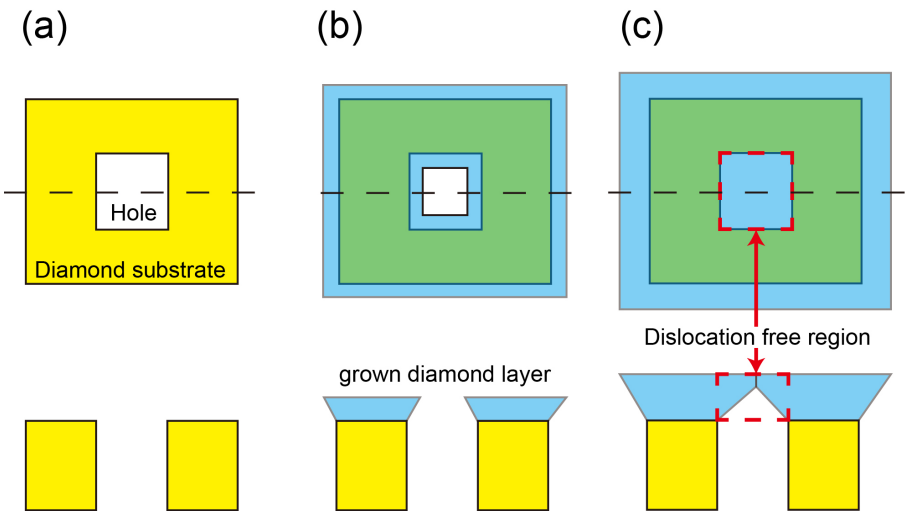

Figure 4.8: Top (upper) and cross-sectional (bottom) images of reduction of dislocation by hole. (a) Before growth, (b) during the lateral growth, and (c) after merging the grown films[89].

4.2 NV centers in heteroepitaxial diamond(111)

The diamond sensors using NV centers have been predominately demonstrated by using single-crystal diamond substrates. Heteroepitaxial diamond films on Si substrates is expected to enable on-chip integration with well-established Si CMOS technology. Another advantage of heteroepitaxial thin films is the fabrication of photonic structures, as demonstrated for NV and SiV centers [25, 90]. Very bright single photon emission was also reported from a SiV center in nanodiamond formed on the Ir surface. Regarding the NV sensor devices, control of the alignment of the N-V axis is crucial to achieve high-sensitivity. Perfect alignment of ensemble NV centers to one atomic direction can maximize the contrast of ODMR [21, 22, 22, 91]. The alignment of NV centers towards one direction have been demonstrated in diamond(111) single-crystal substrates via CVD growth. However, there have been no reports on the formation of aligned NV centers in heteroepitaxial diamond films. In this section, we will describe the formation of aligned NV centers in heteroepitaxial diamond(111) films on the 3C-SiC/Si substrates. The issues of the growth on the Si substrates, SiV centers are easily formed in heteroepitaxial diamond films. The SiV centers lead to deterioration of contrast of ODMR because their ZPL of 738 nm is located within the phonon sideband of NV centers (637-800 nm). Oxygen gas addition during CVD growth is known to improve diamond crystal quality and inhibit the incorporation of Si impurities [92]. Thus, here, we demonstrate the formation of the [111] aligned NV centers while suppressing the incorporation of the Si impurities into diamond films by using oxygen gas.

4.2.1 Fabrication process of NV centers in heteroepitaxial diamond

Figure 4.9 shows the experimental procedure of the formation of NV centers in heteroepitaxial diamond films on the 3C-SiC/Si(111) substrates. First, heteroepitaxial diamonds were nucleated by MPCVD using the BEN procedure (Fig. 4.9a,b). The BEN process was performed at a voltage of -150 V in a gas mixture of 20 % CH_4 in H_2. At the first, we incorporated NV centers directly on the diamond particles to investigate the effect of oxygen gas on the SiV formation (Fig. 4.9c). As the second experiment, non-doped (intrinsic) diamond(111) films were fabricated without nitrogen gas (Fig. 4.9d). Then, the subsequent growth was performed under the conditions for the NV center formation optimized by using the diamond particles (Fig. 4.9e). The fabricated NV centers in the

diamond particles and films were characterized using confocal fluorescence microscope with an excitation laser (wavelength: 532 nm) and a detector of an avalanche photo diode. The measurements were performed with an air objective (numerical aperture: 0.95) at room temperature.

4.2.2 NV centers in diamond particles

Figure 4.10a shows the PL spectra of heteroepitaxial diamond particles grown under different oxygen concentrations (0.1 %, 0.3 % and 0.5 % in the H_2 gas). The strong ZPL of the SiV center appears at 738 nm with 0.1 % oxygen. The increase in the oxygen concentration effectively reduces the SiV fluorescence. The 0.5 % sample clearly shows the ZPL of the NV center, and the intensity of the SiV center is much lower than that of 0.1 % conditions. Figure 4.10b shows the evolution of the peak intensity of the SiV center plotted versus the oxygen concentration in the gas phase. The emission intensity of the SiV color center was monotonically reduced with respect to the oxygen concentration. At oxygen concentrations of over 0.6 %, diamond particles were not observed on the 3C-SiC at all because the high oxygen concentration gives rise to a high etching rate of the diamond compared with the growth rate [93]. Thus, we defined the oxygen concentration of 0.5 % is suitable for the formation of NV centers while suppressing SiV centers. The reason for the reduction of the SiV intensity by oxygen is considered to be the formation of silicon oxide in the gas phase, which prevents the Si atoms from being incorporated in diamond. In fact, it has been reported that the concentration of Si impurities in an epitaxial grown diamond film decreased with increasing the oxygen concentration [92].

A confocal fluorescence microscope image of diamond particles including NV centers is shown in Fig. 4.11a. A typical triangle (111) facet is seen in the inset of Fig. 4.11a, which indicates that the diamond particle was epitaxially nucleated on the 3C-SiC surface. The density and size of the diamond particles were approximately 10^8 cm^{-2} and $0.5 - 2$ μm, respectively. Importantly, decreasing of an order of 10^4 of SiV centers into diamond was obtained by oxygen addition Fig. 4.10b. However, the NV center density of an order of 10^{15} was estimated from photon count rate, which is only one digit lower than that of single crystal diamond formed by CVD without oxygen condition [21]. The reason for effectively reduction of SiV centers is considered as oxide species are more difficult to incorporate into diamond films than the non-oxide species on the growing diamond surface. In fact, it was reported that the concentration of oxygen in epitaxial grown diamond film is less than

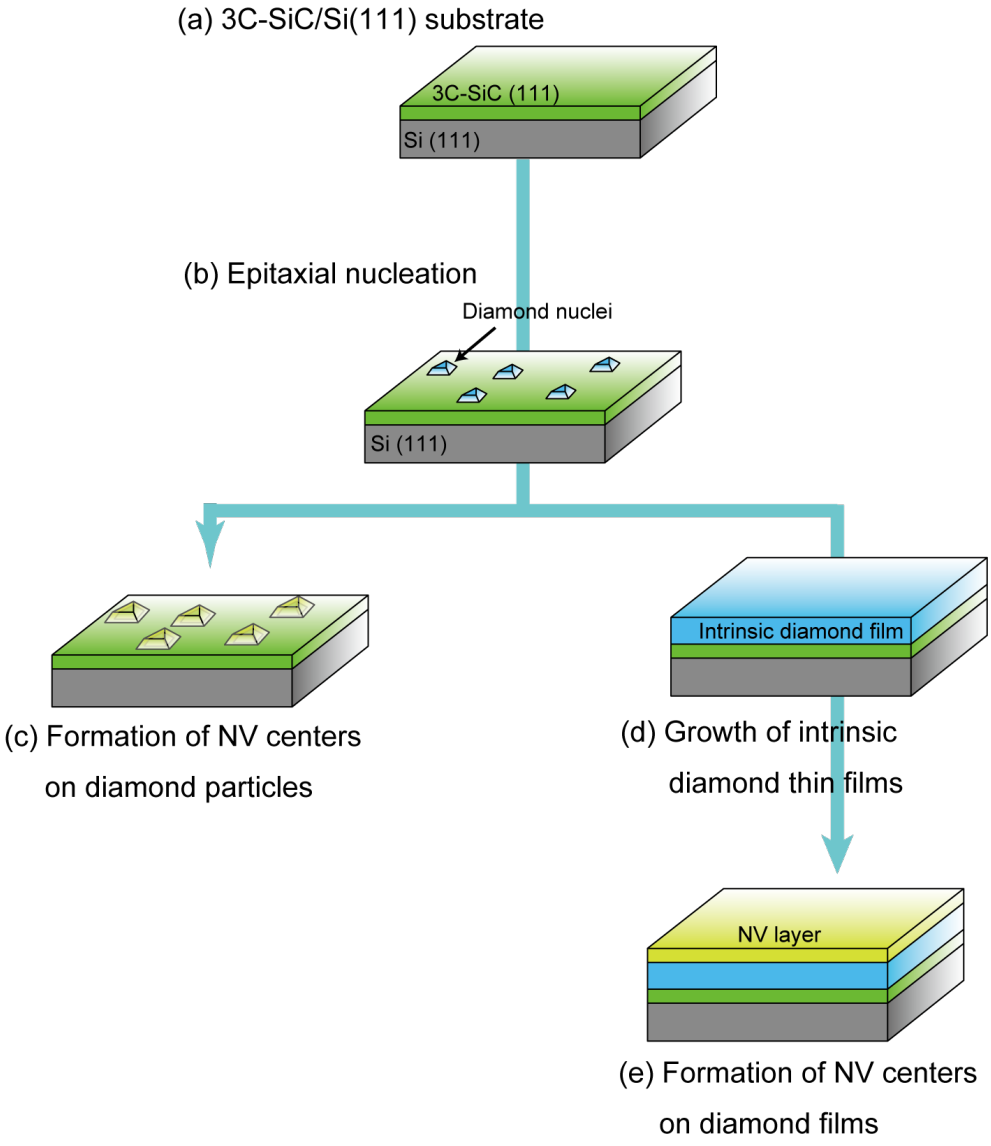

Figure 4.9: Schematic illustration of the formation procedure of NV centers on heteroepitaxial diamond(111) particles and films.

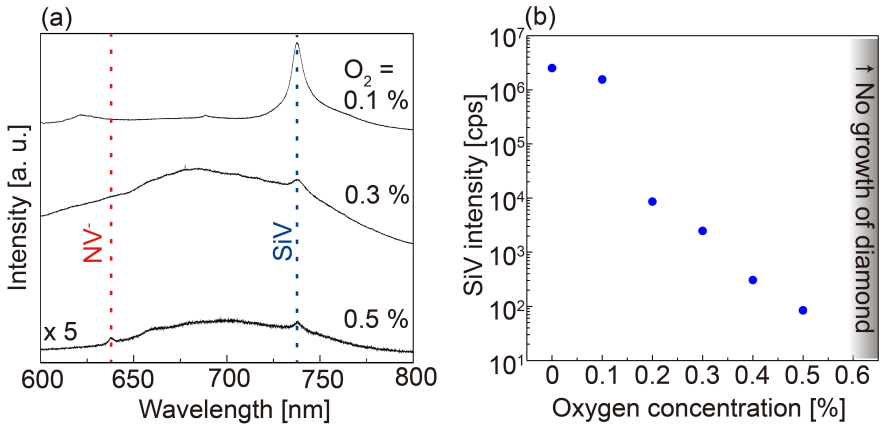

Figure 4.10: (a) PL spectra of diamond particles. The particles were formed by the 10 seconds BEN process and subsequent growth for 30 minutes under an oxygen concentration of 0.1 %, 0.3 % and 0.5 %. (b) Evolution of the peak intensity of SiV centers with respect to the oxygen concentration in the H_2 gas.

the detection limit of SIMS even the oxygen exists in the gas phase [92]. Considering the reaction of oxygen with Si and nitrogen, these are written as follows:

$$Si + O_2 \rightarrow SiO + O \tag{4.4}$$

$$N + O_2 \rightarrow NO + O \tag{4.5}$$

Then, the chemical reaction rate (v) in the plasma is described by

$$v = k[A][B] \tag{4.6}$$

where k is rate coefficient and [A] and [B] are concentrations of A and B, respectively. The rate coefficients of these pathways are $k_{Si} = 2.7 \times 10^{-10}$ [94] and $k_N = 4.4 \times 10^{-12} e^{\frac{-3220}{T}}$ [95]. Considering the growth temperature (T) of around 1400 K, the reaction rate relationship of Si > N is calculated. Thus, Si was strongly suppressed by oxygen introduction. ODMR measurements were performed with a static magnetic field applied along the [111] direction to investigate the atomic orientation of the NV centers in the heteroepitaxial diamond particle (Fig. 4.11b). It is possible to distinguish between the [111] orientation and the orientation of the rest of the NV centers (i.e. $[1\bar{1}\bar{1}]$, $[\bar{1}1\bar{1}]$ and $[\bar{1}\bar{1}1]$). Figure 4.11b

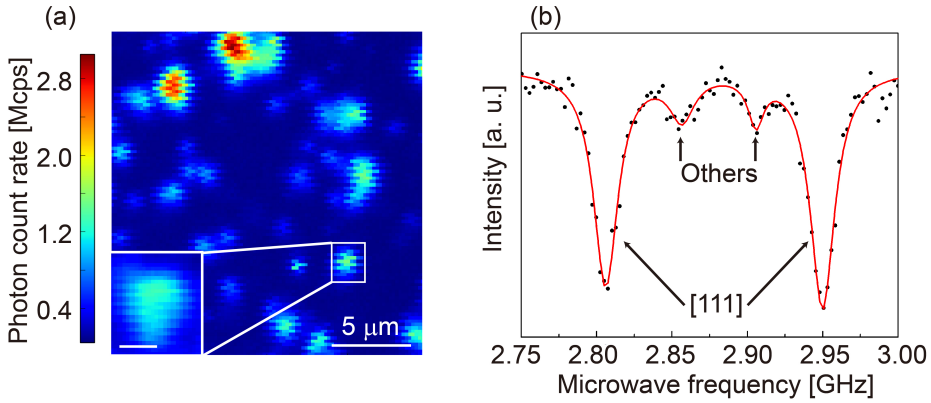

Figure 4.11: (a) Confocal fluorescence microscope image of diamond particles on a 3C-SiC/Si substrate grown for 30 minutes under an oxygen concentration of 0.5 %. An inset shows a magnified epitaxial diamond particle, and scale bar is 500 nm. (b) ODMR spectrum of the epitaxial diamond particle. A magnetic field was applied along the [111] direction.

shows an ODMR spectrum from an epitaxial diamond particle. The peaks at the lowest and highest frequencies correspond to the NV centers aligned to the [111] direction, while the inner peaks come from the other three directions. The alignment ratio is obtained from[96]

$$\eta = \frac{S_{111}}{S_{111} + 1.4S_{others}} \tag{4.7}$$

where S_{111} and S_{others} are intensity of ODMR spectrums of [111] direction and other direction, respectively. By comparing the peak intensities, the alignment ratio to the [111] direction was estimated to be 89 %, indicating that the NV centers can be preferentially aligned on the (111) surface of the epitaxial diamond particle. This alignment of NV centers in small diamond particles would be useful for high sensitivity temperature sensors[97].

4.2.3 NV centers in heteroepitaxial diamond films

We then formed the heteroepitaxial diamond(111) thin films and incorporate NV centers on top. After the formation of an intrinsic diamond film, NV centers were incorporated under the same conditions as the growth of the diamond particles above (i.e. oxygen concentration of 0.5 %). Figure 4.12 shows the crystal orientation distribution and {001}

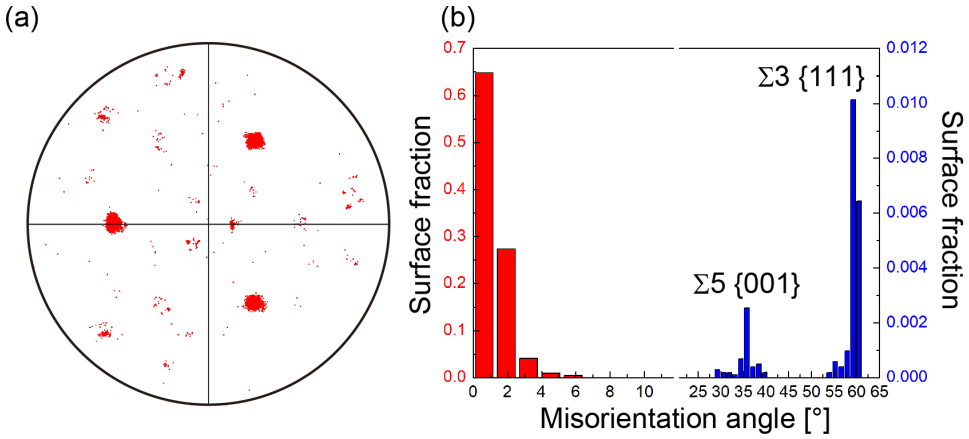

Figure 4.12: EBSD analysis of heteroepitaxial diamond films. (a) (001) pole figure of heteroepitaxial diamond(111) films. (b) The surface fraction of heteroepitaxial diamond(111) films with respect to the misorientation angle from [111] direction.

pole figure of heteroepitaxial diamond films after incorporating NV centers, measured by EBSD, which were acquired using area of 50×50 μm^2 with step size of 200 nm. The three-fold symmetry pattern indicating the epitaxial diamond particles was observed from {001} pole figure of (111) diamond. Although the diamond films include Σ3{111} twins (misorientation angle of around 60°) [98] and Σ5{001} twist (misorientation angle of around 35°)[99] components, most of diamond surface was epitaxially oriented. These grain boundaries (Σ3 and Σ5) are often observed in homoepitaxial diamond (111). Figure 4.13a and b show a SEM and confocal images of the fabricated heteroepitaxial and homoepitaxial diamond film grown under same growth condition, respectively. Considering the growth rate in heteroepitaxial films, the thickness of the intrinsic and NV layers was estimated to be 10 and 1.5 μm, respectively. The NV center density in both the heteroepitaxial and homoepitaxial diamond films were estimated to be on the order of 10^{15} cm^{-3}. which was obtained with comparison to a photon count rate of a single NV center. Although the diamond grains are not perfectly coalesced because of a tilt spread of around 2° (i. e. low angle grain boundary), the surface is covered by triangle and hexagonal grains which are typical (111) facets. The grains show higher fluorescence intensities than that at the grain boundary. We found that a high amount of amorphous carbon was formed at the grain boundaries, which would inhibit the formation of high-quality diamonds with NV centers. We evaluated the alignment of the NV axis using equation 4.7 in both the

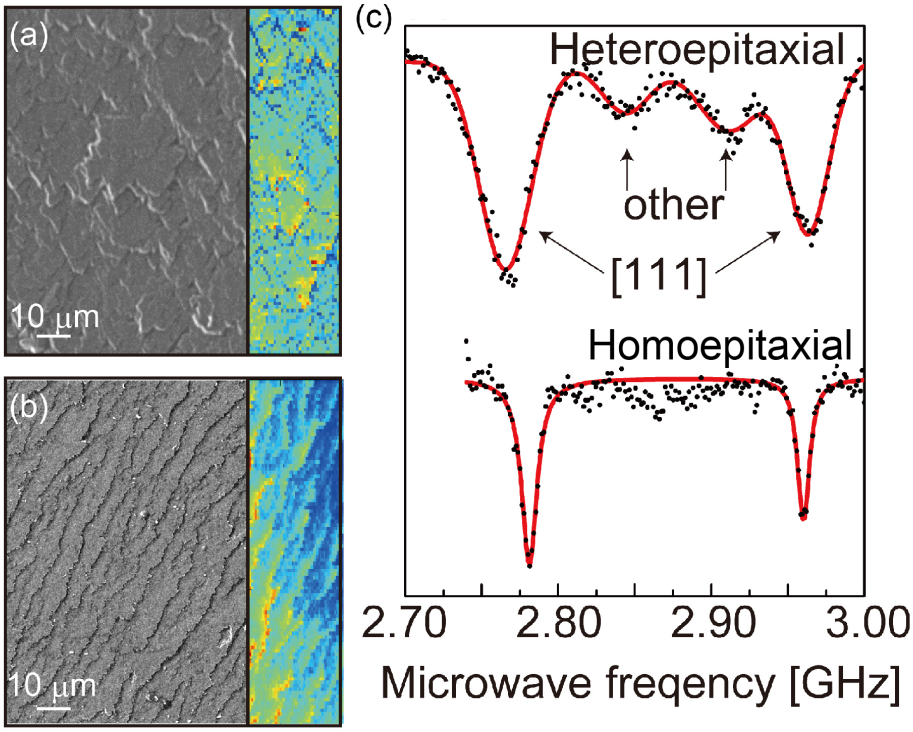

Figure 4.13: SEM and confocal images of (a) heteroepitaxial and (b) homoepitaxial diamond films grown under same growth condition. (c) Typical ODMR spectrums of heteroepitaxial (upper) and homoepitaxial (bottom) films.

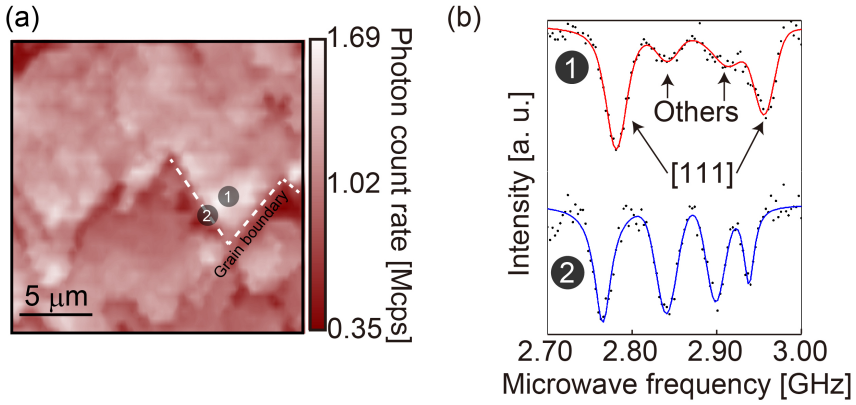

Figure 4.14: (a) confocal fluorescence microscope image of a heteroepitaxial diamond film. (b) ODMR spectrum at the heteroepitaxial grain and grain boundary, marked in panel (b).

heteroepitaxial and homoepitaxial diamond films by ODMR measurements (Fig. 4.13c). We obtained the alignment ratio of 66 % on average from the heteroepitaxial diamond films, which indicates the NV centers in heteroepitaxial were preferentially aligned toward [111] direction. However, the NV centers in homoepitaxial diamond films were perfectly aligned toward [111] direction (i. e. the alignment ratio of 100 %). We considered that the difference of alignment ratio between heteroepitaxial and homoetpitaxial diamond films caused by difference of growth mode. In the case of homoepitaxial diamond films, the step-flow growth mode promotes the formation of alignment NV centers. In fact, the surface structure of homotepitaxial diamond films shows step-terrace structure. In contrast, the heteroepitaxial diamond films shows the grain boundaries caused by tilt angular spreads estimated form EBSD. If the grain boundaries are clearly observed, it propagates to growth direction instead of step-flow growth[100]. The measurements were performed at the diamond grain and the grain boundary as shown in Fig. 4.14. The signals from the [111] aligned NV centers at the grain are 4.7 times stronger than that from the orientation of the rest of the NV centers, indicating the preferential alignment of the NV centers. The alignment ratio to the [111] direction ranges from 60 to 90 % with the average value of 70 %. In contrast, the grain boundary shows more random orientations, giving rise to the

average ratio of 50 %. Therefore, in the case at the grain boundaries, it is thought that the grain edges inhibits the step-flow growth, which leads to the formation of the NV centers with more random orientations. It is expected that a flat and continuous heteroepitaxial (111) diamond film without grain boundaries makes it possible to fabricate the sensor platform of the perfectly-aligned NV quantum sensors. It is worth noting that, at the grain boundary, the center position between the two ODMR dips from the [111]-aligned NV centers shifted by -10 MHz with respect to that at the grain. This means that a tensile stress of 1 GPa with uniaxial direction was generated for the NVs at the grain boundary[101, 102]. The larger strain at the grain boundary has been also observed in a polycrystalline diamond using NV centers[103]. Finally, the spin coherence time (T_2) of the NV centers on the heteroepitaxial diamond film was evaluated by a Hahn-echo sequence. For comparison, NV centers on a single-crystal (111) diamond substrate was characterized. We obtained a spin coherence time of 6.0 μs on the heteroepitaxial film, which was comparable to that on the single-crystal diamond (6.2 μs), as shown in Fig. 4.15. Both the spin coherence times are thought to be limited by substitutional nitrogen atoms (called P1 center)[104]. This indicates that other paramagnetic impurities and defects in the heteroepitaxial diamond film is suppressed to the level in the homoepitaxial film.

4.2.4 Magnetic sensitivity of NV center in heteroepitaxial diamond film

Although the NV centers in heteroepitaxial diamond films were preferentially aligned toward [111] direction, the alignment ratio is lower than that of single crystal diamond. In addition to alignment ratio, FWHM of ODMR is much wider than that of single crystal diamond. In order to obtain higher sensitivity, improving both alignment ratio and FWHM of ODMR are required. This is because that the alignment ratio and FWHM are corresponded to contrast of ODMR and dephasing time (T_2^*), respectively. We assumed that the difference between heteroepitaxial and single crystal diamond is caused by grain boundaries at the film surface and/or residual stress in the films. As mentioned above, the growth mode at the grain boundaries are little different with diamond grain due to the propagation of grain boundaries. The residual strain in the film is also caused by grain boundaries because the low angle grain boundaries form the dislocation and/or disclination. If the residual stress in the diamond films are caused by CTE difference between diamond and Si, the stress in the diamond films is only compressive stress of 0.5

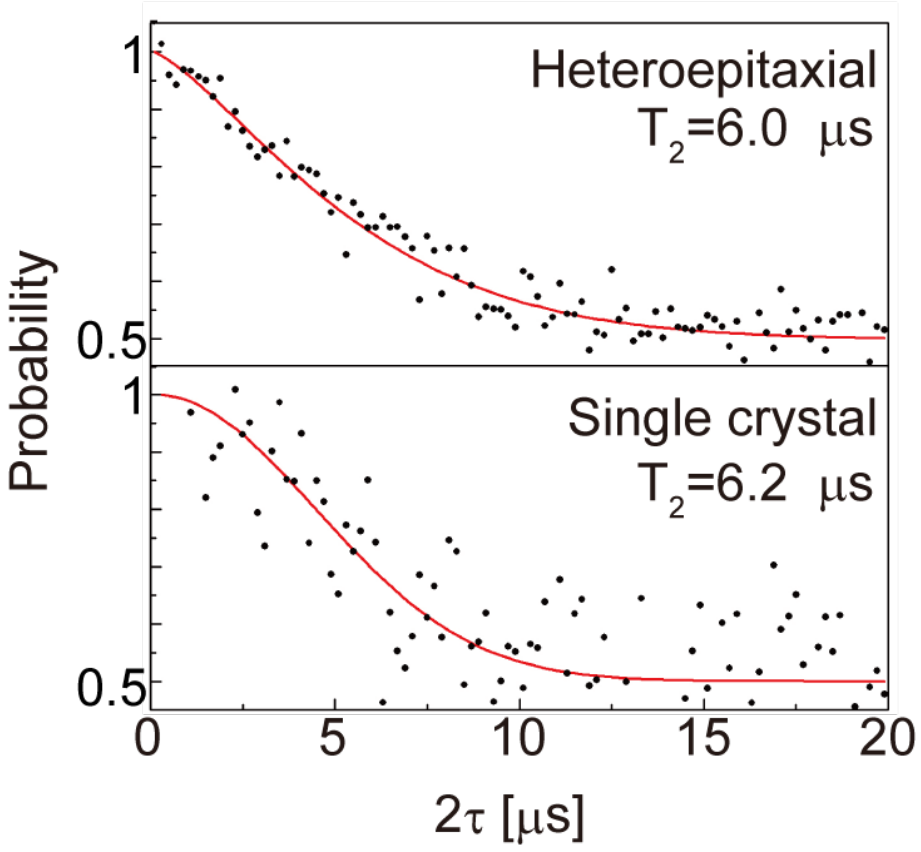

Figure 4.15: Spin coherence time of NV centers on the heteroepitaxial diamond film (upper curve). For comparison, spin coherence time of NV centers formed on a single crystal diamond is shown (bottom).

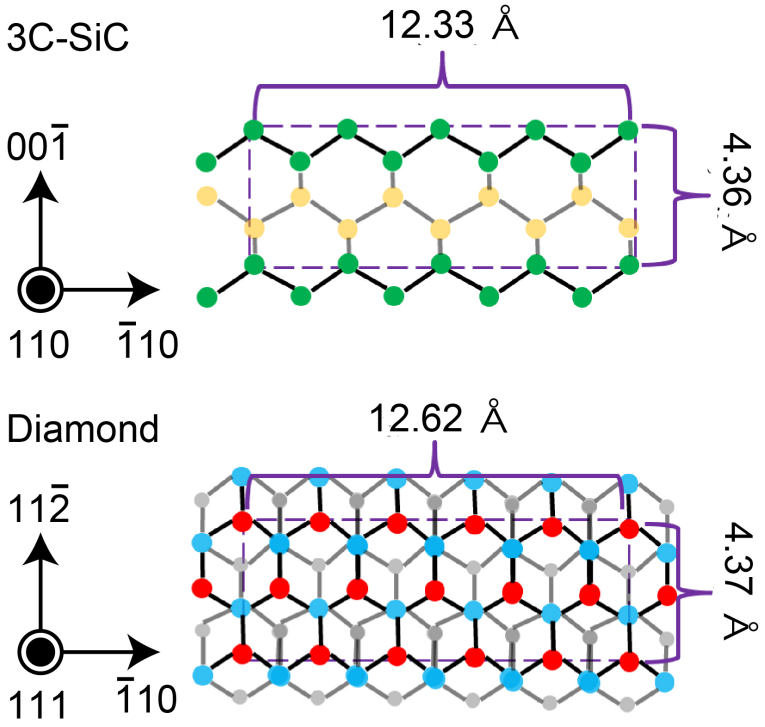

Figure 4.16: Schematic illustrates of crystal structure of 3C-SiC(110) and diamond(111).

GPa. However, the stress in heteroepitaxial diamond films existed both of compressive and tensile stress of above 1 GPa which is estimated from shift of zero-field splitting parameter of 2.87 GHz. Therefore, the stress in the diamond films is considered to induce the deterioration of alignment of the NV centers. For these reasons, perfectly coalesced diamond films (i. e. without grain boundaries films) lead to improve the alignment ratio of NV centers and FWHM of ODMR. The grain boundaries are caused by the tilt spread of diamond grains. One way to reduce the tilt spread of diamond(111) grains is to reduce the lattice mismatch. The lattice mismatch with diamond of 3C-SiC(111) is 18 %. Considering the 3C-SiC(110) surface, the lattice mismatch with diamond(111) can be decrease (Fig. 4.16). Heteroepitaxial growth of 3C-SiC(110) have been reported on Si(111) substrates and this system may reduce the lattice constant mismatch between 3C-SiC and Si, and then improve the crystal quality of 3C-SiC(111)[105, 106]. Thus,

the diamond(111) on 3C-SiC(110) would be improve the crystal quality of heteroepitaxial diamond(111) films.

We calculate the sensitivity of NV centers in heteroepitaxial diamond films using equation 4.8. The magnetic sensitivity is described by

$$\eta = \frac{h}{2\pi g \mu_b C \sqrt{\eta N T_2^*}} \tag{4.8}$$

where h is Plank constant, g is g-factor, μ_b is Bohr magneton, N is the number of NV center, C is contrast of ODMR, and T_2^* is dephasing time. Figure 4.17 shows the calculated sensitivity of NV centers with thickness of 1.5 μm in heteroepitaxial diamond films. The magnetic sensitivity is calculated as several nT/$\sqrt{\text{Hz}}$ to several hundred pT/$\sqrt{\text{Hz}}$ using equation 4.8. However, it is necessary to further increase the sensitivity in order to use as magnetocardiogram or magnetoencephalography. If a perfectly aligned stress-free film can be realized using the above method (i. e. heteroepitaxial growth of diamond (111) on lattice matching 3C-SiC (110)), the sensitivity will be comparable to NV centers in homoepitaxial diamond films. Furthermore, since the film thickness of the NV center fabricated this time is as thin as 1.5 μm, if it can be increased to a thickness equivalent to that of the (001) film, application as a magnetoencephalography can be expected.

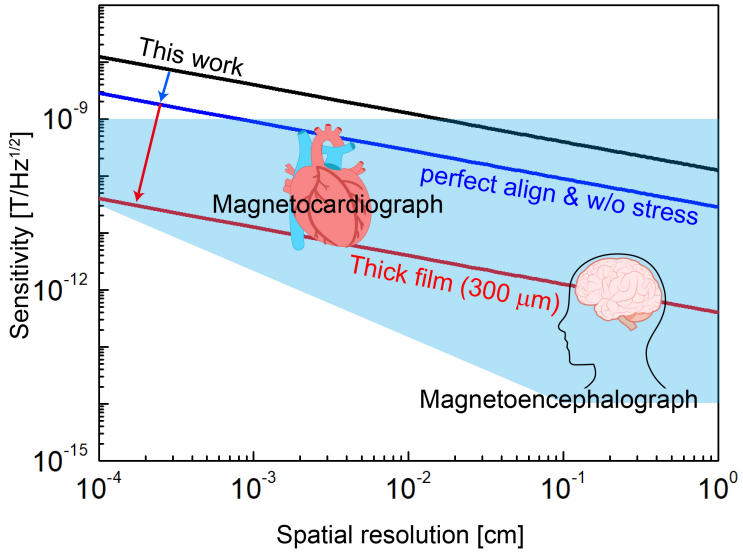

Figure 4.17: Sensitivity of NV centers calculated by equation 4.8. Black, blue, and red lines donate the NV centers of this work, perfectly aligned NV centers in stress-free films, and NV centers with thickness of 300 μm, respectively.

4.3 Conclusion

Using the heteroepitaxial diamond (001) and (111), we have demonstrated power devices as SBDs and magnetic sensors, respectively. The diamond SBDs showed a high rectification of 10^8 at ±5 V. The specific on-resistance (0.2 $\Omega - cm^2$) is comparable with SBDs using single-crystal diamond films. However, the leakage current at higher voltage (>10 V) was increased, due to the high dislocation density in the heteroepitaxial diamond films. Further improvements in the heteroepitaxial growth and device technology are necessary to suppress the leakage current. The sensor devices using NV centers in diamond were formed in both the heteroepitaxial diamond (111) particles and films. The NV centers in heteroepitaxial diamond could be preferentially aligned in the one-atomic direction, leading to improved sensitivity as confirmed in experiments. However, the calculated sensitivity was still lower than that of homoepitaxial films, so the crystal quality of heteroepitaxial diamond (111) films should be further improved. These developments in heteroepitaxial diamond films could be used as a diamond device platform.

Chapter 5

SUMMARY

5.1 Thesis summary

In this thesis, we have performed heteroepitaxial growth of diamond on a Si substrate via 3C-SiC intermediate layer to synthesize large-area and low-cost diamond film for both next generation power devices and high sensitivity sensor devices.

In Chapter 2, we have developed the improving and optimizing of epitaxial diamond nucleation on 3C-SiC during the BEN process by using the combination of high-density plasma and in-situ monitoring of the nucleation process. At the initial stage of the BEN process, non-epitaxial diamond nanoparticles synthesized though the non-crystalline carbon species. However, the non-crystalline impurities are selectively etched by atomic hydrogens which are effectively generated by the unique system of AE-MPCVD. Moreover, the optimization of the BEN process. Moreover, optimization of the BEN duration was performed by the in-situ monitoring of the bias current. The bias current variation is caused by increasing diamond surface coverage. The bias current variation was good agreement with KJMA theory. Using the KJMA theory, the diamond nucleation process can be estimated from the Avrami exponent. In the case of 3C-SiC, the Avrami exponent of 4 was obtained the increasing bias current of 10 % from minimum, which indicates that the nucleation process of diamond is saturated. This characteristics were observed form both of 3C-SiC (001) and (111). Therefore, this technique is useful for each crystal orientations.

In Chapter 3, we have investigated the crystal orientation and dislocation reduction of heteroepitaxial diamond(001) films and developed selectively growth method of epitax-

ial diamond(111) films. The diamond(001) films of which nucleated by combination of high-plasma density and optimized by the in-situ monitoring of the bias current shows the smallest tilt value of 0.52°, compared with previously reported heteroepitaxial diamond films on 3C-SiC. The dislocation and residual stress in the diamond films are decreased with increasing films thickness. This suggests that the dislocation in the heteroepitaxial diamond(001) films can be improved by increasing the films thickness. We have achieved the dislocation density of an order of 10^8 cm^{-2} ,which is comparable for natural single crystal diamond. The diamond(111) films have been reported first time. This is enabled by the combination of nucleation process as mentioned in chapter 2 and selectively etching process of non-epitaxial nanoparticles by oxygen. The tilt spread of diamond(111) on 3C-SiC is wider than that of (001), however, it is much smaller than highly-oriented diamond(111) films on Si substrates directly and comparable that on Pt(111).

In Chapter 4, we have demonstrated power devices as SBDs and magnetic sensor by using heteroepitaxial diamond (001) and (111), respectively. The diamond SBDs shown high rectification of 10^8 at ±5 V. The specific on-resistance of $0.2\ \Omega - cm^2$ which are comparable for SBDs on homoepitaxial diamond films. Further improvement of the heteroepitaxial growth and device technology are necessary to suppress the leakage current. The sensor devices using NV centers in diamond were formed in the heteroepitaxial diamond (111) films. The NV centers in heteroepitaxial diamond could be preferentially aligned to the one-atomic direction and leading to improving the sensitivity was confirmed. However, the calculated sensitivity was lower than that of homoepitaxial films. In order to obtain higher sensitivity, it is necessary to improve the crystal quality of heteroepitaxial diamond(111) films. These development of the heteroepitaxial diamond films is expected for large-area and low-cost power and sensor devices platform.

Appendix A

APPENDIX

A.1 Growth of single crystal 3C-SiC on Si

We used the single crystal 3C-SiC intermediate layers grown on Si as substrates for heteroepitaxial growth of diamond. As the 3C-SiC(001) intermediate layers, we used the 3C-SiC with thickness of 4 μm with on-axis and off angle of 2.5° toward [011] direction. The substrates with off angle which promotes step-flow growth because the dangling-bonds of zinc-blende structure faces the [011] direction were used for improving films quality of diamond. The 3C-SiC(111) of thickness of 1 μm with off angle of 2.5° toward $[\overline{1}\overline{1}2]$ direction was used for heteroepitaxial growth of diamond(111). The substrates with off angle and direction of (111) are also formed to promote step-flow growth and formation of aligned NV centers (mentioned in chapter 4). The growth process of 3C-SiC on Si is as follows:

1. The Si substrates is heated by low-pressure horizontal hot-wall CVD reactor at a temperature above 1000°C.

2. Hydrocarbon gas is introduced into CVD chamber. In this step, the 3C-SiC nanoparticles are epitaxially synthesized on Si substrates.

3. After synthesizing the 3C-SiC nanocrystals on Si substrates, it is grown by hydrogen, hydrocarbon, and silane gas mixture.

Figure A.1 shows the SEM and XRD rocking curve of 3C-SiC grown on Si substrates. Although the 3C-SiC(001) shows APD boundary at the surface caused by compound

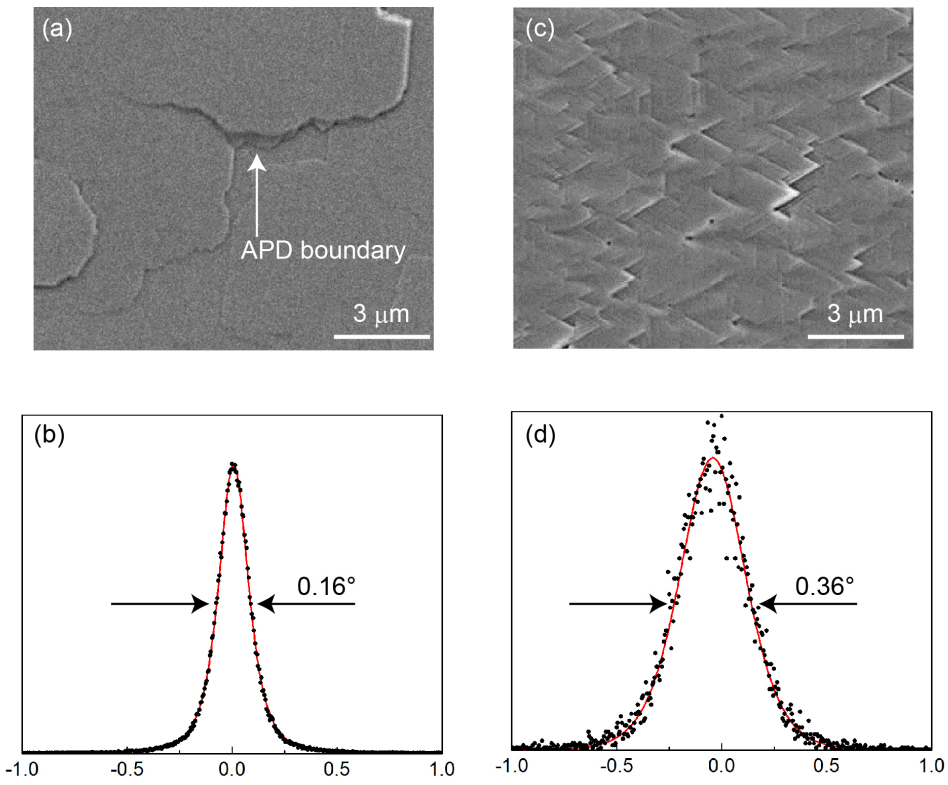

Figure A.1: SEM image and XRD ω-rocking curve of 3C-SiC (a,b) (001) and (c,d) (111).

materials, the diamond is not formed that structure because the diamond is composed only carbon atom. The grain boundaries are existed at the 3C-SiC(111) surface. The FWHM of XRD rocking curve of 0.16° was obtained in 3C-SiC(001) films, which is smaller than that of heteroepitaxial diamond films. Therefore, the heteroepitaxial 3C-SiC films has enough quality for heteroepitaxial diamond films. In fact, the heteroepitaxial diamond(001) films on Ir has only tilt spread of 0.02° even though the tilt spread of Ir layer is around 0.2°. This is caused by evolutionally selection theory during diamond growth. Tilt spread of 0.36° was obtained from 3C-SiC(111) heteroepitaxial films.

A.2 Diamond nucleation and growth conditions

The nucleation and growth conditions of diamond used in this thesis are summarized as follows:

Table A.1: Nucleation Conditions used for section 2.2

	low plasma density	high plasma density
Pressure [kPa]	10	20
CH_4 concentration [%]	1	4
Input microwave power	200	600
Distance [mm]	10	12
Bias Voltage [V]	-50	-100
Temperature [°C]	750	750
Nucleation time [min]	10	5

Table A.2: Nucleation condition used for section 2.3

	(001)	(111)
Pressure [kPa]	20	20
CH_4 concentration [%]	10	20
Input microwave power	800	800
Distance [mm]	12	12
Bias Voltage [V]	-150	-150
Temperature [°C]	1000	1000

Table A.3: Growth conditions used for Fig. 3.2

growth direction	<001> preferential	<111> preferential
Pressure [kPa]	5	5
CH_4 concentration [%]	1	0.5
N_2 concentration [ppm]	120	-
O_2 concentration [%]	-	0.25
Input microwave power	350	350
Temperature [°C]	750	800

Table A.4: Growth condition used for Fig. 3.3

growth direction	<001> preferential	<111> preferential
Pressure [kPa]	20	20
CH_4 concentration [%]	4	4
N_2 concentration [ppm]	120	-
O_2 concentration [%]	-	0.25
Input microwave power	800	800
Temperature [°C]	800	800

Table A.5: Growth conditions used for section 4.1

growth direction	<001> preferential	<111> preferential	Boron doping
Pressure [kPa]	30	30	13
CH_4 concentration [%]	2	2	0.6
N_2 concentration [ppm]	120	-	-
O_2 concentration [%]	-	0.5	0.25
TMB concentration [ppm]	-	-	0.5
Input microwave power	600	600	1200

Table A.6: Growth condition used in section 4.2

	intrinsic	Formation of NV center
Pressure [kPa]	20	20
CH_4 concentration [%]	1	2
N_2 concentration [ppm]	-	300
O_2 concentration [%]	0.25 %	0-0.6 %
Input microwave power	650	650
Temperature [°C]	1100	1100

Bibliography

[1] Hitoshi Umezawa and Shin-ichi Shikata. Leakage Current Analysis of Diamond SBDs Operated at High Temperature. *Japanese Journal of Applied Physics*, 53:04EP04, 2014.

[2] Hitoshi Umezawa, Yukako Kato, and Shinichi Shikata. 1 Ω On-Resistance Diamond Vertical-Schottky Barrier Diode Operated at 250 °C. 6:011302, 1882.

[3] T. Iwasaki, Y. Hoshino, K. Tsuzuki, H. Kato, T. Makino, M. Ogura, D. Takeuchi, T. Matsumoto, H. Okushi, S. Yamasaki, and M. Hatano. Diamond semiconductor JFETs by selectively grown n^+-diamond side gates for next generation power devices. *Technical Digest - International Electron Devices Meeting, IEDM*, (6):6–9, 2012.

[4] Tsubasa Matsumoto, Hiromitsu Kato, Kazuhiro Oyama, Toshiharu Makino, Masahiko Ogura, Daisuke Takeuchi, Takao Inokuma, Norio Tokuda, and Satoshi Yamasaki. Inversion channel diamond metaloxide-semiconductor field-effect transistor with normally off characteristics. *Scientific Reports*, 6(July):1–6, 2016.

[5] Dan Zhao, Chao Hu, Zhangcheng Liu, Hong Xing Wang, Wei Wang, and Jingwen Zhang. Diamond MIP structure Schottky diode with different drift layer thickness. *Diamond and Related Materials*, 73:15–18, 2017.

[6] Aboulaye Traore, Pierre Muret, Alexandre Fiori, David Eon, Aboulaye Traore, Pierre Muret, Alexandre Fiori, David Eon, Etienne Gheeraert, P Muret, A Fiori, D Eon, E Gheeraert, and J Pernot. Zr / oxidized diamond interface for high power Schottky diodes To cite this version :. 052105(2014), 2014.

[7] Takayuki Iwasaki, Fumitaka Ishibashi, Yoshiyuki Miyamoto, Yuki Doi, Satoshi Kobayashi, Takehide Miyazaki, Kosuke Tahara, Kay D. Jahnke, Lachlan J. Rogers, Boris Naydenov, Fedor Jelezko, Satoshi Yamasaki, Shinji Nagamachi, Toshiro Inubushi, Norikazu Mizuochi, and Mutsuko Hatano. Germanium-Vacancy Single Color Centers in Diamond. *Scientific Reports*, 5:1–7, 2015.

[8] Takayuki Iwasaki, Yoshiyuki Miyamoto, Takashi Taniguchi, Petr Siyushev, Mathias H. Metsch, Fedor Jelezko, and Mutsuko Hatano. Tin-Vacancy Quantum Emitters in Diamond. *Physical Review Letters*, 119(25):1–6, 2017.

[9] C D Clark. Silicon defects in diamond. 51(23), 1995.

[10] Chunlang Wang, Christian Kurtsiefer, Harald Weinfurter, and Bernd Burchard. Single photon emission from SiV centres in diamond produced by ion implantation. *Journal of Physics B: Atomic, Molecular and Optical Physics*, 39(1):37–41, 2006.

[11] Victor Acosta and Philip Hemmer. Nitrogen-vacancy centers: Physics and applications. *MRS Bulletin*, 38(2):127–130, 2013.

[12] V. M. Acosta, E. Bauch, M. P. Ledbetter, C. Santori, K. M.C. Fu, P. E. Barclay, R. G. Beausoleil, H. Linget, J. F. Roch, F. Treussart, S. Chemerisov, W. Gawlik, and D. Budker. Diamonds with a high density of nitrogen-vacancy centers for magnetometry applications. *Physical Review B - Condensed Matter and Materials Physics*, 80(11):1–15, 2009.

[13] F. Dolde, H. Fedder, M. W. Doherty, T. Nöbauer, F. Rempp, G. Balasubramanian, T. Wolf, F. Reinhard, L. C L Hollenberg, F. Jelezko, and J. Wrachtrup. Electric-field sensing using single diamond spins. *Nature Physics*, 7(6):459–463, 2011.

[14] Takayuki Iwasaki, Wataru Naruki, Kosuke Tahara, Toshiharu Makino, Hiromitsu Kato, Masahiko Ogura, Daisuke Takeuchi, Satoshi Yamasaki, and Mutsuko Hatano. Direct Nanoscale Sensing of the Internal Electric Field in Operating Semiconductor Devices Using Single Electron Spins. *ACS Nano*, 11(2):1238–1245, 2017.

[15] Taras Plakhotnik, Marcus W. Doherty, Jared H. Cole, Robert Chapman, and Neil B. Manson. All-optical thermometry and thermal properties of the optically detected spin resonances of the NV- center in nanodiamond. *Nano Letters*, 14(9):4989–4996, 2014.

[16] P. Neumann, I. Jakobi, F. Dolde, C. Burk, R. Reuter, G. Waldherr, J. Honert, T. Wolf, A. Brunner, J. H. Shim, D. Suter, H. Sumiya, J. Isoya, and J. Wrachtrup. High-precision nanoscale temperature sensing using single defects in diamond. *Nano Letters*, 13(6):2738–2742, 2013.

[17] G. Kucsko, P. C. Maurer, N. Y. Yao, M. Kubo, H. J. Noh, P. K. Lo, H. Park, and M. D. Lukin. Nanometre-scale thermometry in a living cell. *Nature*, 500(7460):54–58, 2013.

[18] Thomas Wolf, Philipp Neumann, Kazuo Nakamura, Hitoshi Sumiya, Takeshi Ohshima, Junichi Isoya, and Jörg Wrachtrup. Subpicotesla diamond magnetometry. *Physical Review X*, 5(4):1–10, 2015.

[19] H. J. Mamin, M. Kim, M. H. Sherwood, C. T. Rettner, K. Ohno, D. D. Awschalom, and D. Rugar. Nanoscale nuclear magnetic resonance with a nitrogen-vacancy spin sensor. *Science*, 339(6119):557–560, 2013.

[20] Helena S. Knowles, Dhiren M. Kara, and Mete Atatüre. Observing bulk diamond spin coherence in high-purity nanodiamonds. *Nature Materials*, 13(1):21–25, 2014.

[21] Hayato Ozawa, Kosuke Tahara, Hitoshi Ishiwata, Mutsuko Hatano, and Takayuki Iwasaki. Formation of perfectly aligned nitrogen-vacancy-center ensembles in chemical-vapor-deposition-grown diamond (111). *Applied Physics Express*, 10(4), 2017.

[22] Julia Michl, Tokuyuki Teraji, Sebastian Zaiser, Ingmar Jakobi, Gerald Waldherr, Florian Dolde, Philipp Neumann, Marcus W Doherty, Neil B Manson, Junichi Isoya, and Jörg Wrachtrup. Perfect alignment and preferential orientation of nitrogen-vacancy centers during chemical vapor deposition diamond growth on (111) surfaces Perfect alignment and preferential orientation of nitrogen-vacancy centers during chemical vapor deposition diam. 102407(111), 2014.

[23] A. Nawawi, K. J. Tseng, Rusli, G. A.J. Amaratunga, H. Umezawa, and S. Shikata. Characterization of vertical Mo/diamond Schottky barrier diode from non-ideal I-V and C-V measurements based on MIS model. *Diamond and Related Materials*, 35:1–6, 2013.

[24] C. F. Wang, R. Hanson, D. D. Awschalom, E. L. Hu, T. Feygelson, J. Yang, and J. E. Butler. Fabrication and characterization of two-dimensional photonic crystal microcavities in nanocrystalline diamond. *Applied Physics Letters*, 91(20):1–4, 2007.

[25] Carsten Arend, Patrick Appel, Jonas Nils Becker, Marcel Schmidt, Martin Fischer, Stefan Gsell, Matthias Schreck, Christoph Becher, Patrick Maletinsky, and Elke Neu. Site selective growth of heteroepitaxial diamond nanoislands containing single siv centers. 063111(2016), 2016.

[26] J. B. Wang and G. W. Yang. Phase transformation between diamond and graphite in preparation of diamonds by pulsed-laser induced liquid-solid interface reaction. *Journal of Physics Condensed Matter*, 11(37):7089–7094, 1999.

[27] Norio Tokuda, Masahiko Ogura, Tsubasa Matsumoto, Satoshi Yamasaki, and Takao Inokuma. Influence of substrate misorientation on the surface morphology of homoepitaxial diamond (111) films. *Physica Status Solidi (A) Applications and Materials Science*, 213(8):2051–2055, 2016.

[28] O. Brinza, J. Achard, F. Silva, X. Bonnin, P. Barroy, K. De Corte, and A. Gicquel. Dependence of CVD diamond growth rate on substrate orientation as a function of process parameters in the high microwave power density regime. *Physica Status Solidi (A) Applications and Materials Science*, 205(9):2114–2120, 2008.

[29] C. J. Chu, M. P. D'Evelyn, R. H. Hauge, and J. L. Margrave. Mechanism of diamond growth by chemical vapor deposition on diamond (100), (111), and (110) surfaces: Carbon-13 studies. *Journal of Applied Physics*, 70(3):1695–1705, 1991.

[30] Hideaki Yamada, Akiyoshi Chayahara, Hitoshi Umezawa, Nobuteru Tsubouchi, Yoshiaki Mokuno, and Shinichi Shikata. Fabrication and fundamental characterizations of tiled clones of single-crystal diamond with 1-inch size. *Diamond and Related Materials*, 24:29–33, 2012.

[31] Y. Mokuno, A. Chayahara, Y. Soda, H. Yamada, Y. Horino, and N. Fujimori. High rate homoepitaxial growth of diamond by microwave plasma CVD with nitrogen addition. *Diamond and Related Materials*, 15(4-8):455–459, 2006.

[32] Satoshi Koizumi and Tadao Inuzuka. Initial growth process of epitaxial diamond thin films on cbn single Crystals. *Japanese Journal of Applied Physics*, 32(9 R):3920–3927, 1993.

[33] W. Zhu, P. C. Yang, and J. T. Glass. Oriented diamond films grown on nickel substrates. *Applied Physics Letters*, 63(12):1640–1642, 1993.

[34] P.C Yang, W Liu, R Schlesser, C.A Wolden, R.F Davis, J.T Prater, and Z Sitar. Surface melting in the heteroepitaxial nucleation of diamond on Ni. *Journal of Crystal Growth*, 187(1):81–88, 1998.

[35] Suklyun Hong and M Y Chou. Effect of hydrogen on the surface-energy anisotropy of diamond and silicon. *Physical Review B*, 57(11):6262, 1998.

[36] X Jiang, C P Klages, M Rosler, R Zachai, M Hartweg, and H J Fusser. Deposition and Characterization of Diamond Epitaxial Thin-Films on Silicon Substrates. *Applied Physics a-Materials Science & Processing*, 57:483–489, 1993.

[37] T Tachibana, Y Yokota, K Miyata, T Onishi, K Kobashi, M Tarutani, Y Takai, R Shimizu, and Y Shintani. Diamond films heteroepitaxially grown on platinum (111). *Physical Review B*, 56(24):15967–15981, 1997.

[38] M. Fischer, S. Gsell, M. Schreck, R. Brescia, and B. Stritzker. Preparation of 4-inch Ir/YSZ/Si(001) substrates for the large-area deposition of single-crystal diamond. *Diamond and Related Materials*, 17(7-10):1035–1038, 2008.

[39] M. Fischer, R. Brescia, S. Gsell, M. Schreck, T. Brugger, T. Greber, J. Osterwalder, and B. Stritzker. Growth of twin-free heteroepitaxial diamond on Ir/YSZ/Si(111). *Journal of Applied Physics*, 104(12), 2008.

[40] H Kawarada, C Wild, N Herres, R Locher, and P Koidl. Heteroepitaxial growth of highly oriented diamond on cubic silicon carbide. *Journal of Applied Physics*, 81(8):8–11, 1997.

[41] S. Yugo, T. Kanai, T. Kimura, and T. Muto. Generation of diamond nuclei by electric field in plasma chemical vapor deposition. *Science*, 58(10):1036–1038, 1991.

[42] Y. Lifshitz, S. R. Kasi, J. W. Rabalais, and W. Eckstein. Subplantation model for film growth from hyperthermal species. *Physical Review B*, 41(15):10468–10480, 1990.

[43] Y. Lifshitz, Th Köhler, Th Frauenheim, I. Guzmann, A. Hoffman, R. Q. Zhang, X. T. Zhou, S. T. Lee, and Th Ko. The Mechanism of Diamond Nucleation from Energetic Species. *Science*, 297(5586):1531–1533, 2002.

[44] X Jiang, W J Zhang, and C P Klages. Effects of ion bombardment on the nucleation and growth of diamond films. *Physical Review B*, 58(11):7064–7075, 1998.

[45] A. P. Bolshakov, V. G. Ralchenko, V. Y. Yurov, A. F. Popovich, I. A. Antonova, A. A. Khomich, E. E. Ashkinazi, S. G. Ryzhkov, A. V. Vlasov, and A. V. Khomich. High-rate growth of single crystal diamond in microwave plasma in CH_4/H_2 and $CH_4/H_2/Ar$ gas mixtures in presence of intensive soot formation. *Diamond and Related Materials*, 62:49–57, 2016.

[46] C. J. Tang, A. J. Neves, and A. J.S. Fernandes. Influence of nucleation density on film quality, growth rate and morphology of thick CVD diamond films. *Diamond and Related Materials*, 12(9):1488–1494, 2003.

[47] Takeshi Tachibana, Yoshihiro Yokota, Kazushi Hayashi, and Koji Kobashi. Growth of {111}-oriented diamond on Pt/Ir/Pt substrate deposited on sapphire. *Diamond and Related Materials*, 10(9-10):1633–1636, 2001.

[48] Yasuhiko Hayashi, Yoshinori Matsushita, Tetsuo Soga, Masayoshi Umeno, and Takashi Jimbo. The formation of a (111) texture of the diamond film on $Pt/TiO_2/SiO_x/Si$ substrate by microwave plasma chemical vapor deposition. *Diamond and Related Materials*, 11:499–503, 2002.

[49] Atsuhito Sawabe, Hideo Fukuda, Tosiyuki Suzuki, Yuichi Ikuhara, and Tetsuya Suzuki. Interface between CVD diamond and iridium films. *Surface Science*, 467(1-3):845–849, 2000.

[50] B. C. Gallheber, O. Klein, M. Fischer, and M. Schreck. Propagation of threading dislocations in heteroepitaxial diamond films with (111) orientation and their role in the formation of intrinsic stress. *Journal of Applied Physics*, 121(22), 2017.

[51] S. T. Lee, H. Y. Peng, X. T. Zhou, N. Wang, C. S. Lee, I. Bello, and Y. Lifshitz. A nucleation site and mechanism leading to epitaxial growth of diamond films. *Science*, 287(5450):104–106, 2000.

[52] B.R. Stoner and J.T. Glass. Textured diamond growth on (100) β-SiC via microwave plasma chemical vapor deposition. *Applied Physics Letters*, 60(6):698–700, 1992.

[53] J. C. Arnault, S. Saada, S. Delclos, L. Intiso, N. Tranchant, R. Polini, and Ph Bergonzo. In situ study of the initial stages of diamond deposition on 3C-SiC (100) surfaces: Towards the mechanisms of diamond nucleation. *Diamond and Related Materials*, 16(4-7 SPEC. ISS.):690–694, 2007.

[54] B. R. Stoner, G. H. Ma, S. D. Wolter, W. Zhu, Y. C. Wang, R. F. Davis, and J. T. Glass. Epitaxial nucleation of diamond on β-SiC via bias-enhanced microwave plasma chemical vapor deposition. *Diamond and Related Materials*, 2(2-4):142–146, 1993.

[55] H. Kawarada, T. Suesada, and H. Nagasawa. Heteroepitaxial growth of smooth and continuous diamond thin films on silicon substrates via high quality silicon carbide buffer layers. *Applied Physics Letters*, 583(1995):583, 1995.

[56] H. Kawarada, C. Wild, N. Herres, P. Koidl, Y. Mizuochi, A. Hokazono, and H. Nagasawa. Surface morphology and surface p-channel field effect transistor on the heteroepitaxial diamond deposited on inclined β-SiC(001) surfaces. *Applied Physics Letters*, 72(15):1878–1880, 1998.

[57] Mohd Syamsul, Nobutaka Oi, Satoshi Okubo, Taisuke Kageura, and Hiroshi Kawarada. Heteroepitaxial diamond field-effect transistor for high voltage applications. *IEEE Electron Device Letters*, 3106(c):1–1, 2017.

[58] T. Vandevelde, M. Nesladek, C. Quaeyhaegens, and L. Stals. Optical emission spectroscopy of the plasma during CVD diamond growth with nitrogen addition. *Thin Solid Films*, 290-291:143–147, 1996.

[59] K. J. Clay, S. P. Speakman, G. A. J. Amaratunga, and S. R. P. Silva. Characterization of a − C : H : N deposition from CH4/N2 rf plasmas using optical emission spectroscopy. *Journal of Applied Physics*, 79(9):7227–7233, 1996.

[60] B. R. Stoner, G. H.M. Ma, S. D. Wolter, and J. T. Glass. Characterization of bias-enhanced nucleation of diamond on silicon by invacuo surface analysis and transmission electron microscopy. *Physical Review B*, 45(19):11067–11084, 1992.

[61] Vu Ngoc Tuoc. First Principle Study on the Domain Matching Epitaxy Growth of Semiconductor Hetero-Interface. *Materials Transactions*, 49(11):2491–2496, 2008.

[62] W. Zhu, X. H. Wang, B. R. Stoner, G. H.M. Ma, H. S. Kong, M. W.H. Braun, and J. T. Glass. Diamond and β-SiC heteroepitaxial interfaces: A theoretical and experimental study. *Physical Review B*, 47(11):6529–6542, 1993.

[63] Falko Langenhorst and Vladimir L. Solozhenko. ATEM-EELS study of new diamond-like phases in the B-C-N system. *Phys. Chem. Chem. Phys.*, 4(20):5183–5188, 2002.

[64] T. S. Perova, J. Wasyluk, S. A. Kukushkin, A. V. Osipov, N. A. Feoktistov, and S. A. Grudinkin. Micro-raman mapping of 3C-SiC thin films grown by solid-gas phase epitaxy on Si (111). *Nanoscale Research Letters*, 5(9):1507–1511, 2010.

[65] Debabrata Pradhan and I. Nan Lin. Grain-size-dependent diamond?nondiamond composite films: Characterization and field-emission properties. *ACS Applied Materials and Interfaces*, 1(7):1444–1450, 2009.

[66] J A Mucha, D L Flamm, and D E Ibbotson. On the role of oxygen and hydrogen in diamond forming discharge. 65(1989):3348–3452, 1989.

[67] Christopher D. Zuiker, Dieter M. Gruen, and Alan R. Krauss. In situ laser reflectance interferometry measurement of diamond film growth. *Journal of Applied Physics*, 79(7):3541–3547, 1996.

[68] Colin Delfaure, Nicolas Tranchant, Jean Paul Mazellier, Pascal Ponard, and Samuel Saada. Monitoring texture formation during diamond growth by specular and diffuse reflectance interferometry. *Diamond and Related Materials*, 69:214–220, 2016.

[69] Kuoguang Perng, Kuo Shung Liu, and I. Nan Lin. Study on bias-enhanced nucleation of diamonds by simulating the time dependence of bias current. *Journal of Applied Physics*, 91(6):3934–3936, 2002.

[70] S. Barrat, S. Saada, I. Dieguez, and E. Bauer-Grosse. Diamond deposition by chemical vapor deposition process: Study of the bias enhanced nucleation step. *Journal of Applied Physics*, 84(4):1870–1880, 1998.

[71] M. Schreck, K. H. Thürer, and B. Stritzker. Limitations of the process window for the bias enhanced nucleation of heteroepitaxial diamond films on silicon in the time domain. *Journal of Applied Physics*, 81(7):3092–3095, 1997.

[72] Nadine Marechal and Satoshi Yamashita. Oriented Nucleation of Diamond Particles on (001) β-SiC Surface at Low Pressure, 1995.

[73] S. Saada, S. Pochet, L. Rocha, J. C. Arnault, and P. Bergonzo. Real time investigation of diamond nucleation by laser scattering. *Diamond and Related Materials*, 18(5-8):707–712, 2009.

[74] L. Constant and F. Le Normand. HF CVD diamond nucleation and growth on polycrystalline copper: A kinetic study. *Thin Solid Films*, 516(5):691–695, 2008.

[75] I. Sinha and R. K. Mandal. Avrami exponent under transient and heterogeneous nucleation transformation conditions. *Journal of Non-Crystalline Solids*, 357(3):919–925, 2011.

[76] Qian Gao, Zengyun Jian, Junfeng Xu, Man Zhu, Fange Chang, and Amin Han. Crystallization kinetics of the $Cu_{50}Zr_{50}$ metallic glass under isothermal conditions. *Journal of Solid State Chemistry*, 244(June):116–119, 2016.

[77] Norikazu Taniyama, Minoru Kudo, Osamu Matsumoto, and Hiroshi Kawarada. Diamond deposition on a large-area substrate by plasma-assisted chemical vapor deposition using an antenna-type coaxial microwave plasma generator. *Japanese Journal of Applied Physics, Part 2: Letters*, 40(7 A), 2001.

[78] Chih-shiue Yan, Yogesh K Vohra, Ho-kwang Mao, and Russell J Hemley. Very high growth rate chemical vapor deposition of single-crystal diamond. 99(20):12523–12525, 2002.

[79] C. Wild, P. Koidl, W. Müller-Sebert, H. Walcher, R. Kohl, N. Herres, R. Locher, R. Samlenski, and R. Brenn. Chemical vapour deposition and characterization of smooth {100}-faceted diamond films. *Diamond and Related Materials*, 2(2-4):158–168, 1993.

[80] Qi Hua Fan, J. Grácio, and E. Pereira. Residual stresses in chemical vapour deposited diamond films. *Diamond and Related Materials*, 9(9):1739–1743, 2000.

[81] J. Michler, Y. Von Kaenel, J. Stiegler, and E. Blank. Complementary application of electron microscopy and micro-Raman spectroscopy for microstructure, stress, and bonding defect investigation of heteroepitaxial chemical vapor deposited diamond films. *Journal of Applied Physics*, 83(1):187–197, 1998.

[82] Mei Liu, Haihui Ruan, Liangchi Zhang, and Alireza Moridi. Effects of misfit dislocation and film-thickness on the residual stresses in epitaxial thin film systems: Experimental analysis and modeling. *Journal of Materials Research*, 27(21):2737–2745, 2012.

[83] Nobuteru Tsubouchi, Y. Mokuno, and S. Shikata. Characterizations of etch pits formed on single crystal diamond surface using oxygen/hydrogen plasma surface treatment. *Diamond and Related Materials*, 63:43–46, 2016.

[84] C. Stehl, M. Fischer, S. Gsell, E. Berdermann, M. S. Rahman, M. Traeger, O. Klein, and M. Schreck. Efficiency of dislocation density reduction during heteroepitaxial growth of diamond for detector applications. *Applied Physics Letters*, 103(15):3–7, 2013.

[85] Masami Tachikawa and Masafumi Yamaguchi. Film thickness dependence of dislocation density reduction in GaAs-on-Si substrates. *Applied Physics Letters*, 56(5):484–486, 1990.

[86] J. S. Speck, M. A. Brewer, G. Beltz, A. E. Romanov, and W. Pompe. Scaling laws for the reduction of threading dislocation densities in homogeneous buffer layers. *Journal of Applied Physics*, 80(7):3808–3816, 1996.

[87] C. Wild, R. Kohl, N. Herres, W. Müller-Sebert, and P. Koidl. Oriented CVD diamond films: twin formation, structure and morphology. *Diamond and Related Materials*, 3(4-6):373–381, 1994.

[88] Hitoshi Umezawa, Natsuo Tatsumi, Yukako Kato, and Shin Ichi Shikata. Leakage current analysis of diamond Schottky barrier diodes by defect imaging. *Diamond and Related Materials*, 40:56–59, 2013.

[89] Alexandre Tallaire, Ovidiu Brinza, Vianney Mille, Ludovic William, and Jocelyn Achard. Reduction of Dislocations in Single Crystal Diamond by Lateral Growth over a Macroscopic Hole. *Advanced Materials*, 29(16):1–5, 2017.

[90] Janine Riedrich-Möller, Laura Kipfstuhl, Christian Hepp, Elke Neu, Christoph Pauly, Frank Mücklich, Armin Baur, Michael Wandt, Sandra Wolff, Martin Fischer, Stefan Gsell, Matthias Schreck, and Christoph Becher. One-and two-dimensional

photonic crystal microcavities in single crystal diamond. *Nature Nanotechnology*, 7(1):69–74, 2012.

[91] Takehide Miyazaki, Yoshiyuki Miyamoto, Toshiharu Makino, Hiromitsu Kato, Satoshi Yamasaki, Takahiro Fukui, Yuki Doi, Norio Tokuda, Mutsuko Hatano, and Norikazu Mizuochi. Atomistic mechanism of perfect alignment of nitrogen-vacancy centers in diamond. *Applied Physics Letters*, 105(26), 2014.

[92] Isao Sakaguchi, Mikka Nishitani-gamo, Kian Ping Loh, Hajime Haneda, Shunichi Hishita, Toshihiro Ando, Isao Sakaguchi, Mikka Nishitani-gamo, and Kian Ping Loh. Silicon incorporation into chemical vapor deposition diamond : A role of oxygen Silicon incorporation into chemical vapor deposition diamond : A role of oxygen. *Applied Physics Letters*, 71(1997):629–631, 1997.

[93] P. K. Bachmann, H. J. Hagemann, H. Lade, D. Leers, D. U. Wiechert, H. Wilson, D. Fournier, and K. Plamann. Thermal properties of C/H-, C/H/O-, C/H/N- and C/H/X-grown polycrystalline CVD diamond. *Diamond and Related Materials*, 4(5-6):820–826, 1995.

[94] Peter E Norris. Kinetic study of ground state silicon atoms, si[$3p^2(^3P_J)$], by atomic absorption spectroscopy. pages 93–105, 1977.

[95] Rajesh Dorai and Mark J Kushner. Repetitively pulsed plasma remediation of NO_x in soot laden exhaust using dielectric barrier discharges. *Journal of Physics D: Applied Physics*, 35(22):2954–2968, 2002.

[96] Kosuke Tahara, Hayato Ozawa, Takayuki Iwasaki, Norikazu Mizuochi, and Mutsuko Hatano. Quantifying selective alignment of ensemble nitrogen-vacancy centers in (111) diamond. *Applied Physics Letters*, 107(19), 2015.

[97] D. Le Sage, K. Arai, D. R. Glenn, S. J. Devience, L. M. Pham, L. Rahn-Lee, M. D. Lukin, A. Yacoby, A. Komeili, and R. L. Walsworth. Optical magnetic imaging of living cells. *Nature*, 496(7446):486–489, 2013.

[98] Hidetaka Sawada, Hideki Ichinose, and Masanori Kohyama. Atomic structure of the Σ3 and Σ9 grain boundaries in CVD diamond film. *Scripta Materialia*, 51(7):689–692, 2004.

[99] Peter Steneteg, Valeriu Chirita, Natalia Dubrovinskaia, Leonid Dubrovinsky, and Igor A. Abrikosov. Missing-atom structure of diamond Σ5 (001) twist grain boundary. *Physical Review B - Condensed Matter and Materials Physics*, 84(14):3–6, 2011.

[100] X Jiang. The coalescence of diamond grains heteroepitaxially grown on (001) silicon. *Applied physics letters*, 69(December):3902–3904, 1996.

[101] Viktor Ivády, Tamás Simon, Jeronimo R. Maze, I. A. Abrikosov, and Adam Gali. Pressure and temperature dependence of the zero-field splitting in the ground state of NV centers in diamond: A first-principles study. *Physical Review B - Condensed Matter and Materials Physics*, 90(23):1–8, 2014.

[102] Marcus W. Doherty, Viktor V. Struzhkin, David A. Simpson, Liam P. McGuinness, Yufei Meng, Alastair Stacey, Timothy J. Karle, Russell J. Hemley, Neil B. Manson, Lloyd C L Hollenberg, and Steven Prawer. Electronic properties and metrology applications of the diamond NV - Center under pressure, 2014.

[103] Matthew E. Trusheim and Dirk Englund. Wide-field strain imaging with preferentially aligned nitrogen-vacancy centers in polycrystalline diamond. *New Journal of Physics*, 18(12), 2016.

[104] Zhi Hui Wang and Susumu Takahashi. Spin decoherence and electron spin bath noise of a nitrogen-vacancy center in diamond. *Physical Review B - Condensed Matter and Materials Physics*, 87(11):1–6, 2013.

[105] Taro Nishiguchi, Mitsuhiro Nakamura, Koji Nishio, Toshiyuki Isshiki, and Shigehiro Nishino. Heteroepitaxial growth of (111) 3C-SiC on well-lattice-matched (110) Si substrates by chemical vapor deposition. *Applied Physics Letters*, 84(16):3082–3084, 2004.

[106] R. Anzalone, A. Severino, G. D'Arrigo, C. Bongiorno, G. Abbondanza, G. Foti, S. Saddow, and F. La Via. Heteroepitaxy of 3C -SiC on different on-axis oriented silicon substrates. *Journal of Applied Physics*, 105(8):1–8, 2009.